POLITECNICO DI TORINO

Master's Degree in Electronic Engineering

Politecnico
di Torino

Master's Degree Thesis

Advanced Computational Strategies in Electromagnetic BEM Preconditioning

Supervisors

Prof. Francesco P. ANDRIULLI

Prof. Adrien MERLINI

Candidate

Masciocchi MATTEO

ACADEMIC YEAR 2023-2024

Summary

Abstract

This thesis presents some advancements in computational electromagnetics, focusing on integral equation methods for the solution of electromagnetic scattering problems. It explores numerical techniques and matrix operations that enhance the computational efficiency necessary for practical applications: the analysis starts from the derivation of the BEM equations from the Maxwell's systems, continues exploring the most popular basis functions and discretization schemes, tackles the complexity issues that arise introducing fast solvers and preconditioning, investigates harmonic transforms and their behavior on non-regular domains, focuses on the recent preconditioning techniques relying on Laplacian filters, and finally introduces a novel approach to operator filtering. This work presents arguments for both 2D and 3D formulations.

Integral Operators and BEM

Integral operators play a crucial role in formulating the boundary element method (BEM) from Maxwell's equations. The thesis starts by deriving integral equations from Maxwell's systems, highlighting how these equations can be transformed into boundary integral equations suitable for numerical treatment. The BEM is particularly effective for solving scattering problems as it reduces the dimensionality of the problem by one, focusing computations on the boundary of the domain only. Key integral equations, such as the Electric Field Integral Equation (EFIE) and Magnetic Field Integral Equation (MFIE), are discussed in details. The use of boundary conditions and the application of Love's equivalence principle to transform scattering problems into more manageable forms are also covered. The focus is then placed on the discretization of such operators. Basis functions such as Rao-Wilton-Glisson, Loop and Star are introduced, and numerical integration and the implication of dealing with discretized linear systems are addressed.

Well-Known Computational Issues, Solutions, and Fast Schemes

One of the main computational challenges in solving integral equations is the high complexity and large memory requirements of the resulting formulations. Intuitively, this is due to the fact that integral operators leads to dense matrices since each element of the solution depends on all the elements of the source. Solution of dense, full rank linear systems is generally $\mathcal{O}(N^3)$, being N the number of unknowns. The thesis addresses these issues by exploring various numerical techniques and fast algorithms. Techniques such as the Method of Moments (MoM) and preconditioning are employed for discretizing integral equations, leading to a system of linear equations with favourable properties for fast solution. The thesis delves into the use of the Fast Multipole Method (FMM) and Adaptive Cross Approximation (ACA) to accelerate matrix-vector multiplications, significantly reducing computational time and memory usage. Finally, preconditioning techniques, such as the use of the Helmholtz decomposition and quasi-Helmholtz projection, are discussed to improve the convergence rates of iterative solvers.

Geometry Regularity and Flexible Approaches

The accuracy and efficiency of numerical methods in electromagnetics often depend on the regularity of the geometry being analyzed. This work includes a detailed analysis of how the operator of interest straightforwardly simplifies when computed on harmonic geometries, such as circle and sphere, and with uniform discretization. However, such domains are of little practical interest, thus the challenge is to adapt the schemes that lead to these simplifications in such a way that they are applicable also to non-uniform domains. Non-uniform discretization schemes, from the well-known Non-Uniform Discrete Fourier Transform (NUDFT) to the recently introduced Non-Uniform Vector Spherical Harmonic Transform, are explored for their ability to handle complex geometries with varying levels of detail, with favourable complexities. These transforms facilitate the efficient computation of electromagnetic fields on irregular surfaces, enhancing the applicability of the numerical methods. The research also examines the relationship between spherical harmonic transforms and the 2D Fast Fourier Transform (FFT), investigating the contexts in which the former can be replaced by the latter, leading to further computational efficiency.

Operator Filtering Strategies

The thesis review and introduces advanced operator filtering strategies to enhance numerical stability and efficiency. Laplacian multiplicative filters, introduced by Merlini et al. in 2022, have been proved to be an efficient filtering strategy, paving the way to new families of direct and inverse solvers. They are essentially

multiplicative preconditioners for the integral operators that behave as spectral low pass filters, allowing for efficient storage and manipulation of the target matrices. The analogies among the operators and Laplacian spectrum are the foundations for their effectiveness. The newly introduced Modified Green's functions formulations for the 2D case embody another approach to filtering, which does not rely on multiplicative preconditioners but rather on modifying the continuous operator formulations, in such a way that their discretized counterparts exhibit a truncated spectrum. Numerical results demonstrate the success of these filters in modifying the operator spectral properties. The implementation details and practical applications of these filtering strategies are thoroughly discussed.

Conclusions

This thesis work is a panoramic onto the actual research panorama in the BEM computational electromagnetics field, going from its theoretical foundations to many open research problems, touching four out of the ten most impactful algorithms of the 20^{th} century, and including also some advancements in operator filtering. The text is enriched with numerical results to show the effectiveness in practical scenarios of the proposed formulations, as well as abundant citations to external sources where the interested reader can find further details. Mathematical notation and equations are extensively employed, being by far the more appropriate language for the topic.

Acknowledgements

This thesis work and graduation wouldn't have been possible without the precious support of many peoples.

The first greeting goes to my family, dad and mom, who supported me in my growth and studies since my childhood. I will always estimate the endless time they spent with me, playing and satisfying my curiosity about the world: there is where my interest for science rose. And on top of that, thank you for the care you had for me everyday, and still.

Moving from the childhood straight to the end of the path, I want to thank Professor Andriulli, who's passion for science and academic rigor taught me a lot. He picked me up in the last year of my bachelor, and always believed in my capabilities far beyond what I did by myself. His approach to research and teaching have been inspiring for me: a mix of love for science, willingness to invest on the young, talented students, the healthy tension for him and his students to excel in the field, and out of the ordinary passions. The taste of the world-class research environment that he gifted me is invaluable.

And now it's time for the travel companions. A big thank you goes to Alessandro, Mattia, Tommaso and Matilde, who have been much more than colleagues. I will always remember the mountain hikes and travels, the long hours spent for the group works, the dinners and ticket to ride matches, the fun we had in tackling each exam like a team-sport challenge.

Thank you Valentina for all the reports and deadlines that you remembered also for me.

But there have been much, much more than university in those years. Thank you Bea for your love, and for the wonderful relationship we're building together. I don't have words to describe my gratitude to you, and I always thank God for that immense grace. I hope this will be just the beginning of a long life together.

Thank you Davide, Alessandro and Giorgio, for all we've shared in these years. Your friendship have been a safe harbor where I always felt welcomed and understood.

Thank you Ire for our friendship, where the "how are you?" Sentence usually

needs a couple of hours to be answered.

Thank you to all the Sanbe, scout and oratory community, where my faith growth and where I'm now trying to give back even a little fraction of what I got.

Thank you to all the people who I encountered in and at Fuoridivela: the association experience let me grow under many aspects, and left me unforgettable remembering.

Thank you Ilaria for our friendship, that in some weird way made us live together many moments in very different contexts.

Thank you Andrea and Samuele, first year companions, for the reciprocal support in learning how to tackle the big Politecnico beast.

And going back even further, thanks to my high school professors Murabito, De Sanso and Oragano. I still remember the wise words and all the attention you put on me, and I will always be grateful.

These university years have been an amazing trip. This list is widely incomplete and superficial, and I apologize for all the people not explicitly mentioned here.

I hope that's just the beginning, and that I will have you onboard for a long time still. All the best wishes to every one of you.

Thank *you*.

Ringraziamenti

Questa tesi e questa laurea non sarebbero state possibili senza il prezioso supporto di molte persone.

Il primo ringraziamento va alla mia famiglia, papà e mamma, che mi hanno sempre accompagnato nella mia crescita e nei miei studi fin da quando ero bambino. Vi stimerò sempre per l'infinito tempo speso con me, giocando e soddisfano la mia curiosità per il mondo: è sicuramente lì che nacque il mio interesse per la scienza. E soprattutto, grazie per la cura di me che avete avuto negli anni, e che ancora oggi avete per me.

Saltando direttamente alla fine, voglio ringraziare il professor Andriulli, la cui passione per la scienza e il cui rigore accademico mi hanno insegnato molto. Mi ha raggiunto l'ultimo anno di triennale, e ha sempre creduto nelle mie capacità molto più di quanto ci credessi io stesso. Il suo approccio alla ricerca e all'insegnamento sono stati di grande ispirazione: un mix di amore per la scienza, volontà di investire nei giovani talentuosi, la sana tensione per lui e per i suoi studenti a eccellere nel campo della ricerca, e passioni fuori dal comune. L'assaggio del mondo della ricerca che mi ha donato è di inestimabile valore.

E ora è il momento dei compagni di viaggio. Un grande grazie a Alessandro, Mattia, Tommaso e Matilde, che sono stati molto più che colleghi. Ricorderò sempre le gite in montagna e i viaggi, le lunghe ore passate insieme per i lavori di gruppo, le cene e le partite a Ticket to Ride, il divertimento che abbiamo condiviso nell'affrontare ogni esame come una partita di gruppo.

Grazie Valentina per tutte le consegne e i report che ti sei ricordata al posto mio.

Ma c'è stato molto, molto più dell'università in questi anni. Grazie bea per il tuo amore, e per la meravigliosa relazione che stiamo costruendo. Non ho parole per descrivere la mia gratitudine per te, e ringrazio Dio per tutta questa grazia. Spero questo sia stato solo l'inizio di una lunga vita insieme.

Grazie Davide, Alessandro e Giorgio per tutto quel che abbiamo condiviso in questi anni. La vostra amicizia è stata un porto sicuro in cui mi sono sempre sentito accolto e compreso.

Grazie Ire per la nostra amicizia, in cui la domanda “come stai?” Solitamente richiede un paio d’ore per rispondere.

Grazie a tutta la comunità di Sanbe, scout e oratorio, in cui la mia fede è cresciuta e dove sto ora provando a restituire anche solo un piccolo pezzo di ciò che ho ricevuto.

Grazie a tutte le persone che ho incontrato a Fuoridivela: l’esperienza associativa mi ha fatto crescere sotto molti aspetti, e mi ha lasciato ricordi indelebili.

Grazie Ilaria per la nostra amicizia, che in qualche strano modo ci ha fatto vivere insieme molti momenti in contesti diversissimi tra loro.

Grazie Andrea e Samuele, compagni del primo anno, per il supporto reciproco nell’imparare come domare la grande bestia chiamata Politecnico.

E tornando ancora più indietro, grazie ai miei professori delle superiori Murabito, De Sanso e Oragano. Ricordo ancora le sagge parole e tutte le attenzioni che mi avete riservato, e ve ne sarò sempre grato.

Gli anni di università sono stati un magnifico viaggio. Questa lista è ampiamente incompleta e superficiale, e mi scuso per tutte le persone non esplicitamente menzionate qui.

Spero sia solo l’inizio, e spero di avervi a bordo ancora per lungo tempo. I migliori auguri per ognuno di voi.

Grazie a *te*.

Table of Contents

List of Figures

Acronyms

ACA
Adaptive Cross Approximation

BC
Buffa-Christiansen

BEM
Boundary Element Method

DFT
discrete Fourier transform

EFIE/O
Electric Field Integral Equation/Operator

FaVeST
Fast Vector Spherical harmonic Transform

FFT
fast Fourier transform

FMM
fast multiple method

LHS
left hand side

MFIE/O
Magnetic Field Integral Equation/Operator

MoM

Method of Moments

PEC

Perfect Electric Conductor

PMC

Perfect Magnetic Conductor

RHS

right hand side

RWG

Rao-Wilton-Glisson

SHT

Spherical Harmonic Transform

Chapter 1

Introduction to Computational Electromagnetics

In this chapter, a continuous line will be drawn from the Maxwell equations to the discretized electric and magnetic integral equations, passing through wave theory, the Method of Moments and the Boundary element Method.

2D notations

In this thesis, we will always present together with the 3D formulations also the 2D equivalents. More in details, with 2D setting, we refer to geometries which are invariant over one dimension (by convention, the $\hat{z}$ axis). Thus, in this context, the problem is evaluated only on the xy plane, where the geometry manifold collapse into a curve. Physical quantities on this geometries are represented as $\boldsymbol{X} = X_t\hat{\boldsymbol{t}} + X_z\hat{\boldsymbol{z}} + X_n\hat{\boldsymbol{n}}$, where t denotes the quantities on the xy plane, tangential to the surface; n denotes the quantities on the xy plane, perpendicular to the surface and z denotes the quantities on the z axis (i.e., tangential to the surface). Fig. 1.1 exemplifies the notation for a simple geometry.

1.1 The Maxwell's system

Maxwell's theory has been a major milestone in physics, describing in a powerful and incredibly predictive way the relationships among the Electric and Magnetic fields, an interplay that underpins much of modern electromagnetic theory and applications. This understanding has been suggested by the observation of a number of physical phenomena where an interaction between electric $\mathcal{E}$ and magnetic $\mathcal{B}$

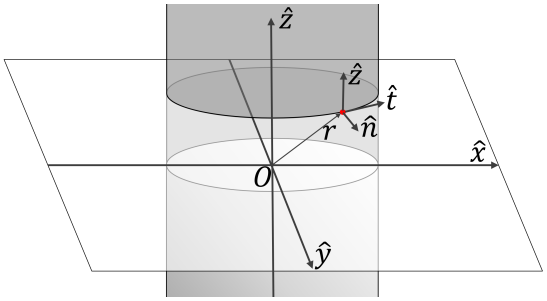

Figure 1.1: Notation used for the 2D setting. The sample shape is a circle, i.e., an infinite cilinder due to invariancy along the z axis.

fields was undeniable. Then, experiments carried out by different scientists of the time confirmed the evidence, and finally James Clerk Maxwell, synthesizing earlier works by Faraday, Ampère, and others, formulated a set of equations that not only described this interaction but also unified the study of electricity, magnetism, and even optics into a coherent theory of electromagnetism.

1.1.1 Maxwell's and Continuity Equations in integral form

The whole electromagnetic theory rely on a set of four equations, called the Maxwell's system. Given an open surface C bounded by a closed contour γ, and a closed surface S enclosing the volume V, these equations read

$$\oiint_S \boldsymbol{\mathcal{D}}(\boldsymbol{r},t)\cdot d\boldsymbol{S} = \iiint_V \rho_e(\boldsymbol{r},t)\, d\boldsymbol{V} \tag{1.1}$$

$$\oint_\gamma \boldsymbol{\mathcal{E}}(\boldsymbol{r},t)\cdot d\boldsymbol{l} = -\frac{\partial}{\partial t}\iint_C \boldsymbol{\mathcal{B}}(\boldsymbol{r},t)\cdot d\boldsymbol{C} - \iint_C \boldsymbol{\mathcal{M}}(\boldsymbol{r},t)\cdot d\boldsymbol{C} \tag{1.2}$$

$$\oiint_S \boldsymbol{\mathcal{B}}(\boldsymbol{r},t)\cdot d\boldsymbol{S} = \iiint_V \rho_m(\boldsymbol{r},t)\, d\boldsymbol{V} \tag{1.3}$$

$$\oint_\gamma \boldsymbol{\mathcal{H}}(\boldsymbol{r},t)\cdot d\boldsymbol{l} = \frac{\partial}{\partial t}\iint_C \boldsymbol{\mathcal{D}}(\boldsymbol{r},t)\cdot d\boldsymbol{C} + \iint_C \boldsymbol{\mathcal{J}}(\boldsymbol{r},t)\cdot d\boldsymbol{C}. \tag{1.4}$$

$$\tag{1.5}$$

Definitions and units of the quantities involved are the following:

$\boldsymbol{\mathcal{E}}$ is the electric field, V/m;

$\boldsymbol{\mathcal{H}}$ is the magnetic field, A/m;

$\boldsymbol{\mathcal{D}}$ is the electric flux density, A·s/m^2;

$\boldsymbol{\mathcal{B}}$ is the magnetic flux density, V·s/m^2;

$\boldsymbol{\mathcal{J}}$ is the electric current density, $\mathrm{A/m^2}$;

$\boldsymbol{\mathcal{M}}$ is the magnetic current density, $\mathrm{V/m^2}$ (unobserved in nature);

ρ_m is the magnetic charge density, in $\mathrm{V{\cdot}s/m^3}$ (unobserved in nature);

ρ_e is electric charge density, in $\mathrm{A{\cdot}s/m^3}$.

These equations are valid in any extended region of space (no continuity conditions are required), and they are known as the Maxwell's equations in integral form. Eq. 1.1 establishes the relationship among electric charge and electric field, and it is independent on frequency. Eq. 1.2, also known as Faraday's law, determines that also a varying magnetic field can be a source of an electric field (note that $\boldsymbol{\mathcal{M}}$ is introduced for symmetry with the electric field, but is zero in all known cases). Eq. 1.3 affirm that the magnetic field is purely solenoidal (note that ρ_m is introduced only for symmetry with the electric field, but is zero in all known cases). Eq. 1.4, also known as Ampère-Maxwell law, to conclude, defines the sources of the magnetic field: variations in time of the Electric field flux and electric currents.

Then, it is necessary to mention the equations relating fields and flux densities, called constitutive equations,

$$\boldsymbol{\mathcal{B}}(\boldsymbol{r},t) = \boldsymbol{\mu}\,\boldsymbol{\mathcal{H}}(\boldsymbol{r},t) \tag{1.6}$$

$$\boldsymbol{\mathcal{D}}(\boldsymbol{r},t) = \boldsymbol{\epsilon}\,\boldsymbol{\mathcal{E}}(\boldsymbol{r},t), \tag{1.7}$$

where the quantities denoted as $\boldsymbol{\mu}$ and $\boldsymbol{\epsilon}$ are respectively the permeability and the permittivity of the medium in which field propagation occurs. These are in general tensor quantities and show complicated dependence on position, time, frequency, and on the field itself. A commonly used simplification is to consider μ and ϵ as constant scalars: this is the assumption of a medium which is isotropic (same properties in all directions), linear (w.r.t. response to electromagnetic fields), and homogeneous (uniform properties throughout the medium). Since vacuum represents the most common medium with such properties, its permeability and permittivity are known as μ_0 and ϵ_0, whose values are

$$\mu_0 = 4\pi 10^{-7}\,\mathrm{H/m}$$

$$\epsilon_0 = \frac{1}{\mu_0\, c_0^2} = 8.85 \times 10^{-12}\,\mathrm{F/m}.$$

Speed of light in vacuum, denoted as c_0, is one of the seven fundamental constants established in the International System of Units, of value 299,792,458 m/s. From this, for any medium with such properties, permeability and permittivity are expressed as $\mu = \mu_0\,\mu_r$, $\epsilon = \epsilon_0\,\epsilon_r$, where μ_r and ϵ_r are adimensional quantities.

Finally, the assumption of conservation of the electric charge is based on experimental evidences, and translates in the continuity equation

$$\oiint_S \boldsymbol{\mathcal{J}}(\boldsymbol{r},t)\cdot d\boldsymbol{S} = -\frac{\partial}{\partial t}\iiint_V \rho_e(\boldsymbol{r},t)\,dV. \tag{1.8}$$

For the sake of symmetry, the continuity equation is also defined for the magnetic field as

$$\oiint_S \boldsymbol{\mathcal{M}}(\boldsymbol{r},t)\cdot d\boldsymbol{S} = -\frac{\partial}{\partial t}\iiint_V \rho_m(\boldsymbol{r},t)\,dV \tag{1.9}$$

however, notice that all the involved quantities has not been observed in nature so far.

1.1.2 Maxwell's and Continuity Equations in differential form

Stokes' theorem, which reads $\oint_C \boldsymbol{A}\cdot d\boldsymbol{l} = \iint_S(\nabla\times\boldsymbol{A})\cdot d\boldsymbol{S}$ with $\boldsymbol{A}$ being a generic vector field, is exploited to move to the differential form:

$$\nabla\times\boldsymbol{\mathcal{E}}(\boldsymbol{r},t) = -\frac{\partial}{\partial t}\boldsymbol{\mathcal{B}}(\boldsymbol{r},t) - \boldsymbol{\mathcal{M}}(\boldsymbol{r},t) \tag{1.10}$$

$$\nabla\times\boldsymbol{\mathcal{H}}(\boldsymbol{r},t) = \frac{\partial}{\partial t}\boldsymbol{\mathcal{D}}(\boldsymbol{r},t) + \boldsymbol{\mathcal{J}}(\boldsymbol{r},t). \tag{1.11}$$

$$\nabla\cdot\boldsymbol{\mathcal{B}}(\boldsymbol{r},t) = \rho_m(\boldsymbol{r},t) \tag{1.12}$$

$$\nabla\cdot\boldsymbol{\mathcal{D}}(\boldsymbol{r},t) = \rho_e(\boldsymbol{r},t). \tag{1.13}$$

To simplify the flux integrals which are involved, some conditions need to be verified for these expressions to be valid: the vector fields should be «single-valued, bounded, continuous functions of position and time and exhibit continuous derivatives» [1]. Such conditions hold true if the surface C and its contour γ, as well as the volume V, lie in a isotropic, linear and homogeneous medium.

In these equations, the electric current density $\boldsymbol{\mathcal{J}}$ is the sum of conduction current, which obeys Ohm's law ($\boldsymbol{\mathcal{J}_c} = \sigma\boldsymbol{\mathcal{E}}$ where σ is the material conductivity, S/m), and impressed current $\boldsymbol{\mathcal{J}_s}$, source of the system. The term $\frac{\partial}{\partial t}\boldsymbol{\mathcal{D}}$ represents instead the electric displacement current and, by symmetry, the contribution $\frac{\partial}{\partial t}\boldsymbol{\mathcal{B}}$ can be denoted as magnetic displacement current. Magnetic current density $\boldsymbol{\mathcal{M}}$ is usually introduced in the Maxwell's system in order to preserve symmetry and duality properties, even if magnetic currents and charges have not been observed in nature and thus can be omitted.

The same applies also to the continuity equations, which can be expressed in the differential form as

$$\nabla \cdot \boldsymbol{\mathcal{J}}(\boldsymbol{r}, t) = -\frac{\partial}{\partial t}\rho_e(\boldsymbol{r}, t), \tag{1.14}$$

$$\nabla \cdot \boldsymbol{\mathcal{M}}(\boldsymbol{r}, t) = -\frac{\partial}{\partial t}\rho_m(\boldsymbol{r}, t). \tag{1.15}$$

1.1.3 Maxwell's equations in frequency domain

Any time-harmonic vector can be written as the sum of its in-phase and in-quadrature components:

$$\boldsymbol{\mathcal{V}}(\boldsymbol{r}, t) = \boldsymbol{V'}(\boldsymbol{r})\cos(\omega t) - \boldsymbol{V''}(\boldsymbol{r})\sin(\omega t) = \Re\{(\boldsymbol{V'}(\boldsymbol{r}) + j\boldsymbol{V''}(\boldsymbol{r}))\, e^{j\omega t}\}. \tag{1.16}$$

In the previous notation, the complex vector $(\boldsymbol{V'} + j\boldsymbol{V''}) = \boldsymbol{V}$ is called phasor and, given constant angular frequency ω, contains the same amount of information of the original vector $\boldsymbol{\mathcal{V}}$. From there on, quantities in roman letters represent the complex phasors of the respective real-valued vector fields in time domain. Assuming time-harmonic dependence of all the quantities involved in the Maxwell's system, it is possible to rewrite them in terms of their phasors. This is really convenient because time derivatives, in the phasors domain, becomes simple scalar multiplications:

$$\frac{\partial}{\partial t}\boldsymbol{\mathcal{V}}(\boldsymbol{r}, t) = \Re(j\omega \boldsymbol{V}(\boldsymbol{r})\, e^{j\omega t}). \tag{1.17}$$

Since both sides of the equation includes real part operators and complex exponentials, they can be simplified to obtain

$$\nabla \times \boldsymbol{E}(\boldsymbol{r}, \omega) = -j\omega \boldsymbol{B}(\boldsymbol{r}, \omega) - \boldsymbol{M}(\boldsymbol{r}, \omega) \tag{1.18}$$

$$\nabla \times \boldsymbol{H}(\boldsymbol{r}, \omega) = j\omega \boldsymbol{D}(\boldsymbol{r}, \omega) + \boldsymbol{J}(\boldsymbol{r}, \omega) \tag{1.19}$$

$$\nabla \cdot \boldsymbol{B}(\boldsymbol{r}, \omega) = P_m(\boldsymbol{r}, \omega) \tag{1.20}$$

$$\nabla \cdot \boldsymbol{D}(\boldsymbol{r}, \omega) = P_e(\boldsymbol{r}, \omega). \tag{1.21}$$

Observing that the frequency-domain representation of Maxwell's equations can also be derived by applying the Fourier transform to the time-domain quantities involved is noteworthy. This observation implies that Eq. 1.18 - 1.21 are applicable not only to time-harmonic fields, but to any field with a generic spectrum that is integrable over the real numbers domain, i.e., any physically feasible one.

1.2 Electromagnetic field in free space

Solving Maxwell's equations, especially when paired with appropriate boundary conditions, presents significant challenges. Analytical solutions are rare and typically

limited to a few special scenarios, the most notable being radiation in free space, which refers to a homogeneous and infinitely vast expanse of space: This concept will be elaborated upon in this section. Note that in the difficulty in obtaining analytical solutions resides the critical need for efficient numerical solvers, which are the final aim of this thesis.

1.2.1 Electromagnetic radiation in free space

In physics, a wave is generally defined as a perturbation, impulsive or periodic, which propagates throughout space at a well-defined speed. Waves are originated by a source, and satisfy the wave equation which reads, for a scalar wave

$$\frac{\partial^2}{\partial t^2}\boldsymbol{\mathcal{E}} = \frac{1}{v^2}\nabla^2\boldsymbol{\mathcal{E}} \tag{1.22}$$

where $\nabla^2 = \nabla \cdot \nabla = \left(\frac{\partial^2}{\partial x^2} + \frac{\partial^2}{\partial y^2} + \frac{\partial^2}{\partial z^2}\right)$ is the spatial Laplacian Operator.

Starting from Maxwell's equations in differential form in a source-free region ($\rho_e = 0$ and $\boldsymbol{\mathcal{J}} = 0$), we have

$$\nabla \cdot \boldsymbol{\mathcal{E}} = 0, \tag{1.23}$$
$$\nabla \cdot \boldsymbol{\mathcal{B}} = 0, \tag{1.24}$$
$$\nabla \times \boldsymbol{\mathcal{E}} = -\frac{\partial \boldsymbol{\mathcal{B}}}{\partial t}, \tag{1.25}$$
$$\nabla \times \boldsymbol{\mathcal{B}} = \mu_0\epsilon_0\frac{\partial \boldsymbol{\mathcal{E}}}{\partial t}. \tag{1.26}$$

If we take the curl of Eq. 1.25, we obtain

$$\nabla \times (\nabla \times \boldsymbol{\mathcal{E}}) = -\frac{\partial}{\partial t}(\nabla \times \boldsymbol{\mathcal{B}}). \tag{1.27}$$

Using the vector identity $\nabla \times (\nabla \times \mathbf{A}) = \nabla(\nabla \cdot \mathbf{A}) - \nabla^2\mathbf{A}$ and substituting $\nabla \times \boldsymbol{\mathcal{B}}$ from Eq. 1.26, we get

$$\nabla^2\boldsymbol{\mathcal{E}} - \mu_0\epsilon_0\frac{\partial^2 \boldsymbol{\mathcal{E}}}{\partial t^2} = 0. \tag{1.28}$$

Similarly, switching the roles of Eq. 1.25 and 1.26, we derive

$$\nabla^2\boldsymbol{\mathcal{B}} - \mu_0\epsilon_0\frac{\partial^2 \boldsymbol{\mathcal{B}}}{\partial t^2} = 0. \tag{1.29}$$

These are the electromagnetic wave equations for electric field $\mathbf{E}$ and magnetic field $\mathbf{B}$, indicating that both fields propagate as waves with a speed $v = \frac{1}{\sqrt{\mu_0\epsilon_0}} = c_0$, i.e., the speed of light in vacuum.

Let's now investigate the fundamental properties of the electromagnetic field. Under the hypothesis that the electric and magnetic fields are time-harmonic waves, and assuming (without loss of generality) that they propagates toward the $\hat{x}$ direction, they will have an analytic form like

$$\boldsymbol{\mathcal{E}} = \boldsymbol{\mathcal{E}}_y\hat{y} + \boldsymbol{\mathcal{E}}_z\hat{z} = \boldsymbol{E}_{0,y}cos(kx - \omega t)\hat{y} + \boldsymbol{E}_{0,z}cos(kx - \omega t)\hat{z}, \tag{1.30}$$

$$\boldsymbol{\mathcal{B}} = \boldsymbol{\mathcal{B}}_y\hat{y} + \boldsymbol{\mathcal{B}}_z\hat{z} = \boldsymbol{B}_{0,y}cos(kx - \omega t)\hat{y} + \boldsymbol{B}_{0,z}cos(kx - \omega t)\hat{z}. \tag{1.31}$$

Applying Eq. 1.25, we obtain

$$\frac{\partial \boldsymbol{\mathcal{E}}_z}{\partial x} = \frac{\partial \boldsymbol{\mathcal{B}}_y}{\partial t} \tag{1.32}$$

$$-k\boldsymbol{E}_{0,z}sin(kx - \omega t) = \omega \boldsymbol{B}_{0,y}sin(kx - wt) \tag{1.33}$$

$$\boldsymbol{E}_{0,z} = -c_0\boldsymbol{B}_{0,y} \tag{1.34}$$

And, symmetrically, applying Eq. 1.26

$$\boldsymbol{E}_{0,y} = c_0\boldsymbol{B}_{0,z} \tag{1.35}$$

From Eq. 1.34 and 1.35 we can derive

$$\boldsymbol{E}^2 = \boldsymbol{E}_{0,y}^2 + \boldsymbol{E}_{0,z}^2 = c_0^2(\boldsymbol{B}_{0,y}^2 + \boldsymbol{B}_{0,z}^2) = c_0^2\boldsymbol{B}^2 \rightarrow \boldsymbol{E} = c_0\boldsymbol{B} \tag{1.36}$$

$$\boldsymbol{\mathcal{E}} \cdot \boldsymbol{\mathcal{B}} = \boldsymbol{\mathcal{E}}_y\boldsymbol{\mathcal{B}}_y + \boldsymbol{\mathcal{E}}_z\boldsymbol{\mathcal{B}}_z = 0. \tag{1.37}$$

These equations reveal us that (i) the electromagnetic field can propagate in vacuum without the need for any media, (ii) the two waves' magnitudes have a fixed relationship, (iii) the two waves are in phase and perpendicular in space. By a practical point of view, this allows us to compute only one of those two vector field, and to retrieve the other at the end of the calculations. A visualization of an electromagnetic wave is reported in Fig. 1.2.

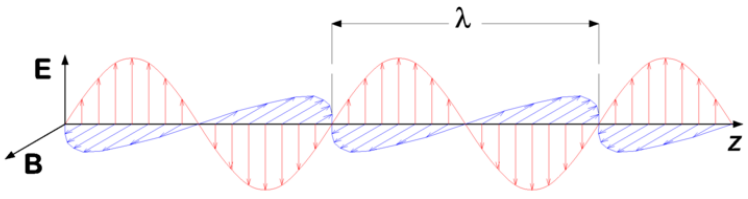

Figure 1.2: Visualization of an electromagetic wave propagating along the $\hat{z}$ direction with wavelength λ

1.2.2 Potentials for electric and magnetic fields

In the frequency domain, Maxwell's equations, specifically Eq. 1.18 and 1.19, reveal complexities when seeking solutions, particularly due to boundary conditions. These complexities are magnified by the assumption that only electric sources are present, excluding magnetic currents $\boldsymbol{M}$ and charges ρ_m. The assertion in Eq. 1.12 that magnetic flux density is solenoidal allows it to be represented as the curl of a vector field $\boldsymbol{A}(\boldsymbol{r})$, as permitted by the vector calculus identity $\nabla \cdot (\nabla \times \boldsymbol{A}) = 0$,

$$\boldsymbol{B}(\boldsymbol{r}) = \nabla \times \boldsymbol{A}(\boldsymbol{r}). \tag{1.38}$$

This expression introduces $\boldsymbol{A}(\boldsymbol{r})$ as determining the curl, while its divergence remains undefined. Substituting into Eq. 1.18 gives us

$$\nabla \times (\boldsymbol{E}(\boldsymbol{r}) + j\omega \boldsymbol{A}(\boldsymbol{r})) = 0. \tag{1.39}$$

Acknowledging that $\nabla \times \nabla \phi_e = 0$ allows for representing an irrotational field as the gradient of a scalr field, hence

$$\boldsymbol{E}(\boldsymbol{r}) + j\omega \boldsymbol{A}(\boldsymbol{r}) = -\nabla \phi_e(\boldsymbol{r}). \tag{1.40}$$

This indicates that the electric field, generated by the system's electric currents and charges, is expressible through both the vector field $\boldsymbol{A}(\boldsymbol{r})$ and the scalar field $\phi_e(\boldsymbol{r})$, termed electric vector and scalar potentials respectively, with units V·s/m and V. Manipulating these equations allows for establishing a direct relationship between the potentials and their sources. Implementing the potential definitions into Eq. 1.19 yields

$$\nabla \times \left(\frac{1}{\mu} \nabla \times \boldsymbol{A}(\boldsymbol{r}) \right) = j\omega\epsilon \left[-j\omega \boldsymbol{A}(\boldsymbol{r}) - \nabla \phi_e \right] + \boldsymbol{J}(\boldsymbol{r}), \tag{1.41}$$

which simplifies to

$$\nabla^2 \boldsymbol{A}(\boldsymbol{r}) + k^2 \boldsymbol{A}(\boldsymbol{r}) = \nabla(j\omega\mu\epsilon\phi_e(\boldsymbol{r}) + \nabla \cdot \boldsymbol{A}(\boldsymbol{r})) - \mu \boldsymbol{J}(\boldsymbol{r}), \tag{1.42}$$

introducing the wave number $k = \omega\sqrt{\mu\epsilon}$. Additionally, the divergence equation (Eq. 1.13) is rendered as

$$\nabla \cdot (-j\omega \boldsymbol{A}(\boldsymbol{r}) - \nabla \phi_e(\boldsymbol{r})) = -\frac{\rho_e(\boldsymbol{r})}{\epsilon}, \tag{1.43}$$

which simplifies further under the Lorenz gauge condition, which decouples scalar and vector potentials:

$$\nabla \cdot \boldsymbol{A}(\boldsymbol{r}) = -j\omega\mu\epsilon\phi_e(\boldsymbol{r}). \tag{1.44}$$

This choice enables the vector and scalar electric potentials to fulfill the inhomogeneous Helmholtz equation in their respective forms:

$$\nabla^2 \boldsymbol{A}(\boldsymbol{r}) + k^2 \boldsymbol{A}(\boldsymbol{r}) = -\mu \boldsymbol{J}(\boldsymbol{r}) \tag{1.45}$$

$$\nabla^2 \phi_e(\boldsymbol{r}) + k^2 \phi_e(\boldsymbol{r}) = -\frac{\rho_e(\boldsymbol{r})}{\epsilon}. \tag{1.46}$$

Note that the potentials, as well as the fields, satisfy the wave equations. The same procedure can be employed to find the potentials for magnetic sources

$$\nabla^2 \boldsymbol{F}(\boldsymbol{r}) + k^2 \boldsymbol{F}(\boldsymbol{r}) = -\epsilon \boldsymbol{M}(\boldsymbol{r}) \tag{1.47}$$

$$\nabla^2 \phi_m(\boldsymbol{r}) + k^2 \phi_m(\boldsymbol{r}) = -\frac{\rho_m(\boldsymbol{r})}{\mu} \tag{1.48}$$

however, note again that these sources are unobserved in nature.

1.2.3 Green's function and scattered field

The approach utilizing Green's function to find an analytic solution for the potentials involves solving the inhomogeneous Helmholtz equation. This method relies on determining the solution for a point source excitation, depicted by a Dirac delta function, and is known as the Green's function or fundamental solution, symbolized by g. The original Helmholtz equation's solution is then derived by convolving g with the actual source, leveraging the superposition principle. Mathematically, the Green's function is defined to satisfy:

$$\nabla^2 g(\boldsymbol{r}) + k^2 g(\boldsymbol{r}) = -\delta(\boldsymbol{r}), \tag{1.49}$$

where the equation has a unique solution only under the boundary condition that imposes the existence of only outgoing waves at infinity, known as Sommerfeld's radiation condition. The expression for the three-dimensional free space Green's function is given by:

$$g(\boldsymbol{r}) = \frac{e^{-jk|\boldsymbol{r}|}}{4\pi|\boldsymbol{r}|} \;\; \textit{if } k{>}0, \tag{1.50}$$

$$g_0(\boldsymbol{r}) = \frac{1}{4\pi|\boldsymbol{r}|} \;\; \textit{if } k{=}0 \tag{1.51}$$

By convolving both sides of eq. (1.49) with the right hand sides of equations 1.45, 1.46, 1.47, 1.48 and comparing what obtained with the just mentioned equations, potentials $\boldsymbol{A}$, ϕ_e, $\boldsymbol{F}$, ϕ_m are respectively obtained as

$$\boldsymbol{A}(\boldsymbol{r}) = \mu \iiint_{r' \in \mathbb{R}^3} g(\boldsymbol{r} - \boldsymbol{r'}) \boldsymbol{J}(\boldsymbol{r'}) dV' \tag{1.52}$$

$$\phi_e(\boldsymbol{r}) = \frac{1}{\epsilon} \iiint_{r' \in \mathbb{R}^3} g(\boldsymbol{r} - \boldsymbol{r'}) \rho_e(\boldsymbol{r'}) dV' \tag{1.53}$$

$$\boldsymbol{F}(\boldsymbol{r}) = \epsilon \iiint_{r' \in \mathbb{R}^3} g(\boldsymbol{r} - \boldsymbol{r'}) \boldsymbol{M}(\boldsymbol{r'}) dV' \tag{1.54}$$

$$\phi_m(\boldsymbol{r}) = \frac{1}{\mu} \iiint_{r' \in \mathbb{R}^3} g(\boldsymbol{r}\boldsymbol{r'}) \rho_m(\boldsymbol{r'}) dV'. \tag{1.55}$$

To perform this convolution, we use the property that the convolution of the Green's function with the source term of a differential equation gives the solution to that differential equation. The convolution process effectively "spreads" the influence of the point source $\delta(\boldsymbol{r})$ across the space where the current density $\boldsymbol{J}(\boldsymbol{r'})$ is nonzero, weighted by the Green's function $g(\boldsymbol{r} - \boldsymbol{r'})$ which accounts for the propagation effects between the source point $\boldsymbol{r'}$ and the observation point $\boldsymbol{r}$.

Summing up the contributions, electric and magnetic fields scattered from both electric and magnetic sources are written as

$$\boldsymbol{E}(\boldsymbol{r}) = -j\omega \boldsymbol{A}(\boldsymbol{r}) - \nabla \phi_e(\boldsymbol{r}) - \frac{1}{\epsilon} \nabla \times \boldsymbol{F}(\boldsymbol{r}) \tag{1.56}$$

$$\boldsymbol{H}(\boldsymbol{r}) = -j\omega \boldsymbol{F}(\boldsymbol{r}) - \nabla \phi_m(\boldsymbol{r}) + \frac{1}{\mu} \nabla \times \boldsymbol{A}(\boldsymbol{r}) \tag{1.57}$$

or equivalently, given the Lorenz gauge considered, as

$$\boldsymbol{E}(\boldsymbol{r}) = -j\omega \boldsymbol{A}(\boldsymbol{r}) + \frac{1}{j\omega\mu\epsilon} \nabla \nabla \cdot \boldsymbol{A}(\boldsymbol{r}) - \frac{1}{\epsilon} \nabla \times \boldsymbol{F}(\boldsymbol{r}) \tag{1.58}$$

$$\boldsymbol{H}(\boldsymbol{r}) = -j\omega \boldsymbol{F}(\boldsymbol{r}) + \frac{1}{j\omega\mu\epsilon} \nabla \nabla \cdot \boldsymbol{F}(\boldsymbol{r}) + \frac{1}{\mu} \nabla \times \boldsymbol{A}(\boldsymbol{r}). \tag{1.59}$$

2D formulations

The Green function 2D formulation can be obtained starting from the 2D Helmholtz equation for the Green's function

$$\nabla^2 g^{2D}(\boldsymbol{r}) + k^2 g^{2D}(\boldsymbol{r}) = -\delta(\boldsymbol{r}) \tag{1.60}$$

and from the two-dimensional (2D) free space Green's function, expressed as

$$g^{2D}(\boldsymbol{r}, \boldsymbol{r'}) \coloneqq -\frac{\mathrm{i}}{4} H_0^{(2)}(k|\boldsymbol{r} - \boldsymbol{r'}|) \ \textit{if } k{>}0, \tag{1.61}$$

$$g_0^{2D}(\boldsymbol{r}, \boldsymbol{r'}) \coloneqq -\frac{1}{2\pi} \log(|\boldsymbol{r} - \boldsymbol{r'}|) \ \textit{if } k{=}0 \tag{1.62}$$

where $H_0^{(2)}$ denotes the Hankel function of the second kind and zeroth order, accounting for the cylindrical wave propagation in a 2D medium.

from 1.60, 1.62 and from the potentials 1.45 - 1.48, by convolving the Green's function $g^{2D}(\boldsymbol{r}-\boldsymbol{r'})$ with the source terms in 2D, we find the expression for the vector potentials in the two-dimensional space. The convolution delivers:

$$\boldsymbol{A}^{2D}(\boldsymbol{r}) = \mu \iint_{r'\in\mathbb{R}^2} g^{2D}(\boldsymbol{r}-\boldsymbol{r'})\boldsymbol{J}(\boldsymbol{r'})dA' \tag{1.63}$$

$$\phi_e^{2D}(\boldsymbol{r}) = \frac{1}{\epsilon} \iint_{r'\in\mathbb{R}^2} g^{2D}(\boldsymbol{r}-\boldsymbol{r'})\rho_e(\boldsymbol{r'})dA' \tag{1.64}$$

$$\boldsymbol{F}^{2D}(\boldsymbol{r}) = \epsilon \iint_{r'\in\mathbb{R}^2} g^{2D}(\boldsymbol{r}-\boldsymbol{r'})\boldsymbol{M}(\boldsymbol{r'})dA' \tag{1.65}$$

$$\phi_m^{2D}(\boldsymbol{r}) = \frac{1}{\mu} \iint_{r'\in\mathbb{R}^2} g^{2D}(\boldsymbol{r}\boldsymbol{r'})\rho_m(\boldsymbol{r'})dA', \tag{1.66}$$

where dA' represents the area element in the plane of integration, and the integral is taken over the 2D space $\mathbb{R}^2$. Equations 1.56 - 1.59 holds also in 2D, replacing the quantities with the respective planar ones.

1.3 Maxwell's equations in statics

In the scenario where the frequency is precisely zero, the electric ($\boldsymbol{E}$) and magnetic ($\boldsymbol{H}$) fields are entirely decoupled, leading to Maxwell's equations being expressed as:

$$\nabla \times \boldsymbol{E}(\boldsymbol{r},\omega) = -\boldsymbol{M}(\boldsymbol{r},\omega) \tag{1.67}$$

$$\nabla \times \boldsymbol{H}(\boldsymbol{r},\omega) = \boldsymbol{J}(\boldsymbol{r},\omega). \tag{1.68}$$

When considering only physical (electrical) sources, eq. (1.67) implies that the electric field is irrotational, rendering it conservative over simply connected domains:

$$\oint_C \boldsymbol{E}\cdot d\boldsymbol{l} = 0 \quad , \tag{1.69}$$

reflecting the conservation of electric potential ϕ_e. This principle, recognizing the path-independence of potential difference, or voltage, is better recognized as Kirchhoff's Voltage Law (KVL). The relation $E = -\nabla\phi_e$ (where E is in Volts per meter, V/m) is merely a specific case of eq. (1.40) under static conditions with only electric sources.

Kirchhoff's Current Law (KCL), another foundational concept in circuit analysis, emerges from eq. (1.68). By defining the current I in Amperes flowing through an

open surface S_o bounded by contour C_o and applying Stokes' theorem, a relationship involving the magnetic field's circulation is established:

$$I = \iint_{S_o} \boldsymbol{J}(\boldsymbol{r}) \cdot d\boldsymbol{S} = \iint_{S_o} (\nabla \times \boldsymbol{H}(\boldsymbol{r})) \cdot d\boldsymbol{S} = \oint_{C_o} \boldsymbol{H}(\boldsymbol{r}) \cdot d\boldsymbol{l}, \tag{1.70}$$

where $\boldsymbol{J}$ is in Amperes per square meter ($\mathrm{A/m^2}$), $\boldsymbol{H}$ is in Amperes per meter (A/m), and $d\boldsymbol{S}$ and $d\boldsymbol{l}$ are in square meters ($\mathrm{m^2}$) and meters (m), respectively. These relationships also hold for a closed surface S_c, whose enclosing contour C_c diminishes to zero, indicating that the net current passing through the closed surface S_c is zero, embodying the essence of KCL.

1.3.1 quasi-static regime

Note that any physically feasible quantity cannot have *exact* zero frequency, or in other words, a null spectrum. This statement underscores a fundamental principle in physics, where absolute static conditions (zero frequency) are idealized concepts rather than practical realities.

In light of this, the quasi-static regime emerges as a critical conceptual framework. This regime is characterized by frequencies that are sufficiently low so that the wave nature of electromagnetic phenomena can be neglected in some aspects, yet the effects of time variation cannot be entirely ignored. From a conceptual viewpoint, the quasi-static regime allows for the application of static field approximations to systems experiencing slow temporal changes.

In the quasi-static regime, the retardation effects due to the finite speed of electromagnetic wave propagation are minimal, and the electromagnetic fields at any point in space can be approximated as responding instantaneously to changes in sources. However, this does not mean that time variations are absent; rather, they are present but occur over time scales long enough that the fields can be considered quasi-static. This approach facilitates the analysis of complex electromagnetic problems by simplifying the mathematical models.

The applicability conditions of this regime depends on two main factors:

- the ratio among the maximum physical size of the object l_{max} under analysis and the minimum wavelength λ_{min}(i.e., maximum frequency) involved

- the needed precision of the analysis

As a rule of thumb, for average accuracy results, if $l_{max} < \frac{1}{10}\lambda_{min}$, the quasi-static approximation can be employed.

1.4 Integral equation formulation

In this section, we will move from the Maxwell equations to the so-called integral Equations, which deals with real-world scattering problems. We will start by introducing the correct boundary conditions, then we will use Love formulation to reshape the problem in a more convenient way, and finally we will manipulate the formulations to make them more compact and expressive.

1.4.1 Boundary conditions

The differential form of Maxwell's system is not applicable in the presence of material discontinuities, as the fields or their derivatives may not exhibit continuity at the interfaces between different media. However, certain relationships between the inner and outer limits of the electric and magnetic fields at these interfaces can be deduced from Maxwell's equations in their integral form, which remains valid under any circumstances.

Let us consider a spatial region denoted by Ω_1 and its smoothly defined boundary Γ, characterized by the outward unit normal vector $\hat{\boldsymbol{n}}$. The field limits at the boundary, external and internal to the region Ω_1, are indicated respectively with the superscripts $^{0/1}$. These field limits obey the following boundary conditions:

$$\hat{\boldsymbol{n}} \times (\boldsymbol{E}^0 - \boldsymbol{E}^1) = -\boldsymbol{m}_s, \tag{1.71}$$

$$\hat{\boldsymbol{n}} \times (\boldsymbol{H}^0 - \boldsymbol{H}^1) = \boldsymbol{j}_s, \tag{1.72}$$

$$\hat{\boldsymbol{n}} \cdot (\boldsymbol{D}^0 - \boldsymbol{D}^1) = \rho_{e,s}, \tag{1.73}$$

$$\hat{\boldsymbol{n}} \cdot (\boldsymbol{B}^0 - \boldsymbol{B}^1) = \rho_{m,s}. \tag{1.74}$$

In these equations, the subscript $_s$ denotes surface quantities: surface current densities in A/m and V/m, and surface charge densities in A $\cdot$ s/m^2 and V $\cdot$ s/m^2.

These pairs of conditions are interrelated, and typically, only the first condition is explicitly applied in the formulation of integral equations. It is also essential to note that in the context of real materials, surface currents and charges are absent, leading to the familiar conditions for the continuity of the tangential components of the fields and the normal components of the flux densities. Conversely, the surface of a perfect electric conductor (PEC) may accommodate surface electric currents and charges, while surface magnetic currents and charges are theoretically feasible on the surface of a perfect magnetic conductor (PMC). Note that PEC and PMC does not exist in nature, however, they are useful mathematical concepts. It is also noteworthy that metal artifacts can often be approximated as PECs.

1.4.2 Love formulation and surface equivalence principle

The Surface Equivalence Principle posits that the electromagnetic field within any region devoid of sources, denoted as Ω, can be entirely determined by knowing the tangential components of the electric and magnetic fields along the boundary $\Gamma = \partial\Omega$. This principle is crucial for formulating boundary integral equations, which recast the original problem into a new, equivalent free-space scattering issue, with the analytic solution discussed in Section 1.2.

For instance, take the scattering problem involving an object Ω_1, endowed with material parameters (ϵ_1, μ_1), and subjected to excitation from the external region $\Omega_0 = \mathbb{R}^3 \backslash \Omega_1$, characterized by (ϵ_0, μ_0) (refer to Figure 1.3). The demarcation between Ω_0 and Ω_1 is the smooth interface Γ, at each point of which the outgoing (relative to Ω_1) unit surface normal vector $\hat{\boldsymbol{n}}$ is defined. The incident excitation $(\boldsymbol{E}^{inc}, \boldsymbol{H}^{inc})$ induces currents within Ω_1, denoted as $(\boldsymbol{j}, \boldsymbol{m})$, which, in turn, are the sources for the scattered fields $(\boldsymbol{E}^{sc}, \boldsymbol{H}^{sc})$. The process of determining the scattered field from the known incident field constitutes the direct scattering problem.

To evaluate the total field, which is the superposition of the incident and scattered fields, it is necessary not only to identify the currents $(\boldsymbol{j}, \boldsymbol{m})$ but also to understand the scattering operators, i.e., the Green's function tailored to the geometry and material parameters being investigated, which connects the scattered fields back to their sources. Typically, this intricate information is unattainable for scatterers with non-canonical shapes.

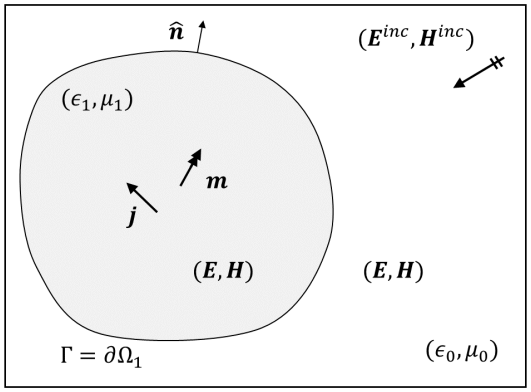

Figure 1.3: Illustration of the original direct scattering problem.

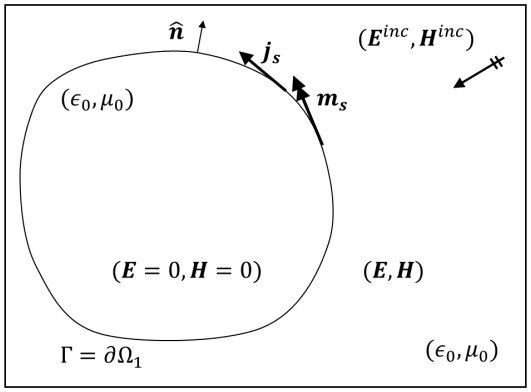

Figure 1.4: Depiction of Love's equivalent formulation for the exterior scattering problem.

On the other hand, the solution to free-space electromagnetic scattering is well-known, as elucidated in Section 1.2. Utilizing the Surface Equivalence Principle, the original problem can be transitioned into a free-space scattering scenario. This necessitates substituting the actual fields inside the scatterer $(\boldsymbol{E}, \boldsymbol{H})$ and the real

(if present) surface current densities $(\boldsymbol{j}_{s,0}, \boldsymbol{m}_{s,0})$ at the boundary with alternative quantities, labelled as $(\boldsymbol{E}', \boldsymbol{H}')$, $(\boldsymbol{j}_s, \boldsymbol{m}_s)$, which contain an equivalent amount of information, thus leaving the external fields unchanged. Specifically, the new and original problems in Ω_0 are equivalent if the boundary conditions

$$\hat{\boldsymbol{n}} \times (\boldsymbol{E}^0 - \boldsymbol{E}'^1) = -\boldsymbol{m}_s, \tag{1.75}$$

$$\hat{\boldsymbol{n}} \times (\boldsymbol{H}^0 - \boldsymbol{H}'^1) = \boldsymbol{j}_s, \tag{1.76}$$

are met. A judicious selection is Love's formulation, which sets interior fields to zero (the scattered fields negate the incident ones), necessitating that the unknown surface current densities fulfill

$$\hat{\boldsymbol{n}} \times \boldsymbol{E}^0 = -\boldsymbol{m}_s, \tag{1.77}$$

$$\hat{\boldsymbol{n}} \times \boldsymbol{H}^0 = \boldsymbol{j}_s. \tag{1.78}$$

Given the nullity of electric and magnetic fields inside Ω_1, the material parameters of the scatterer can be substituted with (ϵ_0, μ_0) from the surrounding medium without altering the problem's essence. Consequently, a free-space scattering scenario is achieved: the external scattered fields $(\boldsymbol{E}^{sc}, \boldsymbol{H}^{sc})$ can be deduced from the scattering of fictitious surface currents $(\boldsymbol{j}_s, \boldsymbol{m}_s)$ via formulas 1.58 and 1.59. As these currents $(\boldsymbol{j}_s, \boldsymbol{m}_s)$ are defined over a surface rather than a volume, the electric and magnetic vector potentials can be reformulated as

$$\boldsymbol{A}(\boldsymbol{r}) = \mu \iint_{r' \in \Gamma} G(\boldsymbol{r} - \boldsymbol{r}') \boldsymbol{j}_s(\boldsymbol{r}') dS', \tag{1.79}$$

$$\boldsymbol{F}(\boldsymbol{r}) = \epsilon \iint_{r' \in \Gamma} G(\boldsymbol{r} - \boldsymbol{r}') \boldsymbol{m}_s(\boldsymbol{r}') dS'. \tag{1.80}$$

Note that these equations are in a 3D setting, and the involved integral operators are only over the 2D manifold Γ. This, by a computational point of view, is of great interest, because it almost directly reflects in a complexity improvement as we will see later.

1.4.3 The electric and magnetic field integral equations

The Electric and Magnetic Field Integral Equations (EFIE and MFIE) stand as two pivotal integral equations within the realm of computational electromagnetics. These equations are derived from the boundary conditions 1.71 and 1.72, corresponding to the electric and magnetic fields, respectively.

In light of the scattering problem delineated in section 1.4.2 and subsequently reformulated through the Love's formulation of the surface equivalence principle (as per equations 1.77 and 1.78), a preliminary formulation of both EFIE and MFIE is hereby introduced:

$$\hat{\boldsymbol{n}}(\boldsymbol{r}) \times (\boldsymbol{E}^{inc}(\boldsymbol{r}) + \boldsymbol{E}^{sc}(\boldsymbol{r})) = -\boldsymbol{m}_s(\boldsymbol{r}) \tag{1.81}$$

$$\hat{\boldsymbol{n}}(\boldsymbol{r}) \times (\boldsymbol{H}^{inc}(\boldsymbol{r}) + \boldsymbol{H}^{sc}(\boldsymbol{r})) = \boldsymbol{j}_s(\boldsymbol{r}). \tag{1.82}$$

However, these expressions do not allow to compute the fields in an efficient way. In this section, we will introduce operators which facilitate the rewriting of the EFIE and MFIE in a more tractable form, ultimately enabling the solution of the exterior scattering problem.

Scattered fields reformulation

The scattered fields $(\boldsymbol{E}^{sc}, \boldsymbol{H}^{sc})$ are described through the radiation formulae 1.58 and 1.59 that incorporate potentials as outlined in eq. (1.79) and eq. (1.80). This step necessitates careful consideration due to the presence of singularities in the potentials' expressions when evaluated at the boundary Γ.

Before delving into the behavior of potentials at the boundary, it is useful to rearrange certain terms in eq. (1.58) and eq. (1.59) using vector calculus identities, allowing the derivative operators to be moved within the surface integrals. This manipulation yields the identities:

$$\nabla \cdot \iint_{r' \in \Gamma} G(\boldsymbol{r} - \boldsymbol{r'}) \boldsymbol{f}(\boldsymbol{r'}) dS' = \iint_{r' \in \Gamma} G(\boldsymbol{r} - \boldsymbol{r'}) \nabla' \cdot \boldsymbol{f}(\boldsymbol{r'}) dS', \tag{1.83}$$

$$\nabla \times \iint_{r' \in \Gamma} G(\boldsymbol{r} - \boldsymbol{r'}) \boldsymbol{f}(\boldsymbol{r'}) dS' = \iint_{r' \in \Gamma} \nabla G(\boldsymbol{r} - \boldsymbol{r'}) \times \boldsymbol{f}(\boldsymbol{r'}) dS', \tag{1.84}$$

where $\boldsymbol{f}$ represents $\boldsymbol{j}_s$ or $\boldsymbol{m}_s$, and primed operators act with respect to the primed variable $\boldsymbol{r'}$.

The advantage of these latter formulations lies in their capacity to simplify the computational process for evaluating the scattered fields. By transferring the differentiation operations inside the integrals, the complexity associated with handling boundary conditions and singularities is effectively reduced. This approach not only facilitates a more straightforward computation of the fields but also enhances the accuracy of the numerical solutions by directly addressing the derivatives of the potentials within the integrals.

Behavior of potentials on the surface

The jump relations reported in 1.4.4 for the scalar operators and better detailed in [2], elucidate the continuity of tangential traces for terms $\boldsymbol{A}(\boldsymbol{r})$ and $\nabla\nabla \cdot \boldsymbol{A}(\boldsymbol{r})$ in equation 1.58 across the boundary. More specifically, for $\boldsymbol{r}_0 \in \Gamma$,

$$\lim_{\boldsymbol{r} \to \boldsymbol{r}_0} \hat{\boldsymbol{n}}(\boldsymbol{r}) \times \boldsymbol{A}(\boldsymbol{r}) = \hat{\boldsymbol{n}}(\boldsymbol{r}_0) \times \boldsymbol{A}(\boldsymbol{r}_0) \tag{1.85}$$

$$\lim_{\boldsymbol{r} \to \boldsymbol{r}_0} \hat{\boldsymbol{n}}(\boldsymbol{r}) \times (\nabla\nabla \cdot \boldsymbol{A}(\boldsymbol{r})) = \hat{\boldsymbol{n}}(\boldsymbol{r}_0) \times (\nabla\nabla \cdot \boldsymbol{A}(\boldsymbol{r}_0)) \,. \tag{1.86}$$

Moreover, the tangential trace of the curl of $\boldsymbol{F}$ is identified as discontinuous across Γ, with the discontinuity magnitude defined by the tangential component of $\boldsymbol{m}_s(\boldsymbol{r})$. Hence, for $\boldsymbol{r} \in \Omega_{0/1}$,

$$\lim_{\boldsymbol{r}\to\boldsymbol{r}_0} \hat{\boldsymbol{n}}(\boldsymbol{r}) \times (\nabla \times \boldsymbol{F}(\boldsymbol{r})) = \pm\frac{1}{2}\boldsymbol{m}_s(\boldsymbol{r}_0) + \hat{\boldsymbol{n}}(\boldsymbol{r}_0) \times p.v. \iint_{r'\in\Gamma} \nabla G(\boldsymbol{r}-\boldsymbol{r'}) \times \boldsymbol{m_s}(\boldsymbol{r'}) dS'. \quad (1.87)$$

Note that the notation $p.v.$ stands for "principal value," a method used to define and evaluate integrals that may not converge due to singularities. It is calculated by symmetrically excluding a small neighborhood around the singularity and then taking the limit as this neighborhood approaches zero. Formally, for a function f with a singularity at a, the principal value of the integral over a domain Ω is defined as:

$$p.v. \int_\Omega f(x)\,dx = \lim_{\epsilon\to 0} \left(\int_{\Omega\setminus[a-\epsilon,a+\epsilon]} f(x)\,dx \right). \quad (1.88)$$

Similar results can be obtained also for the terms in equation 1.59 relative to magnetic scattering. Finally, tangential traces of the scattered fields $(\boldsymbol{E}^{sc}, \boldsymbol{H}^{sc})$ evaluated in points $\boldsymbol{r}$ approaching the surface Γ from outside are rewritten as

$$\begin{aligned}
\hat{\boldsymbol{n}}(\boldsymbol{r}) \times \boldsymbol{E}^{sc}(\boldsymbol{r}) = &-jk\eta\hat{\boldsymbol{n}}(\boldsymbol{r}) \times \iint_{\boldsymbol{r}'\in\Gamma} G(\boldsymbol{r}-\boldsymbol{r}')\boldsymbol{j}_s(\boldsymbol{r}')d\boldsymbol{r}' \\
&+ \frac{\eta}{jk}\hat{\boldsymbol{n}}(\boldsymbol{r}) \times \nabla \iint_{\boldsymbol{r}'\in\Gamma} G(\boldsymbol{r}-\boldsymbol{r}')\nabla'\cdot\boldsymbol{j}_s(\boldsymbol{r}')d\boldsymbol{r}' \\
&- \frac{1}{2}\boldsymbol{m}_s \\
&- \hat{\boldsymbol{n}}(\boldsymbol{r}) \times \text{p.v.} \iint_{\boldsymbol{r}'\in\Gamma} \nabla G(\boldsymbol{r}-\boldsymbol{r}') \times \boldsymbol{m}_s(\boldsymbol{r}')d\boldsymbol{r}' \quad (1.89) \\
\hat{\boldsymbol{n}}(\boldsymbol{r}) \times \boldsymbol{H}^{sc}(\boldsymbol{r}) = &-\frac{jk}{\eta}\hat{\boldsymbol{n}}(\boldsymbol{r}) \times \iint_{\boldsymbol{r}'\in\Gamma} G(\boldsymbol{r}-\boldsymbol{r}')\boldsymbol{m}_s(\boldsymbol{r}')d\boldsymbol{r}' \\
&+ \frac{1}{jk\eta}\hat{\boldsymbol{n}}(\boldsymbol{r}) \times \nabla \iint_{\boldsymbol{r}'\in\Gamma} G(\boldsymbol{r}-\boldsymbol{r}')\nabla'\cdot\boldsymbol{m}_s(\boldsymbol{r}')d\boldsymbol{r}' \\
&+ \frac{1}{2}\boldsymbol{j}_s \\
&+ \hat{\boldsymbol{n}}(\boldsymbol{r}) \times \text{p.v.} \iint_{\boldsymbol{r}'\in\Gamma} \nabla G(\boldsymbol{r}-\boldsymbol{r}') \times \boldsymbol{j}_s(\boldsymbol{r}')d\boldsymbol{r}', \quad (1.90)
\end{aligned}$$

where η is the impedance of background medium. By substituting these expressions in equations 1.81 and 1.82, the electric and magnetic field integral equations are redefined in terms of only incident fields and surface currents. In order to shorten these expressions, it is convenient to introduce surface integral operators.

Surface integral operators

The electric field integral operator $\mathcal{T}_k$ is constructed from a linear combination of the vector and scalar electric potential operators, namely $\mathcal{T}_{\boldsymbol{A},k}$ and $\mathcal{T}_{\phi,k}$:

$$\mathcal{T}_k = -jk\mathcal{T}_{\boldsymbol{A},k} + \frac{1}{jk}\mathcal{T}_{\phi,k} \tag{1.91}$$

$$(\mathcal{T}_{\boldsymbol{A},k}\boldsymbol{f})(\boldsymbol{r}) = \hat{\boldsymbol{n}}(\boldsymbol{r}) \times \iint_\Gamma G_k(\boldsymbol{r},\boldsymbol{r}')\boldsymbol{f}(\boldsymbol{r}')d\boldsymbol{r}' \tag{1.92}$$

$$(\mathcal{T}_{\phi,k}\boldsymbol{f})(\boldsymbol{r}) = \hat{\boldsymbol{n}}(\boldsymbol{r}) \times \nabla \iint_\Gamma G_k(\boldsymbol{r},\boldsymbol{r}')\nabla' \cdot \boldsymbol{f}(\boldsymbol{r}')d\boldsymbol{r}'. \tag{1.93}$$

Similarly, the magnetic field integral operator, $\mathcal{K}_k$, is articulated as

$$(\mathcal{K}_k\boldsymbol{f})(\boldsymbol{r}) = \hat{\boldsymbol{n}}(\boldsymbol{r}) \times \iint_\Gamma \nabla G_k(\boldsymbol{r},\boldsymbol{r}') \times \boldsymbol{f}(\boldsymbol{r}')d\boldsymbol{r}'. \tag{1.94}$$

These operators are instrumental in expressing the Electric Field Integral Equation (EFIE) and the Magnetic Field Integral Equation (MFIE) for the exterior scattering problem, finally in a compact and expressive form:

$$-\hat{\boldsymbol{n}} \times \boldsymbol{E}^{inc} = \eta\mathcal{T}_k\boldsymbol{j}_s + \frac{1}{2}\boldsymbol{m}_s - \mathcal{K}_k\boldsymbol{m}_s \tag{1.95}$$

$$\hat{\boldsymbol{n}} \times \boldsymbol{H}^{inc} = -\frac{1}{\eta}\mathcal{T}_k\boldsymbol{m}_s + \frac{1}{2}\boldsymbol{j}_s - \mathcal{K}_k\boldsymbol{j}_s. \tag{1.96}$$

When structured in a matrix block form, the solution system derived from eq. (1.95) and eq. (1.96) becomes

$$\begin{pmatrix} \eta\mathcal{T}_k & \frac{\mathcal{I}}{2} - \mathcal{K}_k \\ \frac{\mathcal{I}}{2} - \mathcal{K}_k & -\frac{1}{\eta}\mathcal{T}_k \end{pmatrix} \begin{pmatrix} \boldsymbol{j}_s \\ \boldsymbol{m}_s \end{pmatrix} = \begin{pmatrix} -\hat{\boldsymbol{n}} \times \boldsymbol{E}^{inc} \\ \hat{\boldsymbol{n}} \times \boldsymbol{H}^{inc} \end{pmatrix}, \tag{1.97}$$

solving for the surface currents $(\boldsymbol{j}_s, \boldsymbol{m}_s)$, which address the exterior scattering problem.

1.4.4 Scalar operators and jump relations

Single and double layer potentials and the hypersingular operator, scalar operators inherited from the acoustic [3–5], are defined as

$$(\mathcal{S}v)(\boldsymbol{r}) = \iint_\Gamma G(\boldsymbol{r}-\boldsymbol{r}')v(\boldsymbol{r}')dS' \quad \boldsymbol{r}\in\mathbb{R}^3\backslash\Gamma\,, \tag{1.98}$$

$$(\mathcal{D}v)(\boldsymbol{r}) = \iint_\Gamma \frac{\partial}{\partial n'}G(\boldsymbol{r}-\boldsymbol{r}')v(\boldsymbol{r}')dS' \quad \boldsymbol{r}\in\mathbb{R}^3\backslash\Gamma\,. \tag{1.99}$$

$$(\mathcal{D}^*v)(\boldsymbol{r}) = \frac{\partial}{\partial n}\iint_\Gamma G(\boldsymbol{r}-\boldsymbol{r}')v(\boldsymbol{r}')dS' \quad \boldsymbol{r}\in\mathbb{R}^3\backslash\Gamma\,, \tag{1.100}$$

$$(\mathcal{N}v)(\boldsymbol{r}) = -\frac{\partial}{\partial n}\iint_\Gamma \frac{\partial}{\partial n'}G(\boldsymbol{r}-\boldsymbol{r}')v(\boldsymbol{r}')dS' \quad \boldsymbol{r}\in\mathbb{R}^3\backslash\Gamma \tag{1.101}$$

where n, by convention, points toward the outside. Those are harmonic operators, embodying solutions to the Laplace equation within the domain $\mathbb{R}^3\backslash\Gamma$ for any scalar function v.

The properties associated with these potentials are well established, and represent the so-called jump relations:

- The single layer potential exhibits continuity across Γ: $[\mathcal{S}\phi] = 0$.
- Conversely, the double layer potential demonstrates discontinuity across Γ: $[\mathcal{D}\psi] = \psi$.
- The normal derivative of the single layer potential is discontinuous across Γ: $[\gamma_1\mathcal{S}\phi] = -\phi$.
- The normal derivative of the double layer potential maintains continuity across Γ: $[\gamma_1\mathcal{D}\psi] = 0$.

For comprehensive formalism and validations of these principles, one can refer to [3, 4].

Although EM integral operators are vector ones, we will see in the following how under certain hypothesis they can be expressed in terms of scalar ones, and specifically in terms of these operators. In practice, this can be leveraged to obtain fast EM solvers out of fast strategies to compute those operators, that is indeed simpler than dealing with the vector ones. We will now see a first application of this procedure, in the 2D setting, and a second one in 2.2, with Helmholtz decomposition.

1.4.5 TE and TM Modes in the 2D setting

To further simplify the expressions, without loosing generality, we can introduce the definition of Transverse Electric (TE) and Transverse Magnetic (TM) modes

in both EFIE and MFIE in the bidimensional setting. These modes refer to the incidence on the impinging electromagnetic field with respect to the manifold. As illustrated in Fig. 1.5 (where the example scatterer is a PEC cylinder), TE modes represents fields with the electric component on the xy plane, whereas TM modes represents fields with the magnetic component on the xy plane. Note that, in the 2D setting, the fields can only propagate on the xy plane by definitions, i.e., $\hat{\boldsymbol{k}}^{2D} \in xy$. With this notation, we can now express any 2D field as a composition

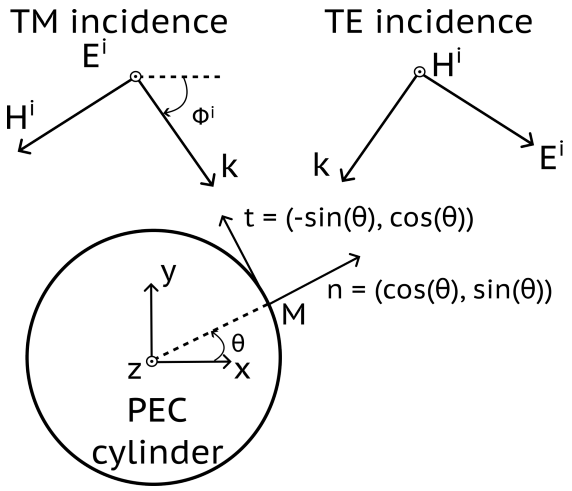

Figure 1.5: Polarization definitions and other useful notations for the 2D setting

of a TE and TM field, denoting

$$\boldsymbol{E} = \boldsymbol{E}_t + \boldsymbol{E}_z = E_t\hat{\boldsymbol{t}} + E_z\hat{\boldsymbol{z}}\,, \tag{1.102}$$

$$\boldsymbol{H} = \boldsymbol{H}_t + \boldsymbol{H}_z = H_t\hat{\boldsymbol{t}} + H_z\hat{\boldsymbol{z}}\,, \tag{1.103}$$

$$\boldsymbol{j_s} = \boldsymbol{j}_{s,t} + \boldsymbol{j}_{s,z} = j_{s,t}\hat{\boldsymbol{t}} + j_{s,z}\hat{\boldsymbol{z}}\,, \tag{1.104}$$

$$\boldsymbol{m_s} = \boldsymbol{m}_{s,t} + \boldsymbol{m}_{s,z} = m_{s,t}\hat{\boldsymbol{t}} + m_{s,z}\,.\hat{\boldsymbol{z}} \tag{1.105}$$

IN this setting, the TE-EFIE can be derived from 1.95 in terms of scalar operators, as described in [6] at chapter 10.2, obtaining

$$\boldsymbol{E}_t^{inc} = \eta\frac{1}{jk}\mathcal{N}_{2D}\boldsymbol{j}_{s,t}\,. \tag{1.106}$$

where

$$(\mathcal{N}_{2D}v)(\boldsymbol{r}) = -\frac{\partial}{\partial n}\int_\gamma \frac{\partial}{\partial n'}G(\boldsymbol{r}-\boldsymbol{r}')v(\boldsymbol{r}')d\boldsymbol{r}' \quad \boldsymbol{r}\in\mathbb{R}^2\backslash\gamma \tag{1.107}$$

is the 2D-equivalent of 1.101.

Following a parallel procedure, we can rewrite 1.95 - 1.96 as

$$\boldsymbol{E}_z^{inc} = \eta j k \mathcal{S}_{2D} \boldsymbol{j}_{s,z} \,, \tag{1.108}$$

$$\boldsymbol{H}_z^{inc} = \Big(-\frac{1}{2} I + \mathcal{D}_{2D} \Big) \boldsymbol{j}_{s,t} \,, \tag{1.109}$$

$$\boldsymbol{H}_t^{inc} = \Big(\frac{1}{2} I + \mathcal{D}_{2D}^* \Big) \boldsymbol{j}_{s,z} \,, \tag{1.110}$$

which are respectively the TM and TE EFIE, and the TM and TE MFIE, and where $\mathcal{S}_{2D}, D_{2D}, D_{2D}^*$ are the 2D equivalent of 1.98 - 1.100, as exemplified for $\mathcal{N}_{2D}$ in 1.107.

1.5 The boundary element method

Integral equations presented in the previous sections can be solved numerically by means of the boundary element method (BEM), a technique which applies the Method of Moments [7] to a boundary value problem. In this section, we will briefly walk through the Method of Moments in all its main steps: discretization, definition of the basis functions, test functions and to conclude linear system formulation. Than, in the next sections, we will see more in detail those steps, showing in details how this method is applied in electromagnetic problems in BEM setting.

We will take as example the electric field integral equation for PEC materials, in which magnetic surface currents are null because of the PEC properties of having null electric field inside:

$$\eta \, \mathcal{T}_k \, \boldsymbol{j}_s = -\hat{\boldsymbol{n}} \times \boldsymbol{E}^{inc}. \tag{1.111}$$

Note that this is just a case, but the very same procedure can be applied also to the other integral equation seen in the previous sections. $\mathcal{T}_k$ is a linear operator; the unknown current $\boldsymbol{j}_s$ and the RHS $\boldsymbol{b} \coloneqq (-\hat{\boldsymbol{n}} \times \boldsymbol{E}^{inc})$ are functions in the space $\{\Gamma \to \mathbb{C}^3\}$.

Discretization

To numerically tackle the boundary integral equation (BIE) presented in eq. (1.111), the first step involves discretizing the surface Γ. The mesh elements provide the basis for defining the domain of the basis functions, which are crucial for discretizing both the current and the right-hand side (RHS) of the equation.

Basis functions

The unknown current $\boldsymbol{j}_s$ is approximated as a linear combination of N_s basis functions, called source basis functions, $\boldsymbol{s}_n$:

$$\boldsymbol{j}_s(\boldsymbol{r}) \simeq \sum_{n=1}^{N_s} \mathrm{j}_n \boldsymbol{s}_n(\boldsymbol{r}). \tag{1.112}$$

These basis functions are vectorial ($\boldsymbol{s}_n : \Gamma \to \mathbb{R}^3$), while the coefficients j_n are complex scalars, so that the linear combination in 1.112 can be a valid approximation of $\boldsymbol{j}_s$. Substituting eq. (1.112) in eq. (1.111), by linearity

$$\eta \sum_{n=1}^{N_s} \mathrm{j}_n \mathcal{T}_k \, \boldsymbol{s}_n \simeq \boldsymbol{b}. \tag{1.113}$$

Test functions

The objective is to find the unknown coefficients j_n such as to minimize the error $\left(\boldsymbol{b} - \eta \sum_{n=1}^{N_s} \mathrm{j}_n \mathcal{T}_k \, \boldsymbol{s}_n\right)$, called residual. To this purpose, the residual is tested against a set of N_t basis functions, called test basis functions, $\boldsymbol{t}_m$, and the result of each of these operations is imposed to be null

$$\begin{aligned}
&\left\langle \boldsymbol{t}_m, \boldsymbol{b} - \eta \sum_{n=1}^{N_s} \mathrm{j}_n \mathcal{T}_k \, \boldsymbol{s}_n \right\rangle = 0 \\
\iff &\eta \sum_{n=1}^{N_s} \mathrm{j}_n \left\langle \boldsymbol{t}_m, \mathcal{T}_k \, \boldsymbol{s}_n \right\rangle = \left\langle \boldsymbol{t}_m, \boldsymbol{b} \right\rangle \\
\iff &\eta \sum_{n=1}^{N_s} \mathbf{T}_{mn} \, \mathrm{j}_n = \mathrm{b}_m \\
\iff &\eta \mathbf{T} \, \mathrm{j} = \mathrm{b}.
\end{aligned} \tag{1.114}$$

$\langle \boldsymbol{a}, \boldsymbol{b} \rangle$ denotes an inner product computation. For $\boldsymbol{a}$, $\boldsymbol{b} : \Gamma \to \mathbb{C}^3$,

$$\langle \boldsymbol{a}, \boldsymbol{b} \rangle = \iint_\Gamma \overline{\boldsymbol{a}(\boldsymbol{r})} \cdot \boldsymbol{b}(\boldsymbol{r}) dS \tag{1.115}$$

and for $\boldsymbol{a}$, $\boldsymbol{b} : \gamma \to \mathbb{C}^2$,

$$\langle \boldsymbol{a}, \boldsymbol{b} \rangle = \int_\gamma \overline{\boldsymbol{a}(\boldsymbol{r})} \cdot \boldsymbol{b}(\boldsymbol{r}) dl, \tag{1.116}$$

where the overline denotes complex conjugation.

Linear system formulation

Finally, a numerical solution of the integral equation 1.111 can be found by solving the linear system

$$\eta \mathbf{T}\,\mathrm{j} = \mathrm{b} \tag{1.117}$$

where the involved quantities read

$$\mathbf{T}_{mn} = \langle \boldsymbol{t}_m, \mathcal{T}_k\, \boldsymbol{s}_n \rangle \tag{1.118}$$

$$\mathrm{j}_n = \langle \boldsymbol{s}_n, \boldsymbol{j}_s \rangle \tag{1.119}$$

$$\mathrm{b}_m = \langle \boldsymbol{t}_m, \boldsymbol{b} \rangle\,. \tag{1.120}$$

1.5.1 The Gram Matrix

The Gram matrix is the Method of Moments identity operator,i.e., it maps quantities from basis functions to test ones. Given a set of source basis functions $\{\boldsymbol{s}_n\}_{n=1}^{N}$ and a set of test functions $\{\boldsymbol{t}_m\}_{m=1}^{M}$ defined on a discretized domain Γ, the Gram matrix $\mathbf{G}_{t,s} \in \mathbb{R}^{M\times N}$ is defined by its elements:

$$[\mathbf{G}_{t,s}]_{mn} = \langle \boldsymbol{t}_m, \boldsymbol{s}_n \rangle_{\Gamma}\,. \tag{1.121}$$

In particular, when different basis and test functions are employed, the resulting operator is often referred to as mix-Gram matrix. The Gram matrix thus encapsulates the geometric and functional relationships between these basis and test functions, offering insights into their orthogonality, linear independence, and stability of the numerical methods employed.

1.5.2 Mesh Elements

3D case

In the 3D setting, discretization is typically achieved using flat triangular elements to construct what is known as a mesh. An example is shown in Fig. 1.6. The fidelity with which this mesh represents Γ is largely governed by the average length of the edges, denoted as h. The selection of h is critical and must adhere to both the Nyquist-Shannon sampling theorem, ensuring $h < \lambda/2$ where λ is the wavelength, and the necessity to accurately reflect the geometric details of the surface. Depending on the application, one of the two constraints will be the critical one, and as we will see later, this largely determines the strategies that can be used to solve the problem in a computationally effective way.

2D case

On a bi-dimensional manifold, the most intuitive discretization is the one with piecewise linear elements, which can be seen as the 2D-equivalent of the triangular elements proposed for the 3D case. An example is shown in Fig. 1.7. Again, the average length of those elements h determines both the discretization (and consequently, the simulation) accuracy and the computational effort. h must be chosen accordingly to Nyquist-Shannon theorem, i.e., $h < \lambda/2$, and must be small enough to well represent the geometry details of the manifold to be discretized.

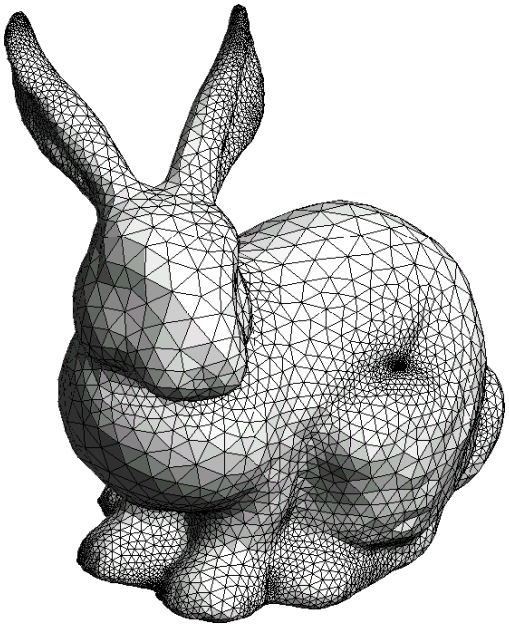

Figure 1.6: 3D triangular mesh for a bunny model

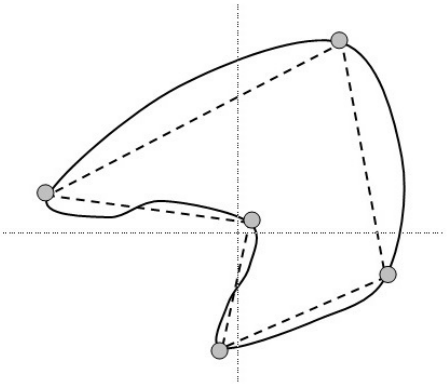

Figure 1.7: Piecewise linear mesh for a 2D manifold

1.5.3 Basis functions

A discretization of the closed surface Γ, equipped with an outward unit normal $\hat{\boldsymbol{n}}$ at each point, is achieved using a triangular mesh consisting of N_V vertices, N_E edges, and N_F flat triangular faces. The topology of Γ is quantified by its genus, N_H, representing the count of handles on the surface. Euler's relation for such geometries is captured by:

$$N_E = N_V + N_F + 2N_H - 2 \tag{1.122}$$

The discretization employs local basis functions, such as Rao-Wilton-Glisson (RWG), Buffa-Christiansen (BC), and others, each defined within specific mesh elements

(edges, vertices, or faces). Conversely, global loops, reflecting the geometry's handles, extend across the entire mesh. In this section, we will delve into the various basis functions employed in electromagnetic BEM, focusing first on the 3D setting and then to the 2D one.

Rao-Wilton-Glisson basis functions

Defined on mesh edges, Rao-Wilton-Glisson or Raviart-Thomas basis functions fig. 1.8, associate with any edge e_i bridged by vertices $\boldsymbol{v}_i^{\pm}$, as:

$$f_i(\boldsymbol{r}) = \begin{cases} \dfrac{\boldsymbol{r} - \boldsymbol{r}_i^+}{2A_i^+} & \boldsymbol{r} \in c_i^+ \\ \dfrac{\boldsymbol{r}_i^- - \boldsymbol{r}}{2A_i^-} & \boldsymbol{r} \in c_i^- \end{cases}, \tag{1.123}$$

where $A_i^{\pm}$ denotes the area of the triangle $c_i^{\pm}$, with $c_i^{\pm}$, $\boldsymbol{r}_i^{\pm}$ and $\boldsymbol{v}_i^{\pm}$ as in Fig. 1.9. This normalization ensures the flux through edge e_i is unity, though some conventions also incorporate edge length l_i for additional scaling as per [8]. A key feature of RWG functions is the continuity of their normal component across e_i, constant along the edge at:

$$|f_i(\boldsymbol{r} \in e_i) \cdot \hat{\boldsymbol{n}}_i| = \frac{1}{l_i}, \tag{1.124}$$

with $\hat{\boldsymbol{n}}_i$ being the edge's normal unit vector. However, their tangential components are discontinuous. This continuity implies RWG functions are divergence-conforming, with their divergence across mesh faces expressed as

$$\nabla \cdot f_i(\boldsymbol{r}) = \begin{cases} \dfrac{1}{A_i^+} & \boldsymbol{r} \in c_i^+ \\ -\dfrac{1}{A_i^-} & \boldsymbol{r} \in c_i^- \end{cases}, \tag{1.125}$$

where A_i^+ and A_i^- are the areas of faces c_i^+ and c_i^-, indicating piece-wise constant divergence. Yet, due to tangential discontinuity, RWG functions are not curl-conforming. A curl-conforming basis can be derived by rotating RWG functions through $\hat{\boldsymbol{n}}\times$ operation, although such functions are not divergence-conforming.

Buffa-Christiansen basis functions

Introduced by [9], BC basis functions are localized on edges within a barycentrically refined mesh. This refinement subdivides each face into six smaller triangles, positioning new vertices at midpoints of edges, original vertices, and median intersections. The BC function for edge e_i combines RWG functions of adjacent

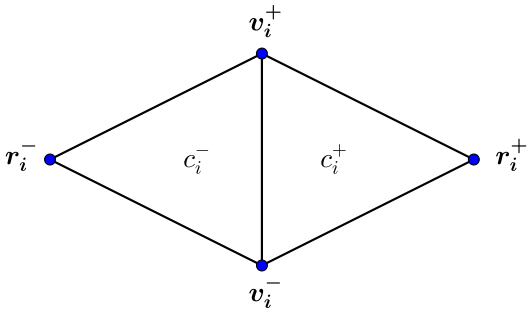

Figure 1.8: Notation used for the definition of RWG functions.

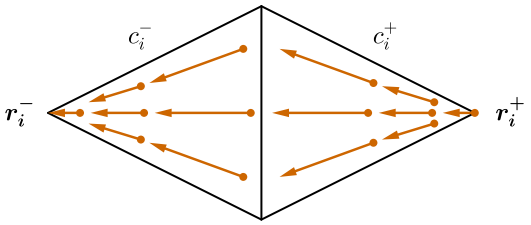

Figure 1.9: Rao-Wilton-Glisson basis function.

edges sharing a vertex with e_i. BC functions, symbolized as $\boldsymbol{g}$, are inherently divergence-conforming and quasi-curl-conforming, a property elucidated in [10]. This indicates a well-conditioned relationship (i.e., a well-conditioned Gram matrix) between BC functions and their rotated RWG counterparts. Rotated BC functions, $\hat{\boldsymbol{n}} \times \boldsymbol{g}$, exhibit both curl-conformity and quasi-divergence-conformity.

Loop basis functions

Pyramid basis functions are constructed locally around vertices, with the loop function for a vertex v_j described as

$$\lambda_j(\boldsymbol{r}) = \begin{cases} 1 & \boldsymbol{r} = \boldsymbol{v}_j, \\ 0 & \boldsymbol{r} = \boldsymbol{v}_i, i \neq j, \\ \text{linear} & \text{otherwise}, \end{cases} \tag{1.126}$$

achieving a value of one at v_j and zero at other vertices, often referred to as the pyramid function [11]. With reference to pyramid basis functions, each loop function is defined as $\Lambda_j(\boldsymbol{r}) = \nabla_s \times \hat{\boldsymbol{n}}\lambda_j(\boldsymbol{r})$, where ∇_s is the surface gradient operator defined as

$$\nabla_s = \nabla - \hat{n}\frac{\partial}{\partial n}\,. \tag{1.127}$$

Thus, the loop basis can be interpreted as the discretized surface curl operator [12]. The Loop to RWG matrix $\boldsymbol{\Lambda}$ (the matrix whose columns are the coefficients of the Loop functions when expressed as linear combinations of the RWG functions) can be expressed as

$$\boldsymbol{\Lambda}_{ij} = \begin{cases} +1 & v_j = v_i^+ \\ -1 & v_j = v_i^- \\ 0 & \text{otherwise} \end{cases}\,. \tag{1.128}$$

The loop basis functions are characterized by their solenoidal nature, as evident from their definition and the divergence property of RWG functions.

Star basis functions

Patch basis functions can be defined for a face c_j as

$$p_j(\boldsymbol{r}) = \begin{cases} \frac{1}{A_j} & \text{if } \boldsymbol{r} \in c_j, \\ 0 & \text{otherwise}, \end{cases} \tag{1.129}$$

where A_j is the area of face c_j. Note that these basis functions are localized to faces and piecewise constant. Star basis functions are defined on faces, and the Star to RWG matrix $\boldsymbol{\Sigma}$ (the matrix whose columns are the coefficients of the Star functions when expressed as linear combinations of the RWG functions) is defined as

$$\boldsymbol{\Sigma}_{ij} = \begin{cases} +1 & c_j = c_i^+ \\ -1 & c_j = c_i^- \\ 0 & \text{otherwise} \end{cases}. \tag{1.130}$$

or equivalently as $\boldsymbol{\Sigma}_{ij} = \langle p_i, \nabla_s \cdot f_j(\boldsymbol{r}) \rangle$, highlighting their behavior as discretized surface div operator [12]. Notably, substituting RWG functions in a star with BC functions yields a solenoidal function [11].

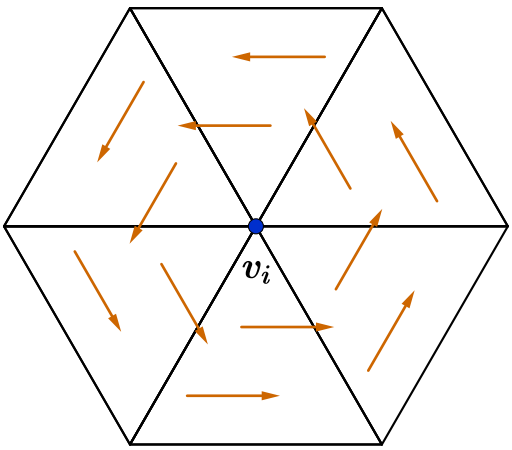

Figure 1.10: Loop basis function.

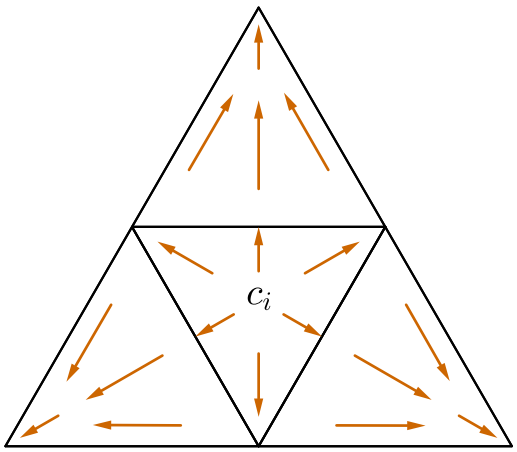

Figure 1.11: Star basis function.

Global Loops

Global loops, defined per handle, introduce two types, toroidal and poloidal, as depicted for a torus. Within the considered mesh, global loops are expressible as

sums of RWG functions:

$$\boldsymbol{h}_j(\boldsymbol{r}) = \sum_{i=1}^{N_e} \boldsymbol{H}_{ij} \boldsymbol{f}_i(\boldsymbol{r}), \tag{1.131}$$

with $\boldsymbol{H} \in \mathbb{R}^{N_E \times 2N_H}$ as the transformation matrix. To cope with the computational intensity of this formulation, an alternative involves calculating $\boldsymbol{H}$ as the null-space of integral operators, detailed in [13]. Global loops, thus defined, are solenoidal but exclusively so, differing from their harmonic, non-discretized counterparts due to the limitations of the RWG basis in representing the curl operator with regularity.

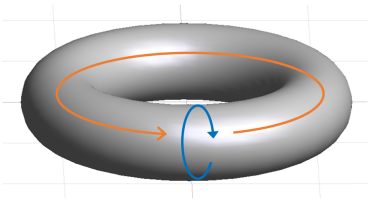

Figure 1.12: Global loops on a torus ($N_H = 1$): toroidal in orange, poloidal in blue.

Piecewise linear basis functions

In the bi-dimensional setting, piecewise linear basis functions are defined on the vertices. More in detail, they are defined as

$$\phi_i(x) = \begin{cases} \dfrac{x - x_{i-1}}{x_i - x_{i-1}} & x \in [xi - 1, x_i] \\ \dfrac{x_{i+1} - x}{x_{i+1} - x_i} & x \in [x_i, x_{i+1}] \end{cases}, \tag{1.132}$$

where x is the curvilinear abscissa along the curve being discretized. Note that this definition strongly recalls the RWG definition, with edges in place of faces and vertices in place of edges, due to the reduced dimensionality of the problem. These basis functions are also known as Hat functions, a visualization is in Fig. 1.13.

Dirac delta as basis functions

Another possible choice for basis function, valid both for 3D and 2D, is

$$\boldsymbol{f}_i(\boldsymbol{r}) = \delta(\boldsymbol{r_i})\, \boldsymbol{r_i} \in \Gamma. \tag{1.133}$$

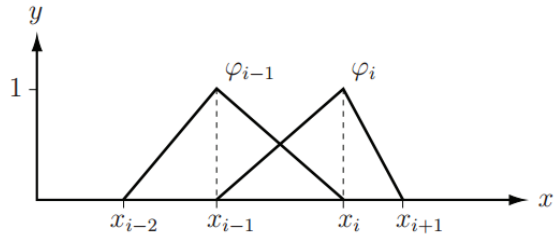

Figure 1.13: Piecewise linear basis functions example on a non-uniform discretized domain

It must be noted that this choice has really bad continuity properties, in fact it is discontinuous and has discontinuous derivatives of all kind, thus it cannot represent real quantities. However, it is very simple to convolve with, and as we will see exhibits some really nice computational features. It is also noteworthy that in the context of numerical integration schemes, "sampling" implicitly refer to convolution with Dirac delta.

1.5.4 Discretization of operators and physical quantities

Selecting appropriate source and testing basis functions is a crucial aspect of discretizing integral equations, heavily influenced by the regularity requirements of the operator in use.

Considering the Electric Field Integral Equation (EFIE) for Perfect Electric Conductors (PEC), the discretization process frequently employs Rao-Wilton-Glisson (RWG) basis functions $\boldsymbol{f}$ for sources and their rotated counterparts $\hat{\boldsymbol{n}} \times \boldsymbol{f}$ for testing. This approach leads to the evaluation of the right-hand side (RHS) against these rotated RWG functions, resulting in:

$$\mathbf{T}_{mn} = \langle \hat{\boldsymbol{n}} \times \boldsymbol{f}_m, \mathcal{T}_k \, \boldsymbol{f}_n \rangle \tag{1.134}$$

$$\mathrm{b}_m = \langle \hat{\boldsymbol{n}} \times \boldsymbol{f}_m, \boldsymbol{b} \rangle \,, \tag{1.135}$$

where the operation $\hat{\boldsymbol{n}}\times$ applied during testing aligns with and simplifies against similar operations defined within the expressions for $\mathcal{T}_k$ and $\boldsymbol{b}$. For the following, it is useful to also define the discretized vector and scalar potential operators

$$\mathbf{T}_{\boldsymbol{A},mn} = \langle \hat{\boldsymbol{n}} \times \boldsymbol{f}_m, \mathcal{T}_{\boldsymbol{A},k} \, \boldsymbol{f}_n \rangle \tag{1.136}$$

$$\mathbf{T}_{\phi,mn} = \langle \hat{\boldsymbol{n}} \times \boldsymbol{f}_m, \mathcal{T}_{\phi,k} \, \boldsymbol{f}_n \rangle \tag{1.137}$$

$$\tag{1.138}$$

Analogously, for the discretization of the PEC-EFIE using Buffa-Christiansen (BC)

$\boldsymbol{g}$ basis functions as sources and their rotated versions $\hat{\boldsymbol{n}} \times \boldsymbol{g}$ for testing, we find:

$$\mathbb{T}_{mn} = \langle \hat{\boldsymbol{n}} \times \boldsymbol{g}_m, \mathcal{T}_k \, \boldsymbol{g}_n \rangle \tag{1.139}$$

$$\mathbb{b}_m = \langle \hat{\boldsymbol{n}} \times \boldsymbol{g}_m, \boldsymbol{b} \rangle \, . \tag{1.140}$$

This systematic approach ensures that the testing procedure, involving the rotation through $\hat{\boldsymbol{n}}\times$, is effectively accounted for and integrated into the formulations for both $\mathcal{T}_k$ and the incident field $\boldsymbol{b}$ components. Also the identity operator can be discretized by means of some source and test basis functions leading to the Gram or mix-Gram matrix, as already explained in 1.5.1.

1.5.5 Simplification of the scalar potential calculation

Finally, it is worth mentioning a common trick exploited in the discretization of the $\mathcal{T}_{\phi,k}$ operator to eliminate the gradient present in its definition. The testing to be evaluated is

$$\begin{aligned} \mathbf{T}_{\phi,mn} &= \langle \hat{\boldsymbol{n}} \times \boldsymbol{f}_m, \mathcal{T}_{\phi,k} \, \boldsymbol{f}_n \rangle \\ &= \iint_{\Gamma_m} d\boldsymbol{r} \, (\hat{\boldsymbol{n}}(\boldsymbol{r}) \times \boldsymbol{f}_m(\boldsymbol{r})) \cdot \left(\hat{\boldsymbol{n}}(\boldsymbol{r}) \times \nabla \iint_{\Gamma_n} d\boldsymbol{r}' \, G_k(\boldsymbol{r}, \boldsymbol{r}') \nabla' \cdot \boldsymbol{f}(\boldsymbol{r}') \right), \end{aligned} \tag{1.141}$$

where Γ_m and Γ_n are the supports of the testing and source basis functions considered. After simplifying the $\hat{\boldsymbol{n}}\times$ operators and by defining the scalar quantity $\psi(\boldsymbol{r}) = \iint_{\Gamma_n} d\boldsymbol{r}' \, G_k(\boldsymbol{r}, \boldsymbol{r}') \nabla' \cdot \boldsymbol{f}(\boldsymbol{r}')$, the above testing reduces to

$$\mathbf{T}_{\phi,mn} = \iint_{\Gamma_m} d\boldsymbol{r} \, \boldsymbol{f}_m(\boldsymbol{r}) \cdot \nabla \psi(\boldsymbol{r}). \tag{1.142}$$

By applying the vector calculus identity $\nabla \cdot (\psi \boldsymbol{f}_m) = \psi \nabla \cdot \boldsymbol{f}_m + (\nabla \psi) \cdot \boldsymbol{f}_m$, we get

$$\mathbf{T}_{\psi,mn} = \iint_{\Gamma_m} d\boldsymbol{r} \, \nabla \cdot (\psi(\boldsymbol{r}) \boldsymbol{f}_m(\boldsymbol{r})) - \iint_{\Gamma_m} d\boldsymbol{r} \, \psi(\boldsymbol{r}) \nabla \cdot \boldsymbol{f}_m(\boldsymbol{r}). \tag{1.143}$$

By applying the divergence theorem and noticing that the normal component of an RWG function at the boundary of its domain is null, it follows that the first term in eq. (1.143) is null, since

$$\iint_{\Gamma_m} d\boldsymbol{r} \, \nabla \cdot (\psi(\boldsymbol{r}) \boldsymbol{f}_m(\boldsymbol{r})) = \oint_{\partial \Gamma_m} \psi(\boldsymbol{r}) \, (\boldsymbol{f}_m(\boldsymbol{r}) \cdot \hat{\boldsymbol{n}}(\boldsymbol{r})) \, d\boldsymbol{l} = 0. \tag{1.144}$$

Finally, the gradient in the definition of $\mathcal{T}_{\phi,k}$ has been removed, and a divergence operation has appeared to the testing function, so that the expression of $\mathbf{T}_{\phi,mn}$ reads

$$\mathbf{T}_{\phi,mn} = - \iint_{\Gamma_m} d\boldsymbol{r} \, \nabla \cdot \boldsymbol{f}_m(\boldsymbol{r}) \iint_{\Gamma_n} d\boldsymbol{r}' \, G_k(\boldsymbol{r}, \boldsymbol{r}') \nabla' \cdot \boldsymbol{f}(\boldsymbol{r}'), \tag{1.145}$$

This discretization operation becomes completely similar to that of the electric vector potential operator, apart from the fact that the divergence is applied to both source and test basis functions.

1.5.6 Changes of basis in the solution of linear systems

When solving linear systems using a change of basis, proper normalization must be applied to the quantities of interest. Given a discretized operator $[\mathbf{A}_{p,p}]_{mn} = \langle \boldsymbol{p}_m, \mathcal{A}\boldsymbol{p}_n \rangle$, a change of basis described by the mix-gram matrix $[\mathbf{G}_{q,p}]_{mn} = \langle \boldsymbol{q}_m, \boldsymbol{p}_n \rangle$ and the gram matrix $[\mathbf{G}_{p,p}]_{mn} = \langle \boldsymbol{p}_m, \boldsymbol{p}_n \rangle$, we want to compute $[\mathbf{A}_{q,q}]_{mn} = \langle \boldsymbol{q}_m, \mathcal{A}\boldsymbol{q}_n \rangle$.

At first, we need to normalize $\mathbf{A}_{p,p}$ with respect to the inner product in the $\boldsymbol{p}$-basis as

$$\mathbf{A}_{p,p,\text{norm}} = G_{p,p}^{-0.5} \mathbf{A}_{p,p} G_{p,p}^{-0.5} \,. \tag{1.146}$$

Now, we can correctly apply the change of basis

$$\mathbf{A}_{q,q} = \mathbf{G}_{q,p}^{H} \mathbf{A}_{p,p,\text{norm}} \mathbf{G}_{q,p} \,. \tag{1.147}$$

In the context of a linear system in the form $\mathbf{A}_{p,p}\mathbf{b}_p = \mathbf{x}_p$, the normalization and change of basis must also be applied to $\mathbf{b}$ and $\mathbf{x}$ as

$$\mathbf{b}_q = \mathbf{G}_{q,p}^{H} G_{p,p}^{-0.5} \mathbf{b}_p \tag{1.148}$$

$$\mathbf{x}_q = \mathbf{G}_{q,p}^{H} G_{p,p}^{-0.5} \mathbf{x}_p \tag{1.149}$$

leading to the full system solution in the form

$$\mathbf{b}_p = \mathbf{G}_{p,p}^{-0.5} \mathbf{G}_{p,q} \left(\mathbf{G}_{p,q}^{H} \mathbf{G}_{p,p}^{-0.5} \mathbf{A}_{p,p} \mathbf{G}_{p,p}^{-0.5} \mathbf{G}_{p,q} \right)^{-1} \mathbf{G}_{p,q}^{H} \mathbf{G}_{p,p}^{-0.5} \mathbf{x}_p. \tag{1.150}$$

Despite the appearing complexity, consider that for local basis functions $\mathbf{G}_{p,p}$ are sparse, and their multiplication and inversion is easily achievable in linear complexity. Furthermore, the inversion of the operator upon the change of basis may lead to significant improvement in the computation time, as exemplified in 3.2.1.

1.6 Introduction to Numerical Integration

A pivotal step towards fully realizing the Boundary Element Method involves the numerical implementation of the inner products outlined in equations 1.115 - 1.116. Beyond these points, all formulations become discrete, making them amenable to computational processing. This challenge is at the heart of a broad domain within computational science, known as *Numerical Integration*. Our objective here is to

provide a primer on this subject, emphasizing how various strategies for addressing this challenge significantly influence the final solution.

Numerical integration involves approximating the integral of a function using a finite sum. Generally, this process includes selecting a suitable set of points within the integration domain and assigning a weight to each point. The choice of points and their associated weights plays a crucial role in determining the accuracy and efficiency of the numerical integration. Apart special cases related to particular function classes, the integration accuracy always depends on the discretization density (i.e., number of sampling points per unit length, surface or volume) and on the smoothness of the function to be integrated and of its derivatives. Since the computational cost scales with the discretization density, a trade-off between accuracy and computational intensity must be found depending on the application's need. Rules which guarantees certain levels of accuracy of the integration exists for the domains and functions of interest.

Gauss-Legendre quadrature

The Gauss-Legendre quadrature falls under the category of Gaussian quadrature, a family of schemes for polynomials and smooth functions integration over a fixed interval, typically $[-1, 1]$. The essence of the Gauss-Legendre integration rule lies in its selection of both integration points (the abscissas) and their corresponding weights in such a way that they ensures that the method achieves the highest possible degree of accuracy for polynomials w.r.t the number n of integration points. Specifically, the abscissas are chosen to be the roots of Legendre polynomials, and the weights are determined to maximize the accuracy of the integral's approximation over the chosen interval. For an inner product $\langle \boldsymbol{f}_i, \boldsymbol{\phi} \rangle$, where $\boldsymbol{f}_i$ is a piecewise linear basis function as defined in 1.132, and $\boldsymbol{\phi} : \gamma \to \mathbb{C}^2$ represents a continuous and differentiable function on y, the Gauss-Legendre integration scheme can be applied to numerically approximate the integral. The process involves mapping the integration domain to the standard interval of the Gauss-Legendre quadrature and then applying the quadrature rule to compute the approximation.

Error bound

Gauss-Legendre quadrature with n points is exact for polynomials of degree less than or equal to $2n - 1$. Given a function $f(x)$ that is $2n$-times continuously differentiable on the interval $[-1, 1]$, the error E_n of the Gauss-Legendre quadrature can be expressed as:

$$E_n = \left| \int_{-1}^{1} f(x)\, dx - \sum_{i=1}^{n} w_i f(x_i) \right| = \frac{f^{(2n)}(\xi)}{(2n)!} \cdot \frac{2^{2n+1}[(n!)^4]}{(2n+1)[(2n)!]^3}, \tag{1.151}$$

for some $\xi \in (-1, 1)$, where w_i are the quadrature weights, x_i are the quadrature points (roots of the n-th Legendre polynomial), and $f^{(2n)}(\xi)$ is the $2n$-th derivative of $f(x)$ evaluated at some point ξ within the interval.

Assuming $f^{(2n)}(\epsilon) = \text{const}$ over the interval, the error bound simplifies to:

$$E_n = \mathcal{O}\left(\frac{1}{(2n)!}\right). \tag{1.152}$$

Considering the rapid growth of the factorial function compared to the growth rate of the derivatives of the functions of interest, typically at most polynomial (like in the case of the derivation of $e^{\alpha x}, \alpha > 1$, which derivatives grows like $\mathcal{O}(\alpha^n)$ the error term decreases very quickly as n increases. This make the Gauss-Legendre integration scheme highly effective in practical cases.

surface integrals

To extend the Gauss-Legendre quadrature rule to surface integrals, the method involves applying a tensor product of the one-dimensional (1D) Gauss-Legendre quadrature rule across each dimension independently. For a function $f(x, y)$ defined over a rectangular domain $D = [a, b] \times [c, d]$ in the xy-plane, the 2D integral can be approximated by:

$$\iint_D f(x, y)\, dx\, dy \approx \sum_{i=1}^{n} \sum_{j=1}^{n} w_i w_j f(x_i, y_j), \tag{1.153}$$

where x_i and y_j are the Gauss-Legendre quadrature points in the x and y directions, respectively, and w_i and w_j are the corresponding weights. This approach effectively decomposes the 2D integral into a series of weighted sums of the function evaluated at the quadrature points. For non-rectangular domains additional transformations or mappings are required to convert the integration domain to a standard form where the Gauss-Legendre quadrature can be directly applied. This domain conversion is often source of complexities, under both accuracy, complexity and stability points of view. Specific integration methods exists for different domains, like [put some citations here].

1.6.1 Singularity integration

In the discretized functional space framework, the most relevant method of moments matrices for solving prevalent integral formulations are delineated as follows:

$$[\mathbf{T}_A]_{mn} = \iint_{\boldsymbol{r}\in\Gamma} \boldsymbol{f}_m(\boldsymbol{r}) \cdot \left(\iint_{\boldsymbol{r}'\in\Gamma} G(\boldsymbol{r}-\boldsymbol{r}')\boldsymbol{f}_n(\boldsymbol{r}')dS' \right) dS, \tag{1.154}$$

$$[\mathbf{T}_\phi]_{mn} = -\iint_{\boldsymbol{r}\in\Gamma} \nabla\cdot\boldsymbol{f}_m(\boldsymbol{r}) \left(\iint_{\boldsymbol{r}'\in\Gamma} G(\boldsymbol{r}-\boldsymbol{r}')\nabla'\cdot\boldsymbol{f}_n(\boldsymbol{r}')dS' \right) dS, \tag{1.155}$$

$$[\mathbf{K}]_{mn} = \iint_{\boldsymbol{r}\in\Gamma} \boldsymbol{f}_m(\boldsymbol{r}) \cdot \left(\iint_{\boldsymbol{r}'\in\Gamma} \nabla G(\boldsymbol{r}-\boldsymbol{r}')\times\boldsymbol{f}_n(\boldsymbol{r}')dS' \right) dS. \tag{1.156}$$

For the matrix entries where the supports of $\boldsymbol{f}_m$ and $\boldsymbol{f}_n$ are sufficiently distant, these integrals can be numerically approximated by employing two-dimensional Gaussian quadrature rules on triangles, applied twice with orders N and N', respectively:

$$[\mathbf{T}_A]_{mn} \approx \sum_{i=1}^{N} \boldsymbol{f}_m(\boldsymbol{r}_i) \cdot \left(\sum_{j=1}^{N'} G(\boldsymbol{r}_i-\boldsymbol{r}'_j)\boldsymbol{f}_n(\boldsymbol{r}'_j)w'_j \right) w_i, \tag{1.157}$$

$$[\mathbf{T}_\phi]_{mn} \approx -\sum_{i=1}^{N} \nabla\cdot\boldsymbol{f}_m(\boldsymbol{r}_i) \left(\sum_{j=1}^{N'} G(\boldsymbol{r}_i-\boldsymbol{r}'_j)\nabla'\cdot\boldsymbol{f}_n(\boldsymbol{r}'_j)w'_j \right) w_i, \tag{1.158}$$

$$[\mathbf{K}]_{mn} \approx \sum_{i=1}^{N} \boldsymbol{f}_m(\boldsymbol{r}_i) \cdot \left(\sum_{j=1}^{N'} \nabla G(\boldsymbol{r}_i-\boldsymbol{r}'_j)\times\boldsymbol{f}_n(\boldsymbol{r}'_j)w'_j \right) w_i, \tag{1.159}$$

where $\boldsymbol{r}_i$ and $\boldsymbol{r}'_j$ represent the sampling points on the supports of $\boldsymbol{f}_m$ and $\boldsymbol{f}_n$, with w_i and w'_j being the Gaussian weights at these points. While the Gauss-Legendre quadrature rule is typically employed and provides satisfactory outcomes for non-polynomial kernels, it yields imprecise or erroneous results when applied to integrands exhibiting singular behavior. This problematic scenario arises when the supports of $\boldsymbol{f}_m$ and $\boldsymbol{f}_n$ coincide or are proximate, leading to a situation where $\boldsymbol{r}_i \approx \boldsymbol{r}'_j$, rendering the Green's function and its gradient singular. Under these circumstances, specialized techniques are imperative for accurate integration.

Singularity Subtraction

A prominent method to manage singular kernels, the singularity subtraction technique, was introduced in seminal works [14, 15]. This approach entails reformulating the integrand with singular behavior by decomposing it into singular and non-singular components. This is practically achieved by subtracting the singular part from, and then adding it back to, the integrand. The differential, termed the regular part, devoid of singularities, is amenable to numerical integration via standard

quadrature rules. Conversely, the singular component can be assessed analytically. An illustrative case is the Green's function $G(\boldsymbol{r}-\boldsymbol{r'})$, which can be decomposed as

$$G(\boldsymbol{r}-\boldsymbol{r'}) = \frac{e^{-jk|\boldsymbol{r}-\boldsymbol{r'}|}-1}{4\pi|\boldsymbol{r}-\boldsymbol{r'}|} + \frac{1}{4\pi|\boldsymbol{r}-\boldsymbol{r'}|}, \tag{1.160}$$

with the initial term representing the regular part and the latter the singular portion.

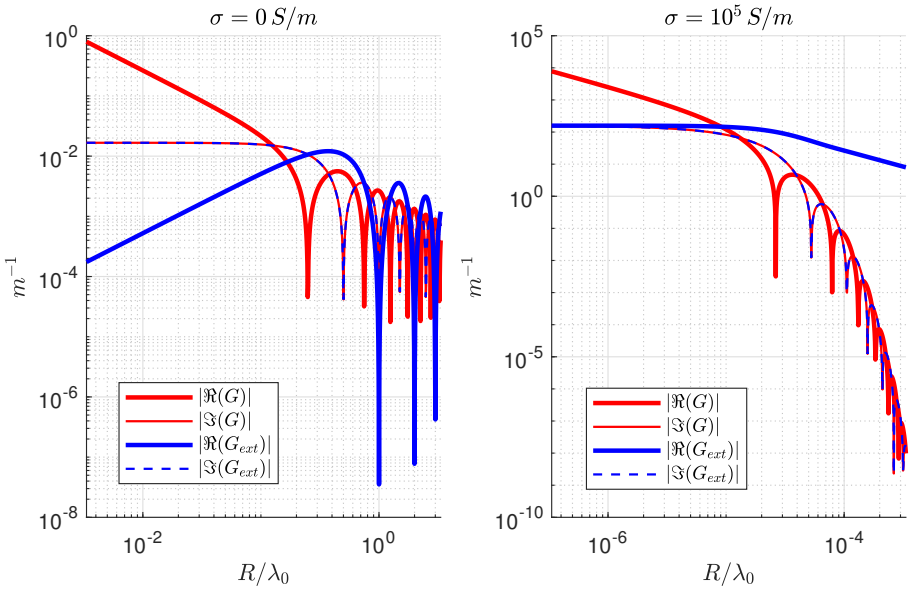

Figure 1.14: Comparative analysis of the Green's function and its regular component in both lossless and lossy media environments.

Figure 1.14 showcases a comparison between the characteristics of the Green's function and its regular segment in scenarios involving lossless and lossy media. The asymptotic behaviors of the real and imaginary sections as $R = |\boldsymbol{r}-\boldsymbol{r'}| \to 0$ align with the Taylor expansion given by

$$G(R) = \frac{1}{4\pi}\left[\frac{1}{R} - jk - k^2R + \mathcal{O}(R^2)\right], \tag{1.161}$$

highlighting that, for lossless conditions, $\Re(G) = \mathcal{O}(R^{-1})$, $\Im(G) = \mathcal{O}(1)$. The extraction of the singular segment influences solely the real component of the Green's function, leading to a transformation where $\Re(G_{ext}) = \mathcal{O}(R)$. Conversely, in lossy environments due to the complex nature of the wave number, the extracted Green's function's real part scales as $\Re(G_{ext}) = \mathcal{O}(1)$, with the imaginary section's behavior remaining unaffected by the subtraction process.

Singularity cancellation

The technique of singularity subtraction, while effective, necessitates the enumeration and programming of various specific scenarios for each potential kernel to analytically resolve their singular components. To address these complexities, numerous singularity cancellation methods have been devised over the years, with some of the most notable ones highlighted in [16–19]. These approaches tend to achieve a higher accuracy level compared to the traditional singularity subtraction methodology. The essence of these schemes lies in implementing a variable transformation for the integrand that introduces a Jacobian within the integral. The ideal transformation is one where the Jacobian precisely negates the kernel's singularity while transforming the original triangular integration domain into a rectangular one.

Particularly, [20] and [21] propose integration strategies centered around singularity cancellation, specifically tailored to mitigate the challenges in integrating the overdamped Green's function. A further significant advantage of these methods is their ability to simplify the integration from two dimensions to merely one dimension.

Green function filtering

As we will see in Chapter 4, the method that we propose in this work implicitly address also the singularity integration problem in an alternative way. The Green function filtering modifies the Green function in such a way that its singular part is inherently smoothed, allowing, among the other things, for easier integration.

Chapter 2

The graph Laplacian approach to filtering

The purpose of this chapter is twofold. On the one hand, we introduce here the main computational complexity and stability issues posed by the electromagnetic operators. On the other hand, we deeply analyze the role that the Laplacian operator plays, and how some manipulation based on it can lead to interesting solutions and strategies. More in detail, this chapter is structured as follow. We will start by introducing direct and inverse solvers, their complexity issues and the most known algorithms to tackle them. Then, we will discuss preconditioning, and in particular Quasi-Helmholtz decomposition as preconditioning strategy for the EFIE. An introduction to matrix spectral filtering follows, and to conclude Laplacian multiplicative filters are proposed as an effective way to perform spectral manipulation of electromagnetic integral equation operators.

2.1 Computational Complexity

An essential aspect when numerically solving a problem is the computational complexity of the employed algorithm. This encompasses the time required to reach a solution, and memory needed for data storage. Ideally, we'd like to develop numerical scheme whose complexity grows linearly or quasi-linearly with the number of unknowns, indicating scalability. The boundary integral equations discussed earlier, solved via the Boundary Element Method (BEM) with the formulation proposed in Chap. 1, do not exhibit this property. Let's take as example the PEC-EFIE equation (1.117), solved numerically over a mesh with N_e edges. The solution process encompasses three primary steps:

1. The computation of the matrix $\mathbf{T}$, explicitly calculated element by element,

which has a time complexity $\mathcal{O}(N_e^2)$.

2. The computation of the vector b, with a time complexity $\mathcal{O}(N_e)$.

3. The resolution of the linear system as shown in (1.117), explicitly solving for the current vector $\eta\,\mathrm{j} = \mathbf{T}^{-1}\mathrm{b}$, which complexity is dominated by matrix inversion, time complexity $\mathcal{O}(N_e^3)$.

Consequently, the overall complexity is $\mathcal{O}(N_e^3)$, leading to prohibitively long solution times as the number of unknowns increases. This issue extends to the matrix storage complexity, which is $\mathcal{O}(N_e^2)$, further complicating scalability.

2.1.1 Families of solvers

In this section, a primer is given on the principal approaches to numerical solution of linear systems.

Inverse solvers

Inverse solvers looks for single solutions of the linear system. The linear system is solved iteratively, aiming for a solution within the Krylov subspace, $\mathrm{span}\{\mathrm{b}, \mathbf{T}\mathrm{b}, \mathbf{T}^2\mathrm{b}, ..., \mathbf{T}^k\mathrm{b}\}$:

$$\eta\,\mathrm{j} = \mathbf{T}^{-1}\mathrm{b} \approx \sum_{i=1}^{k} \alpha_i \mathbf{T}^i \mathrm{b}. \tag{2.1}$$

Here, the time complexity depends on the product of the number of iterations k needed for the desired accuracy and the cost of matrix-vector multiplication, which naively requires $\mathcal{O}(N_e^2)$ operations. Efforts should thus focus on both reducing the number of iterations to a constant and minimizing the cost of computing the matrix and matrix-vector products to linear time. We will tackle the matrix-vector product problem and the iteration bound problem separately in the following.

Direct solvers

Direct solvers, on the other hand, tackle the problem in a more classical manner, inverting the system matrix. This operation is naively of complexity $\mathcal{O}(N_e^3)$, but leveraging matrix property this complexity could be reduced. The most notable property enabling fast inversion is the rank of the matrix: the inversion complexity for a $N \times N$ matrix with rank $r < N$ can be reduced to $\mathcal{O}(Nr^2)$ [22]. We will address in the following the problem of manipulating the matrix rank. Notice that, once the matrix has been inverted, computing solutions of the same problem for multiple stimuli reduces to a M-V product. This make those methods of great

interest, since in real scenarios this is often the case (e.g., given an antenna, we may want to compute its response to different impinging fields with varying frequencies and amplitudes).

2.1.2 Fast matrix vector product

Fast M-V product can be achieved by means of many techniques available in literature, such as the Adaptive Cross Approximation (ACA) [23, 24], and the Fast Multiple Method (FMM) [25], also available in multi-level versions [26–28]. These two approaches lead to M-V multiplication in time and memory growing as $\mathcal{O}(Nlog(N))$ for size N problems.

Adaptive Cross Approximation and Single-Skeleton Form Factorization

The Adaptive Cross Approximation (ACA) algorithm is a pivotal tool for efficiently dealing with matrices arising from boundary element methods and kernel-based methods with a numerically finite rank. The fundamental advantage of ACA is its ability to construct a low-rank approximation of a matrix $M \in \mathbb{R}^{N\times N}$ without needing to compute the full matrix. This allows for matrix storage and M-V multiplication in $\mathcal{O}(rN)$ complexity.

Given a matrix $\mathbf{M}$, assumed to have a numerically finite rank, ACA seeks an approximation M_{approx} that satisfies $||\mathbf{M} - \mathbf{M}_{\text{approx}}|| < \varepsilon$, where ε is a predefined accuracy threshold. The approximation is sought in the form of a product of two matrices,

$$\mathbf{M}_{\text{approx}} = \mathbf{U}\mathbf{V}^H, \quad \mathbf{U}, \mathbf{V} \in \mathbb{R}^{N\times r}, \tag{2.2}$$

where r is the rank of the approximation. The matrices $\mathbf{U}$ and $\mathbf{V}$ are constructed incrementally, capturing the essential structure of $\mathbf{M}$ with significantly fewer elements, leading to an approximation that can be stored and manipulated with $\mathcal{O}(rN)$ complexity, where $r \ll N$.

The ACA algorithm operates by selectively sampling rows and columns of M, progressively building up an outer product form until the desired precision is achieved. A notable enhancement of ACA is the incorporation of a pivoting procedure to improve numerical stability [29, 30]. It's important to note that the ACA resulting rank r may be higher than the optimal numerical rank obtained through Singular Value Decomposition (SVD) for the same accuracy level. However, SVD has cubic complexity which makes it unpractical in the fast solvers field.

The matrix-vector (M-V) between the matrix $\mathbf{M}$ approximated by $\mathbf{M}_{\text{approx}} = \mathbf{U}\mathbf{V}^H$ and the vector v can be efficiently computed as $\mathbf{M}\mathbf{v} = \mathbf{U}\mathbf{V}^H\mathbf{v}$, delivering a time complexity of $O(rN)$.

Another good property of ACA is its kernel-free nature, that implies its applicability does not depend on the specific properties of the kernel generating the

matrix but only on the rank properties of the matrix itself.

Fast Multipole Method

The Fast Multipole Method (FMM) represents a significant advancement in the computational treatment of N-body problems, where the objective is to efficiently evaluate the interactions among N particles. Traditional methods require $O(N^2)$ operations to compute all pairwise interactions, making large-scale simulations computationally intensive. FMM, however, reduces this complexity to $O(N \log N)$, enabling rapid computations even for systems with a vast number of elements. Practically, this method allows to compute fast M-V products for the matrices arising in our domain, even when full rank.

Originating from efforts to address computational challenges in gravitational and electrostatic simulations, FMM is based on a hierarchical decomposition of space and the use of multipole expansions to approximate the cumulative effect of distant particles on a given target. This approach also allows for precise control over approximation errors.

More in details, after decomposing the geometry in regions, the algorithm determines for each region near neighbors and far-interacting regions. For the first, the full matrix is computed and employed, but the number of neighbors for each region is constant: this means that the overall complexity of this computations scales as $\mathcal{O}(NM^2)$, where M is the size of each region. For the latter, the effect of all the sources in a region is summed up and streamlined to the destination region by (i) converting the spherical wave kernel in plain wave basis, (ii) translating the plane wave basis from source to destination and (iii) reconstructing the spherical wave kernel locally. This can be done in complexity (with some effort), thus limiting the overall complexity to $\mathcal{O}(N^{1.5})$ for the single-level algorithm (with an optimal choice of M), and to $\mathcal{O}(Nlog(N))$ for the multi-level one.

2.1.3 Inverse solver iteration bound

Notice that equation 2.1 is a (approximate) diagonalization of $\mathbf{T}^{-1}$, using the Krylov space as vector basis. This, leveraging the spectral theorem, leads to the relationship among the eigenvectors $\{\lambda_n\}$ of $\mathbf{T}$ and the iterative solver coefficients α_i

$$\frac{1}{\lambda_n} \simeq \sum_{i=1}^{k} \alpha_i \lambda_n^i. \tag{2.3}$$

By looking at 2.3, and recalling the strict relationship among singular values and eigenvalues, it is clear that the lower the variation range of the singular values of $\mathbf{T}$ (i.e., the lower the condition number), the fewer terms in the summation 2.3 are required to approximate accurately the values $\frac{1}{\lambda_n}$. Note that the condition number

is an effective indicator of rapid convergence of an inverse solver only under certain conditions, dictated by the spectral properties of the matrix $\mathbf{T}$. In particular, if $\mathbf{T}$ is Hermitian and positive definite, the CG method ensure an upper bound on the error $e^{(i)} = \mathrm{j}^{(i)} - \mathrm{j}$ given by [31]

$$\|e_i\|_{\mathbf{T}} \leq 2 \left(\frac{\sqrt{\text{cond } \mathbf{T}} - 1}{\sqrt{\text{cond } \mathbf{T}} + 1} \right)^i \|e_0\|_{\mathbf{T}} \tag{2.4}$$

which leads to an iteration bound, given a target error threshold ϵ,

$$i \leq \left[\frac{1}{2} \sqrt{\text{cond } \mathbf{T}} \ln \left(\frac{2}{\epsilon} \right) \right]. \tag{2.5}$$

However, in most practical cases, the involved matrices are not Hermitian and positive definite, making CG unpractical [32]. Other popular Krylov methods, such as GMRES or CGS, do not have such strict error bounds depending on the condition number alone. Other properties, such as the clustering of singular values on a semi-axis of the complex plane, are needed for rapid convergence [33].

In conclusion, in order to keep the number of iterations k constant and low, it is necessary to assure condition number of matrix $\mathbf{T}$ constant and as low as possible, or to enforce other spectral properties on the linear system matrix of interest. This is the final aim of matrix preconditioning.

It is worth noticing that, if on the one side spectral filtering enables to apply low-rank fast algorithms to the matrices, on the other side it introduces a large null-space that makes the condition number explode, thus special care must be taken when solving such systems. How to efficiently solve this issue is an open research field, with the Moore-Penrose pseudo-inverse serving as a track but not yet being a defnitive solution.

Introduction to preconditioning

In the context of solving linear systems, the concept of a matrix's condition number is pivotal. This parameter does more than just dictate the iteration count necessary for an iterative solver to find a solution; it also sets the limits on the solution's precision. A particularly high condition number might even prevent the solver from converging. A matrix is termed 'well-conditioned' when its condition number is modest and does not depend on the parameters of the problem, such as frequency, the total unknowns, or material properties. If not, it is regarded as 'ill-conditioned'.

The process of matrix preconditioning seeks to identify preconditioning matrices to the left and/or right, denoted by $\mathbf{L}$ and $\mathbf{R}$, with the aim of reducing the condition number of the product compared to that of the initial matrix. When employing both left and right preconditioners, the system of equations $\mathbf{A}x = b$ is transformed into:

$$\mathbf{LAR}y = \mathbf{L}b,$$

where the solution to the original system, x, is recovered by $x = \mathbf{R}y$. The choice of $\mathbf{L}$ and $\mathbf{R}$ is of paramount relevance. Those matrices must have very peculiar properties: they should support fast multiplication and compressed storage and they should effectively precondition the operator of interest.

2.2 Low frequency breakdown and Quasi-Helmholtz preconditioning

In this section, a glimpse into one of the most notable sources of ill-conditioning of the EFIE is presented, together with proposed solutions in literature. The purpose of this section is twofold: on the one hand, it is intended to help fixing ideas with a concrete example of ill-conditioning and curing by means of preconditioning; on the other hand, here we put the foundations needed to later introduce the graph Laplacian filters.

The genesis of the EFIE's low-frequency breakdown can be elucidated through its formulation in eq. (1.91): as $k \to 0$, the equation delineates a disparity in the behavior of its components—where the vector potential term scales as $\mathcal{O}(k)$, conversely, the scalar potential term scales as $\mathcal{O}(1/k)$. Alternatively, it can be seen as the mathematical incarnation of the quasi-static regime introduced in 1.3. This dichotomy results in the attenuation of the vector potential's contribution and an unbounded increase in the scalar potential's influence as the frequency decreases, leading to $\mathcal{T}_k \approx \frac{1}{jk}\mathcal{T}_{\phi,k}$ and signifying a decoupling of electric and magnetic fields approaching static conditions. The manifestation of this issue becomes apparent when addressing the linear system reformulated in eq. (1.117):

$$\left[-\eta(jk)^2\,\mathbf{T}_A + \eta\mathbf{T}_\phi\right]\,\mathrm{j} = jk\mathrm{b}, \tag{2.6}$$

highlighting that solenoidal current distributions approximate the solution, thereby underscoring the problem's ill-posedness.

A meticulous analytical scrutiny of the $\mathcal{T}$ operator's spectrum in the asymptotic regime reveals that its condition number grows as $\mathcal{O}(1/k^2)$ [11, 34]. In scenarios of sufficiently low frequencies, this escalates to a near (numerically) singular matrix condition, obfuscating the convergence of iterative methods designed for solving the linear system. To circumvent this predicament, a strategy involving the segregation of solenoidal and non-solenoidal current contributions is proposed. This entails a re-scaling of the corresponding system blocks independently, aiming to forestall information loss and thereby reformulating the problem as well-conditioned.

Quasi-Helmholtz preconditioning has emerged as a pivotal approach to address this problem. The inception of this solution strategy traces back to the seminal work by Wilton et al. [35], accruing significant relevance in contemporary research due

to the surge in demand for efficient and reliable low-frequency full-wave simulation tools, propelled by the miniaturization trend in electronic device manufacturing.

The section is structured as follows: first, we will introduce the Helmholtz decomposition theorem alongside with the Loop-Star decomposition, which is its most intuitive incarnation. Then, we will see how this decomposition comes together with some criticalities, and how Quasi-Helmholtz projectors can solve this problem.

2.2.1 Helmholtz Decomposition Theorem

The Helmholtz Decomposition Theorem posits that a vector field $\boldsymbol{U}$, provided it is sufficiently smooth and exhibits rapid decay, can be delineated as the sum of an irrotational component and a solenoidal component. Leveraging the fundamental identities of vector calculus, specifically for any smoothly varying scalar field ψ and vector field $\boldsymbol{V}$ where $\nabla \times (\nabla\psi) = 0$ and $\nabla \cdot (\nabla \times \boldsymbol{V}) = 0$, the decomposition is articulated as:

$$\boldsymbol{U} = \nabla\psi + \nabla \times \boldsymbol{V}, \tag{2.7}$$

with the first term symbolizing the irrotational portion and the latter term signifying the solenoidal portion of the field. In scenarios where $\boldsymbol{U}$ is defined over a two-dimensional manifold Γ, the decomposition adopts the guise of surface operators, expressed as:

$$\boldsymbol{U} = \nabla_s\psi + \hat{\boldsymbol{n}} \times \nabla_s\xi. \tag{2.8}$$

where ∇_s is defined and widely discussed in Sec. 2.4.1 Moreover, the rotation of 2.8 maintains the essence of a Helmholtz decomposition:

$$\hat{\boldsymbol{n}} \times \boldsymbol{U} = \hat{\boldsymbol{n}} \times \nabla_s\psi - \nabla_s\xi, \tag{2.9}$$

thereby interchanging the roles of the solenoidal and irrotational components.

In practical applications where $\boldsymbol{U}$ is discretized, that is, expressed as a linear amalgam of basis functions as outlined in eq. (1.112), achieving a full Helmholtz decomposition directly is not always viable; instead, a quasi-Helmholtz decomposition is employed. This approach bifurcates the field into solenoidal, $\boldsymbol{U}^s$, and non-solenoidal, $\boldsymbol{U}^{ns}$, constituents:

$$\boldsymbol{U} = \boldsymbol{U}^s + \boldsymbol{U}^{ns}. \tag{2.10}$$

Subsequent sections delve into two distinct methodologies to accomplish this decomposition, namely Loop-Star decomposition and Quasi-Helmholtz projectors.

2.2.2 Loop-Star Decomposition

Loop, star, and global loops, delineated respectively on vertices, cells, and handles, have been introduced previously. It has been established that for a closed surface

Γ, these functions comprehensively span the RWG space. Euler's equation 1.122 elucidates that the columns of $\boldsymbol{\Lambda}$ and $\boldsymbol{\Sigma}$ matrices are not linearly independent, necessitating the removal of one column from each to achieve linear independence. Henceforth, it is assumed that these adjustments have been made, rendering $\boldsymbol{\Lambda} \in \mathbb{R}^{N_E \times (N_V - 1)}$ and $\boldsymbol{\Sigma} \in \mathbb{R}^{N_E \times (N_C - 1)}$. The decomposition matrix $\boldsymbol{A}$ is thus defined as:

$$\boldsymbol{A} = (\boldsymbol{\Lambda} \quad \boldsymbol{H} \quad \boldsymbol{\Sigma}). \tag{2.11}$$

Revisiting the discretized (PEC)-EFIE 1.117, employing $\boldsymbol{A}^T$ and $\boldsymbol{A}$ as left and right preconditioning matrices, respectively, transforms the linear system to:

$$\begin{cases} \eta \mathbf{A}^T \mathbf{T} \mathbf{A}\, \mathbf{y} = \mathbf{A}^T \mathbf{b} \\ \mathbf{j} = \mathbf{A}\mathbf{y} \end{cases}. \tag{2.12}$$

This can be envisioned as a change of basis from RWG to Loop-Stars-Global loops performed in the forward direction before solving the system, and backward after the system solution.

Expanding the block multiplication $\boldsymbol{A}^T \mathbf{T} \boldsymbol{A}$ yields:

$$\boldsymbol{A}^T \mathbf{T} \boldsymbol{A} = \begin{pmatrix} \boldsymbol{\Lambda}^T \mathbf{T} \boldsymbol{\Lambda} & \boldsymbol{\Lambda}^T \mathbf{T} \boldsymbol{H} & \boldsymbol{\Lambda}^T \mathbf{T} \boldsymbol{\Sigma} \\ \boldsymbol{H}^T \mathbf{T} \boldsymbol{\Lambda} & \boldsymbol{H}^T \mathbf{T} \boldsymbol{H} & \boldsymbol{H}^T \mathbf{T} \boldsymbol{\Sigma} \\ \boldsymbol{\Sigma}^T \mathbf{T} \boldsymbol{\Lambda} & \boldsymbol{\Sigma}^T \mathbf{T} \boldsymbol{H} & \boldsymbol{\Sigma}^T \mathbf{T} \boldsymbol{\Sigma} \end{pmatrix}, \tag{2.13}$$

where $\mathbf{T}$ is 1.134. Recalling $\mathbf{T}_\phi$'s definition from 1.93 and recognizing that loop functions are inherently solenoidal, it becomes evident that

$$\boldsymbol{\Lambda}^T \mathbf{T}_\phi = \mathbf{0} \tag{2.14}$$

$$\boldsymbol{H}^T \mathbf{T}_\phi = \mathbf{0} \tag{2.15}$$

$$\mathbf{T}_\phi \boldsymbol{\Lambda} = \mathbf{0} \tag{2.16}$$

$$\mathbf{T}_\phi \boldsymbol{H} = \mathbf{0}\,. \tag{2.17}$$

This insight allows the product $\boldsymbol{A}^T \mathbf{T} \boldsymbol{A}$ to be succinctly rewritten as

$$\begin{aligned} \boldsymbol{A}^T \mathbf{T} \boldsymbol{A} &= \begin{pmatrix} \boldsymbol{\Lambda}^T(-jk\mathbf{T}_A)\boldsymbol{\Lambda} & \boldsymbol{\Lambda}^T(-jk\mathbf{T}_A)\boldsymbol{H} & \boldsymbol{\Lambda}^T(-jk\mathbf{T}_A)\boldsymbol{\Sigma} \\ \boldsymbol{H}^T(-jk\mathbf{T}_A)\boldsymbol{\Lambda} & \boldsymbol{H}^T(-jk\mathbf{T}_A)\boldsymbol{H} & \boldsymbol{H}^T(-jk\mathbf{T}_A)\boldsymbol{\Sigma} \\ \boldsymbol{\Sigma}^T(-jk\mathbf{T}_A)\boldsymbol{\Lambda} & \boldsymbol{\Sigma}^T(-jk\mathbf{T}_A)\boldsymbol{H} & \boldsymbol{\Sigma}^T(-jk\mathbf{T}_A + \frac{1}{jk}\mathbf{T}_\phi)\boldsymbol{\Sigma} \end{pmatrix} \\ &= \begin{pmatrix} \mathcal{O}(k) & \mathcal{O}(k) & \mathcal{O}(k) \\ \mathcal{O}(k) & \mathcal{O}(k) & \mathcal{O}(k) \\ \mathcal{O}(k) & \mathcal{O}(k) & \mathcal{O}(\frac{1}{k}) \end{pmatrix} \end{aligned} \tag{2.18}$$

where $\mathbf{T}_A$ is 1.136. Note that in the static limit this problem can be formulated in terms of the scalar operators $\mathcal{S}$ and $\mathcal{N}$ defined in 1.98 - 1.101, as clearly elucidated in [34]. The matrix's conditioning behavior is then appraised through the Gershgorin

circle theorem, which states that given a matrix $\mathbf{M} \in \mathbb{C}^{N\times N}$, for any $i = 1, \ldots, N$, define $R_i = \sum_{j\neq i} |(\mathbf{M})_{ij}|$ and $D_i(\mathbf{M}_{ii}, R_i)$ as the closed disk centered at $\mathbf{M}_{ii}$ with radius R_i. These disks are termed Gershgorin disks. All eigenvalues of $\mathbf{M}$ lie within the union of these Gershgorin disks.

From the application of the Gershgorin Circle Theorem, it is discernible that the eigenvalues exhibit two distinct clustering behaviors: one tending towards zero at a rate of $\mathcal{O}(k)$, and the other escalating towards infinity as $\mathcal{O}(1/k)$. This leads to a condition number that scales as $\mathcal{O}(1/k^2)$, aligning with the anticipations regarding the low-frequency breakdown. A remedy to this issue is introduced through the incorporation of specific scalings within the decomposition matrix:

$$\boldsymbol{A}_s = \begin{pmatrix} \frac{1}{\sqrt{k}}\boldsymbol{\Lambda} & \frac{1}{\sqrt{k}}\boldsymbol{H} & \sqrt{k}\boldsymbol{\Sigma} \end{pmatrix}. \tag{2.19}$$

This adjustment leads to a transformed scaling of the blocks in the preconditioned matrix $\boldsymbol{A}_s^T\mathbf{T}\boldsymbol{A}_s$, articulated as:

$$\boldsymbol{A}_s^T\mathbf{T}\boldsymbol{A}_s = \begin{pmatrix} \mathcal{O}(1) & \mathcal{O}(1) & \mathcal{O}(k) \\ \mathcal{O}(1) & \mathcal{O}(1) & \mathcal{O}(k) \\ \mathcal{O}(k) & \mathcal{O}(k) & \mathcal{O}(1) \end{pmatrix}. \tag{2.20}$$

By virtue of the Gershgorin Circle Theorem, it can be deduced that the eigenvalues of this matrix converge to constant values with diminishing radii, thus rendering the system well-conditioned. Specifically, the condition number of $\boldsymbol{A}_s^T\mathbf{T}\boldsymbol{A}_s$ is rendered invariant with respect to frequency fluctuations.

However, a notable limitation associated with this preconditioning strategy is its introduction of an alternative form of ill-conditioning that is contingent upon the mesh discretization. As elucidated in [11], the condition number of $\mathbf{G}^{\Lambda\Sigma} = [\boldsymbol{\Lambda} \quad \boldsymbol{\Sigma}]^T\mathbf{G}[\boldsymbol{\Lambda} \quad \boldsymbol{\Sigma}]$, where $\mathbf{G}$ represents the well-conditioned Gram matrix of the RWG basis, experiences an augmentation proportional to $\mathcal{O}(1/h^2)$. This escalation adversely affects the condition number of the decomposed (PEC)-MFIE operator. This dilemma stems from the fact that the quasi-Helmholtz decomposition, in this scenario, is derived through differential operators, which inherently possess a non-flat spectrum. Nevertheless, this complication can be rectified by resorting to projectors and operators characterized by flat, rectangular spectra.

2.2.3 Quasi-Helmholtz Projection

Given a vector field $\boldsymbol{x}$ expressed through RWG functions, the objective is to identify a projection operator $\mathbf{P}^{\Sigma}$ that maps $\boldsymbol{x}$ to its non-solenoidal component $\boldsymbol{x}^{ns}$, which resides within the range of $\boldsymbol{\Sigma}$, symbolized as $\mathcal{R}(\boldsymbol{\Sigma})$, ensuring that $\boldsymbol{x}^{ns}$ is the closest approximation to $\boldsymbol{x}$. Adhering to the projection theorem, the discrepancy $(\boldsymbol{x} - \boldsymbol{x}^{ns})$

is orthogonal to $\mathcal{R}(\mathbf{\Sigma})$, indicating its presence in the nullspace of $\mathbf{\Sigma}^T$, denoted as $\mathcal{N}(\mathbf{\Sigma}^T)$:

$$\mathbf{\Sigma}^T(\boldsymbol{x} - \mathbf{P}^{\Sigma}\boldsymbol{x}) = 0 \iff \mathbf{\Sigma}^T\boldsymbol{x} = \mathbf{\Sigma}^T\mathbf{P}^{\Sigma}\boldsymbol{x}.$$

The matrix $\mathbf{P}^{\Sigma} = \mathbf{\Sigma}(\mathbf{\Sigma}^T\mathbf{\Sigma})^{+}\mathbf{\Sigma}^T$, employing Moore-Penrose pseudo-inversion denoted by $^{+}$, fulfills equation 2.21. This matrix is not only a projector, i.e., $(\mathbf{P}^{\Sigma})^2 = \mathbf{P}^{\Sigma}$, but it also constitutes an orthogonal projector with $\mathcal{R}(\mathbf{P}^{\Sigma}) \perp \mathcal{N}(\mathbf{P}^{\Sigma})$ [36]. The complementary projector to the solenoidal space, $\mathbf{P}^{\Lambda H}$, projects onto the entire RWG solenoidal subspace, inclusive of both local and global loops. Consequently, the quasi-Helmholtz projectors within the RWG functional domain are delineated as:

$$\mathbf{P}^{\Sigma} = \mathbf{\Sigma}(\mathbf{\Sigma}^T\mathbf{\Sigma})^{+}\mathbf{\Sigma}^T \tag{2.21}$$

$$\mathbf{P}^{\Lambda H} = 1 - \mathbf{P}^{\Sigma}. \tag{2.22}$$

In a parallel fashion, dual quasi-Helmholtz projectors are conceptualized, aiming at the BC non-solenoidal and solenoidal subspaces, respectively:

$$\mathbb{P}^{\Lambda} = \mathbf{\Lambda}(\mathbf{\Lambda}^T\mathbf{\Lambda})^{+}\mathbf{\Lambda}^T \tag{2.23}$$

$$\mathbb{P}^{\Sigma H} = 1 - \mathbb{P}^{\Lambda}. \tag{2.24}$$

Quasi-Helmholtz projectors can be ingeniously utilized to delineate and independently rescale the segments of the operator that correlate with solenoidal or non-solenoidal source and testing functions. When the electric field integral operator $\mathbf{T}$ undergoes left- and right-multiplication by the identity matrix expressed as $\mathbf{I} = \mathbf{P}^{\Lambda H} + \mathbf{P}^{\Sigma}$, it manifests as

$$\begin{aligned}\mathbf{T} &= (\mathbf{P}^{\Lambda H} + \mathbf{P}^{\Sigma})\mathbf{T}(\mathbf{P}^{\Lambda H} + \mathbf{P}^{\Sigma}) \\ &= -jk\mathbf{P}^{\Lambda H}\mathbf{T}_A\mathbf{P}^{\Lambda H} - jk\mathbf{P}^{\Lambda H}\mathbf{T}_A\mathbf{P}^{\Sigma} - jk\mathbf{P}^{\Sigma}\mathbf{T}_A\mathbf{P}^{\Lambda H} \\ &\quad + \mathbf{P}^{\Sigma}\left(-jk\mathbf{T}_A + \frac{1}{jk}\mathbf{T}_{\phi}\right)\mathbf{P}^{\Sigma},\end{aligned} \tag{2.25}$$

with the simplifying assumptions $\mathbf{P}^{\Lambda H}\mathbf{T}_{\phi} = \mathbf{T}_{\phi}\mathbf{P}^{\Lambda H} = \mathbf{0}$ being applied.

The preconditioning strategy for the (PEC)-EFIE utilizing Quasi-Helmholtz projectors involves defining left and right preconditioning matrices as

$$\mathbf{L} = \alpha\mathbf{P}^{\Lambda H} + \beta\mathbf{P}^{\Sigma}, \tag{2.26}$$

$$\mathbf{R} = \gamma\mathbf{P}^{\Lambda H} + \delta\mathbf{P}^{\Sigma}, \tag{2.27}$$

where α, β, γ, and δ are scaling coefficients selected to ensure the resulting matrix is well-conditioned, akin to the loop-star decomposition approach. The resultant system to be solved is given by

$$\begin{cases}\eta\boldsymbol{L}^T\mathbf{T}\boldsymbol{R}\mathrm{y} = \boldsymbol{L}^T\mathrm{b}, \\ \mathrm{j} = \boldsymbol{R}\mathrm{y},\end{cases}. \tag{2.28}$$

This preconditioning technique, distinct from the loop-star decomposition, is immune to the mesh discretization ill-conditioning, ensuring that the condition number of $\boldsymbol{L}^T\mathbf{T}\boldsymbol{R}$ does not exceed cond($\mathbf{T}$). This advantage stems from the non-differential nature of the projectors, with the overall differential contribution of $\boldsymbol{\Sigma}$ nullified in the $\mathbf{P}^{\Sigma}$ expression, as numerically demonstrated in fig. 2.1. Moreover, it obviates the need for explicit identification of global loops. However, it is crucial to recognize that this aspect also limits the freedom in choosing rescaling coefficients, as blocks associated with global loops cannot be independently rescaled from the remaining solenoidal functions.

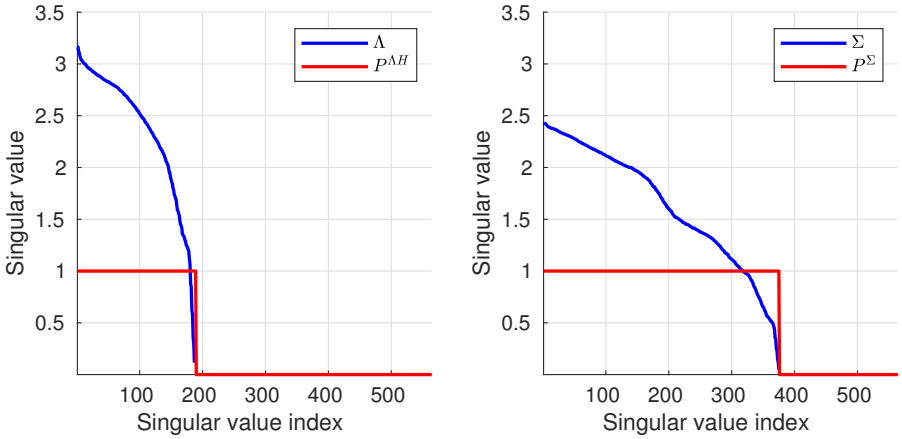

Figure 2.1: Singular values of $\boldsymbol{\Lambda}$ and $\mathbf{P}^{\Lambda H}$ (left) and of $\boldsymbol{\Sigma}$ and $\mathbf{P}^{\Sigma}$ (right) for a sphere discretized with 188 vertices, 376 cells and 564 edges.

2.3 Introduction to matrix spectral manipulation

As we've seen many times in this section, the spectral properties of the operator matrices involved are central in determining the effectiveness of many solution methods. It would thus be nice to be able to manipulate the spectral properties of those matrices. Let's now better explain what do we mean by filtering and spectral manipulation. We will here introduce filtering and spectral projector using the SVD.

Filtering by SVD

The most straightforward approach would be to start with the computation of the SVD of the matrix, namely

$$\mathbf{X} = \mathbf{U}_{\mathbf{x}}\mathbf{S}_{\mathbf{X}}\mathbf{V}_{\mathbf{X}}^{\mathbf{T}}, \quad [\mathbf{S}_{\mathbf{X}}]_{ii} = \sigma_{\mathbf{X},i}, \tag{2.29}$$

where $\mathbf{U_x}$ and $\mathbf{V_x}$ are unary and $\mathbf{S_X}$ is a block-diagonal matrix with the singular values $\sigma_{\mathbf{X},i}$ of $\mathbf{X}$ as entries in decreasing magnitude order. Then, we can arbitrarily set to zero the unwanted part of the spectrum, i.e., to impose the rank of a matrix to be constant and equal to n keeping at the same time the most of the information content of the matrix. We define the filtered matrix $\mathbf{X}_n$ as

$$\mathbf{X}_n = \mathbf{U_x}\mathbf{S}_{\mathbf{X},n}\mathbf{V}_{\mathbf{X}}^{\mathbf{T}}, \quad [\mathbf{S}_{\mathbf{X},n}]_{ii} = \begin{cases} 0, & \text{if } i \leq n \\ [\mathbf{S_X}]_{ii}, & \text{if } i > n \end{cases} . \tag{2.30}$$

This can also be seen as the application of a projector $\mathbf{P} : [\mathbf{P}_n]_{ii} = \begin{cases} 0, & \text{if } i \leq n \\ 1, & \text{if } i > n \end{cases}$ on the singular value matrix, obtaining the filtered singular value matrix denoted here with $\mathbf{S}_{\mathbf{X},n}$, and then the reconstruction of the matrix by multiplication with the left and right singular vectors. Obviously, depending on the used projector we can obtain different types of filters, arbitrarily deciding which singular values we keep and which we discard. As we know, the SVD operation involved in this approach is prohibitively expensive, but there exists (and we'll later introduce) effective ways of achieving the same result in a computationally efficient manner.

Error introduced by spectral manipulation

Whenever we alter the spectrum of a matrix and we build its filtered counterpart, we should expect the filtered matrix to be a slight modification of the original one. More in detail, we can bound the error that we introduce while filtering as

$$\begin{aligned} \mathbf{E} = \mathbf{X} - \mathbf{X}_n &= \mathbf{U_x}\mathbf{S_X}\mathbf{V}_{\mathbf{X}}^{\mathbf{T}} - \mathbf{U_x}\mathbf{S}_{\mathbf{X},n}\mathbf{V}_{\mathbf{X}}^{\mathbf{T}} \\ &= \mathbf{U_x}(\mathbf{S_X} - \mathbf{S}_{\mathbf{X},n})\mathbf{V}_{\mathbf{X}}^{\mathbf{T}} \\ &= \mathbf{U_x}\mathbf{S}_{\mathbf{E},n}\mathbf{V}_{\mathbf{X}}^{\mathbf{T}} \end{aligned} \tag{2.31}$$

with $\mathbf{S}_{\mathbf{E},n} : [\mathbf{E}_n]_{ii} = \begin{cases} 0, & \text{if } i \leq n \\ \sigma_{\mathbf{X},i}, & \text{if } i > n \end{cases}$. Using the Frobenius norm of the error matrix

$$\|\mathbf{E}\|_F = \sqrt{\sum_{i=n-k+1}^{n} \sigma_{\mathbf{X},i}^2}, \tag{2.32}$$

which tells us that the error we introduce is of the order of the highest singular value we truncate. Notice that numerical methods always come with an associated error, which is often determined by the numerical integration accuracy. Thus, as a first rule of thumb, it's acceptable to set the filtering threshold at the first singular vectors with magnitude comparable to numerical integration accuracy. Further investigations about the acceptability of the introduced error are open research fields.

2.3.1 Eigenvalue perturbation theory

When dealing with matrices with a null-space, or with clustering eigenvalues or singular values, some considerations needs to be taken into account when dealing with spectral decompositions (eigenvalue decomposition or singular value decomposition). In this section, we will firstly introduce Davis-Kahan Theorem, and then delve into its consequences in concrete scenarios: clustering spectrum due to symmetry, and null-space created by filtering.

Davis-Kahan Theorem

Let A and $A + E$ be Hermitian matrices, with E being a perturbation matrix. Let λ_i and λ_j be eigenvalues of A and $A + E$, respectively, and let u_i and v_j be the corresponding eigenvectors. The angle θ between u_i and v_j is bounded by:

$$\sin(\theta) \leq \frac{\|E\|_2}{\delta}, \tag{2.33}$$

where $\delta = \min_{i \neq k} |\lambda_i - \lambda_k|$ is the separation between the eigenvalues of A.

Additionally, let $\mathcal{U}$ and $\mathcal{V}$ be subspaces spanned by some sets of eigenvectors of A and $A + E$, respectively. Define the angle Θ between these subspaces as the largest principal angle between any pair of vectors from $\mathcal{U}$ and $\mathcal{V}$. Then,

$$\sin(\theta) \leq \frac{\|E\|_2}{\delta^*}, \tag{2.34}$$

where $\delta^* = \min(|\lambda_i - \mu_j| : \lambda_i \in \text{spec}(A), \mu_j \in \text{spec}(A + E))$ is the separation between the parts of the spectra of A and $A + E$.

Recall that every numerical matrix at least include machine error, with in double precision arithmetic is of order 10^{-16}. This theorem explains two phenomena we often encounter in singular vector or eigenvector projections plot B: clustering of singular values or eigenvalues due to symmetry and due to filtering.

Clustering spectrum due to symmetry

According to the analysis of [37], it turns out that all the scalar operators 1.98-1.101, when computed in two dimensions on the circle, have eigenvalues which are equal in pairs. By the relationship between eigenvalues and singular values it is easy to understand that also singular values follow the same rule. This is evident in numerical results, as shown in Fig. 2.2.

Clustering due to filtering

When we filter a matrix, we introduce an artificial null-space into its spectrum. This results in a subspace with $\delta^* = 0$, thus removing every constraint on the

eigenvector correspondence. Thus, when checking the eigenvector corruption due to a filtering algorithm, it is not enough to compute the numerical difference among the eigenvector matrices before and after the filtering. It only make sense to compute such a difference on the columns of such matrices spanning the unfiltered subspace; or to consider the filtered matrix eigenvalue spectrum, together with the projection of the eigenvector matrices before and after the filtering, one against each other. On such a visualization, exemplified in Fig. 2.2 if no corruption takes place, we expect to see a diagonal part before the filter cutoff, and a messy one in correspondence with the null-space.

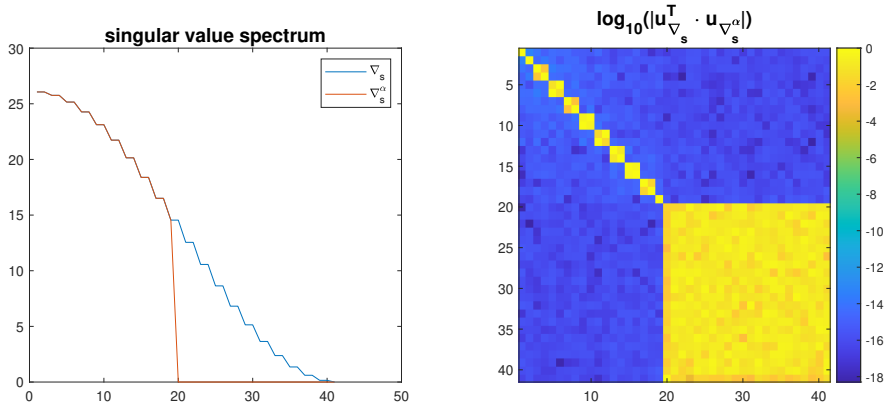

Figure 2.2: Singular value clustering due to symmetry (below filtering threshold) and null-space (after threshold). The figure has been obtained decomposing the Laplacian, filtering, recomposing the filtered Laplacian, adding noise with magnitude equal to machine precision, and then decomposing the Laplacian again.

2.4 Laplacian Multiplicative filters

Laplacian filters introduced in [38] are an effective way to carry out spectral manipulation in almost linear complexity. The idea is to be able to filter the operator in a multiplicative way. Being $\mathbf{F}$ the filter matrix with filtering threshold n and $\mathbf{X}$ the operator of interest, we'd like to achieve

$$\mathbf{X}_n = \mathbf{F}\mathbf{X}. \tag{2.35}$$

Ideally, to obtain a filtered version of the operator $\mathbf{X}$ as $\mathbf{F}\mathbf{X}$, and supposing our filter is a projector (i.e., it is a normal matrix with $\mathbf{U_F} = \mathbf{V_F}$ and $[\mathbf{S_F}]_{ii} \in \{0, 1\}$), we need

$$\mathbf{F}\mathbf{X} = \mathbf{U_F}\mathbf{S_F}\mathbf{U_F}^H\mathbf{U_X}\mathbf{S_X}\mathbf{V_X}^H = \mathbf{U_X}\mathbf{S_F}\mathbf{S_X}\mathbf{V_X}^H \tag{2.36}$$

which means that $\mathbf{U_F}^H\mathbf{U_X} = \mathbf{I}$, i.e., the filter must share the left singular vectors of $\mathbf{X}$. With the same logic, to obtain a filtered version of the operator $\mathbf{X}$ as $\mathbf{XF}$, we need $\mathbf{V_X}^H\mathbf{V_F} = \mathbf{I}$, i.e., the filter must share the right singular vectors of $\mathbf{X}$. In order to have commutation between filter and operator, by the way, also $\mathbf{X}$ must be normal, but we don't need its left and right eigenvectors to be identical: they can differ by a complex, unitary constant, which can be different for each of them. So,

$$\mathbf{U_X} = \mathbf{V_X}\mathbf{C} \tag{2.37}$$

with $\mathbf{C}$ diagonal, complex, $[\mathbf{C}]_{i,i} = 1$. Hence, we can rewrite

$$\mathbf{X} = \mathbf{V_X}\mathbf{C}\mathbf{S_X}\mathbf{V_X}^H \tag{2.38}$$

where $\mathbf{CS_X}$ is a diagonal matrix, thus $\mathbf{X}$ is finally diagonalized by $\mathbf{V_X}$. Note that for both U and V, their hermitian equals the inverse since they represents othonormal basis.

On top of that, we need fast algorithms for computation and storage of $\mathbf{F}$, as well as for the multiplication $\mathbf{FX}$.

2.4.1 The special role of the graph Laplacians

In this section, the theoretical framework behind the effectiveness of the Graph Laplacians as filters is presented. First, the discrete mesh graph Laplacians are introduced, subsequently, we will see how they are related to the operators of interest; to conclude, fast methods for the computation of the filtered graph Laplacians are introduced.

First order differential operators

Here we present a possibly mathematically inexact interpretation of the loop and star basis as differential operators on manifolds, and from this intuition we postulate the foundations for the effectiveness of the graph Laplacian operators for filtering purposes.

We start by recalling the four differential operators, which maps vector into scalar quantities and vice-versa:

$$\text{grad}\phi = \nabla\phi \quad : \quad \mathbb{C} \to \mathbb{C}^n, \tag{2.39}$$

$$\text{div}\mathbf{v} = \nabla \cdot \mathbf{v} \quad : \quad \mathbb{C}^n \to \mathbb{C}, \tag{2.40}$$

$$\text{curl}\phi = \nabla \times (\hat{n} \cdot \phi) \quad : \quad \mathbb{C} \to \mathbb{C}^n, \tag{2.41}$$

$$\text{curl}\mathbf{v} = \hat{n} \cdot (\nabla \times \mathbf{v}) \quad : \quad \mathbb{C}^n \to \mathbb{C} \tag{2.42}$$

with $\phi \in \mathbb{C}$ being a scalar function and $\mathbf{v} \in \mathbb{C}^n$ being a vector field. According to the divergence theorem, the volume integral of the divergence of a vector field over

a volume V equals the flux of the vector field through the boundary surface S of the volume

$$\int_V \nabla \cdot \mathbf{v}\, dV = \int_S \mathbf{v} \cdot \mathbf{n}\, dS. \tag{2.43}$$

Applying integration by parts to a scalar field ϕ and a vector field $\mathbf{v}$ gives:

$$\int_V \phi(\nabla \cdot \mathbf{v})\, dV = -\int_V (\nabla\phi) \cdot \mathbf{v}\, dV + \int_S \phi\mathbf{v} \cdot \mathbf{n}\, dS. \tag{2.44}$$

If ϕ and $\mathbf{v}$ vanish on S, the surface integral disappears, showing the fundamental relationship between the gradient and divergence as adjoint operators. Upon discretization, representing the gradient operator ∇ by a matrix G and the divergence operator $\nabla\cdot$ by a matrix D, Eq. 2.44 implies

$$\langle \nabla\phi, \mathbf{v} \rangle = -\langle \phi, \nabla \cdot \mathbf{v} \rangle, \tag{2.45}$$

which shows that the matrix D is the adjoint of the matrix G, thus $D = G^H$. An equivalent procedure leads to the conclusion that also curlϕ is the adjoint of curl$\mathbf{v}$.

Now, we consider a vector field $\mathbf{v}$ discretized on a manifold using RWG basis functions introduced in section 1.5.3. we can now interpreter the quasi-Helmholtz decomposition theorem presented in Eq. 2.8 (discretized by loop and star basis functions) as the application of the two scalar operators: the vector curl of loops plus the gradient of the stars yields the field.

It is worth noticing that both loop-to-RWG and star-to-RWG matrices $\mathbf{\Lambda}$ and $\mathbf{\Sigma}$ are respectively the primary and dual graph divergences, considering as primary graph the vertices one and as secondary the faces one. This stems from their definition, which is the one of a differential operator, assigning a $+1$ and a -1 weight to every graph element (respectively, vertex or face). As a consequence, we can interpreter those matrices as disceretizations of the operators 2.41 and 2.40, and their adjoints $\mathbf{\Lambda}^T$ and $\mathbf{\Sigma}^T$ as disceretizations of 2.42 and 2.39 [11, 39]. On the dual mesh defined on the barycentric refinement [9], the role of such matrices is inverted, with $\mathbf{\Lambda}$ becoming the divergence operator and $\mathbf{\Sigma}$ becoming the curl operator.

Second order differential operators

the Laplace operator (or Laplacian) is a differential operator given by the divergence of the gradient of a scalar function on Euclidean space

$$\text{grad}(\text{div}\mathbf{v}) = \Delta\mathbf{v} \quad : \quad \mathbb{C}^n \to \mathbb{C}^n. \tag{2.46}$$

We are particularly interested in its discrete incarnations, as graph Laplacian and discrete Laplace-Beltrami operator in particular. Building on the definitions given

in the previous section, it is straightforward to compute the primary and dual graph Laplacians as [38]

$$\mathbf{\Delta}^{ns} = \mathbf{\Sigma}^T\mathbf{\Sigma}, \tag{2.47}$$

$$\mathbf{\Delta}^{s} = \mathbf{\Lambda}^T\mathbf{\Lambda}. \tag{2.48}$$

Note that these operators does not take into account the physical dimensions of the manifold, but describe only the differential property of the mesh.

The Laplace-Beltrami operator, on the other hand, for a two-dimensional manifold RWG mesh, can be built from the following discretization

$$[\overline{\overline{G}}^{\mathbf{\Lambda}}]_{i,j} = \langle \nabla \times \hat{n}\lambda_i, \nabla \times \hat{n}\lambda_i \rangle = \langle \nabla_s \cdot \lambda_i, \nabla_s \cdot \lambda_j) \rangle \tag{2.49}$$

$$\overline{\overline{\mathbf{G}}}^{\mathbf{\Lambda}} = \mathbf{\Lambda}^{\mathbf{H}}\mathbf{G}\mathbf{\Lambda}, \tag{2.50}$$

where $\mathbf{G}$ is the RWG gram matrix for the given manifold; or, for duality, as $\overline{\overline{\mathbf{G}}}^{\mathbf{\Sigma}} = \mathbf{\Sigma}^{\mathbf{H}}\mathbf{G}\mathbf{\Sigma}$ [11].

Note that it can be proved that any valid preconditioning scheme for $\overline{\overline{\mathbf{G}}}^{\mathbf{\Sigma}}$ applies also to $\mathbf{\Delta}^{ns}$, and any valid preconditioner for $\overline{\overline{\mathbf{G}}}^{\mathbf{\Lambda}}$ applies also to $\mathbf{\Delta}^{s}$ [11].

2.4.2 Filtered graph Laplacians as multiplicative preconditioners

The idea of filtered Laplacians as preconditioners is suggested by some analogies between the wavelet spectral properties of the Laplacian and of the integral operators of interest [40, 41]. However, a clear theoretical framework behind the effectiveness of this approach is still under investigation.

We can define the filtered graph Laplacians [38]

$$(\mathbf{X}^T\mathbf{X})_n = \mathbf{V}_{\mathbf{X}}\mathbf{L}_{\mathbf{X}}^2{}_n\mathbf{V}_{\mathbf{X}}{}^T \tag{2.51}$$

where $\mathbf{X}$ can either represent the loop-to-RWG $\mathbf{\Lambda}$ or start-to-RWG $\mathbf{\Sigma}$ matrix, $\mathbf{V}_{\mathbf{X}}$ are its right singular vectors and $\mathbf{L}_{\mathbf{X}}$ is its singular value matrices (diagonal, with SV in descending order). Now, the new filtered loop and filtered star basis functions can be introduced, with filtered loop-to-RWG and filtered star-to-RWG matrices defined as

$$\mathbf{\Sigma}_n = \mathbf{\Sigma}\left(\mathbf{\Sigma}^{\mathrm{T}}\mathbf{\Sigma}\right)^{+}\left(\mathbf{\Sigma}^{\mathrm{T}}\mathbf{\Sigma}\right)_n, \tag{2.52}$$

$$\mathbf{\Lambda}_n = \mathbf{\Lambda}\left(\mathbf{\Lambda}^{\mathrm{T}}\mathbf{\Lambda}\right)^{+}\left(\mathbf{\Lambda}^{\mathrm{T}}\mathbf{\Lambda}\right)_n. \tag{2.53}$$

The new basis function inherits most of the properties of the loop and star basis functions, such as loop-star orthogonality. In addition, it can be proved that non-intersecting differences of loop or star matrices are mutually orthogonal, and that $\mathbf{X^T}_m\mathbf{X}_n = \mathbf{X^T}_{\min(n,m)}\mathbf{X}_{\min(n,m)}$. This implies that $\mathbf{X^T}\mathbf{X}_n = \mathbf{X^T}_n\mathbf{X}_n$.

2.4.3 Efficient computation of the graph Laplacian multiplicative filter

The filtering proposed in Eq. 2.51 relies on SVD, which is, as already discussed, computationally inefficient. In this section, efficient methods to perform matrix-vector product for the filtered graph Laplacians $\left(\mathbf{\Lambda}^{\mathrm{T}}\mathbf{\Lambda}\right)_n$ and $\left(\mathbf{\Sigma}^{\mathrm{T}}\mathbf{\Sigma}\right)_n$ are proposed, both in case of constant and variable filtering threshold w.r.t the number of unknowns. Numerical results on the obtained spectra are deferred to section 4.3, while the effectiveness of the resulting solvers is proved in [38].

Constant filtering threshold

In such context, there are two viable algorithms to achieve efficient filtering, namely preconditioned inverse power methods [42] and Butterworth matrix filters.

The first method proposed yield the last singular vectors and singular values of the $\mathbf{\Sigma}^{\mathrm{T}}\mathbf{\Sigma}$ and $\mathbf{\Lambda}^{\mathrm{T}}\mathbf{\Lambda}$ matrices at the price of a constant number of matrix-vector products. Given the sparsity of such matrices, the resulting method is linear in complexity and the filtered projectors can be efficiently obtained.

The Butterworth matrix filtering method is a matrix extension of the well-known Butterworth filter, which is, for order m and cutoff parameter $x_c > 0$, characterized by

$$f_{m,x_c}(x) = (1 + (x/x_c)^m)^{-1}, \quad x \geq 0. \tag{2.54}$$

The spectrum of a symmetric positive matrix $\mathbf{A} \in \mathbb{R}^{N\times N}$, composed of the set of singular values $\{\sigma_i(\mathbf{A})\}_i$, can be filtered by extending f_{m,x_c} to matrix arguments and applying it to $\mathbf{A}$, resulting in the filtered matrix

$$\mathbf{A}_{\text{filt}} := f_{m,x_c}(\mathbf{A}) = (I + (\mathbf{A}/x_c)^m)^{-1}, \tag{2.55}$$

with singular values $\{f_{m,x_c}(\sigma_i(\mathbf{A}))\}_i$. The filtered matrix $(\mathbf{\Sigma}^T\mathbf{\Sigma})_n$ can then be expressed as

$$(\mathbf{\Sigma}^T\mathbf{\Sigma})_n = (\mathbf{\Sigma}^T\mathbf{\Sigma}) \lim_{m\to\infty} f_{m,\sigma_n(\mathbf{\Sigma}^T\mathbf{\Sigma})}(\mathbf{\Sigma}^T\mathbf{\Sigma}). \tag{2.56}$$

In practical cases, the computation can be halted after few iterations, in fact, filters of order $n \in (10{,}100)$ provide already very good result 4.3. Further stabilization and implementation details can be found in [38].

Unknowns-proportional filtering threshold

When the filtering index is proportional to the number of unknowns, we can leverage the ideas of polynomial preconditioning and graph wavelets [41, 43, 44] and adopt a method based on a polynomial expansion of the spectral filter.

Given that we are interested in cases where the filtering index is proportional to the number of degrees of freedom, we can use a polynomial approximation of

f_{m,x_c} on the interval $[0, \sigma_{N_S}(\mathbf{\Sigma}^T\mathbf{\Sigma})]$. A natural basis for this approximation is the Chebyshev polynomials $\{T_n(x)\}_n$, defined by the recurrence relation

$$T_n(x) = \begin{cases} 1 & \text{if } n = 0 \\ x & \text{if } n = 1 \\ 2xT_{n-1}(x) - T_{n-2}(x) & \text{otherwise.} \end{cases} \tag{2.57}$$

The approximated filtered matrix now reads

$$(\mathbf{\Sigma}^T\mathbf{\Sigma})_n \approx -\frac{c_0}{2}\mathbf{I} + \sum_{k=1}^{n_c} c_k T_k \left(\frac{\mathbf{\Sigma}^T\mathbf{\Sigma}}{\sigma_n(\mathbf{\Sigma}^T\mathbf{\Sigma})} \right), \tag{2.58}$$

where the c_n are the expansion coefficients of $f_{m,\sigma_n(\mathbf{\Sigma}^T\mathbf{\Sigma})}$ in the basis of the first $n_c + 1$ Chebyshev polynomials. The filters obtained by following this approach will require the same number of sparse matrix-vector multiplications for increasing discretization when the filtering index is proportional to the number of degrees of freedom. Further details can be found in [38].

Chapter 3

Non-uniform discretization

In this chapter, a qualitative and quantitative analysis of the behavior of integral operators on non-uniform discretized meshes and non-regular geometries has been performed. It is notable that on regular manifolds, i.e., circle and sphere, respectively in 2D and 3D, all the problems discussed in this thesis have trivial solutions by the application of the Fourier transform, or Spherical Harmonic transform in 3D. These very versatile tools, which also have fast implementations, diagonalize integral and differential operators, leading to very efficient solution strategies in linear complexity. This chapter is structured as follows: we start by discussing how these circular domains are of few practical interest for real world applications, then, we will discuss which are the properties of such domains that make calculations so effective on them. We will then discuss what happens to these nice and efficient formulation when we slightly move away from circular geometries, adding some irregularity in the discretization or in the geometry itself. We will also discuss the relevant fast algorithm for non-uniform settings, and discuss possible strategies, approaches and schemes.

3.1 The advantages of non-uniform discretization schemes

In computational electromagnetics, uniform discretization is often impractical due to the inherent inefficiencies and excessive computational demands it imposes. Two factors can determine the size of the mesh elements:

- the simulation frequency, which dictates the minimum wavelength, thus due to Shannon therorem the needed discretization density,
- the geometry details, which may need a certain level of accuracy in the discretization to be correctly represented.

The scope of this section is to address the second case, that we will call the "Dense discretization" scenario. In uniform discretization, the entire computational domain is divided into equally sized elements. If fine details exist in small regions, the entire domain must be discretized with the same small element size to capture those details accurately. This leads to a massive number of elements, increasing the computational load significantly. The large number of elements generated by uniform discretization results in high memory usage and computational requirements. This can become unmanageable, especially for large domains or complex geometries. This represents a huge inefficiency in resource usage, that could thwart the complexity performance offered by the best numerical methods.

Non-uniform discretization, on the other hand, adapts the element size to the specific needs of different regions within the computational domain. This approach offers several advantages:

- By using smaller elements in regions with high field variations or complex geometries, and larger elements in regions with low field variations, non-uniform discretization efficiently captures important details without unnecessarily increasing the problem size.

- This adaptive approach results in a smaller overall number of elements, reducing the computational burden and memory requirements without loosing simulation accuracy

- Another advantage is the possibility to focus on the areas of greater interest inside the simulation domain, and set higher accuracy constraint only on those, leaving looser constraints on the rest of the geometry. This leads to further computational resources savings.

In real world dense discretization problems, it is common the need to have very high accuracy on some small detail (e.g., an antenna) being part of much bigger objects (i.e., a plane). To fix ideas, suppose we would like to have a discretization with mesh length DH on a detail of size SH and mesh length DL on the rest of the simulation domain with size SL. The usage of non-uniform discretization allows for a growth of the total simulation complexity $\mathcal{O}(\max(\frac{SH^2}{DH^2}, \frac{SL^2}{DL^2}))$ compared to $\mathcal{O}(\frac{SL^2}{DH^2})$ in case of uniform discretization. Notice that in practical cases the ratios $\frac{SH}{DH}$ and $\frac{SL}{DL}$ are often of similar magnitude, whereas $\frac{SL}{DH}$ may easily be a couple of orders of magnitude higher, further doubled by the square in the complexity equation.

To summarize, Non-uniform discretization is a powerful complexity reducer in computational electromagnetics, particularly in the low to mid-frequency regimes. By focusing computational resources on the areas where they are most needed and relaxing the requirements in less critical regions, it allows for efficient and

accurate simulations without the excessive computational cost associated with uniform discretization.

3.2 Properties of circular geometries

As we anticipated earlier, the circle and the sphere exhibits some very interesting properties when it comes to solving numerical problems on such manifolds. In fact, it must be noticed that the properties of the discretized operators are influenced by three factors: the operator nature, the the problem geometry and chosen discretization (basis functions, mesh points). Let's use some simple examples to fix ideas.

- Any derivative operator (such as the Laplacian) will lead to a sparse matrix, since each point result will be a linear combination of its neighbours points only.

- Any operator on a circle, with uniform discretization will lead to a circulant matrix, because each point will have the same relationship with points in equal relative positions.

- A discretized integral operator will have the highest magnitude on the biggest mesh elements, because the value of such samples are representative of bigger areas of the geometry; and for the same reason will have very low magnitude for the samples corresponding to the smallest mesh elements.

It is straightforward how such properties translates into computational schemes. A sparse matrix will be easier to compress, or may be diagonalized via permutations. A circulant matrix can be diagonalized by Fast Fourier Transform. A matrix with a wide dynamic range of value will be probably ill-conditioned and may lead to numerical cancellation issues. Let's focus on the usage of the FFT to diagonalize circulant matrices.

3.2.1 Diagonalization via FFT

We will first provide a brief recall of Fourier transform, one of the most fascinating mathematical tools of all times. Then, we will present its fast implementation, widely acknowledged as one of the most impactful algorithms of the last century. To conclude, we will explain how this transform allows for solution of linear problems described by circulant matrices in linear complexity.

Fourier transform

The Fourier transform, a mathematical operation named after Joseph Fourier, who introduced the concept in the early 19th century, is a powerful tool in both pure and applied mathematics [45]. Fourier's work, originally developed to solve problems related to heat conduction, revealed that any periodic function could be expressed as a sum of sine and cosine functions, which are the basic building blocks of harmonic analysis.

The essence of the Fourier transform lies in its ability to decompose a function into its constituent frequencies. This expressive power is particularly useful in the analysis and processing of signals, allowing us to transform a time-domain signal into its frequency-domain representation. Mathematically, the Fourier transform of a function $f(t)$ is given by

$$\hat{f}(\omega) = \int_{-\infty}^{\infty} f(t) e^{-i\omega t}\, dt \tag{3.1}$$

where $\hat{f}(\omega)$ represents the frequency components of the function $f(t)$. This transformation provides a comprehensive view of the harmonic content of $f(t)$, effectively breaking it down into complex sinusoidal components. For a function defined on a domain, the Fourier series expansion is expressed as

$$f(x) = \sum_{n=-\infty}^{\infty} c_n e^{i\frac{2\pi n x}{L}} \tag{3.2}$$

where c_n are the Fourier coefficients, calculated by

$$c_n = \frac{1}{L} \int_0^L f(x) e^{-i\frac{2\pi n x}{L}}\, dx\,. \tag{3.3}$$

Another relevant feature of the complex exponential set is that they form an orthonormal basis for the space of square-integrable periodic functions $L^2([0, L])$. It must be noted that a function defined on a circle is inherently a periodic function, because the domain can be interpreted as a period, and the function as an infinite replica of that period. This underpins the effectiveness of Fourier theory on this domain.

Discrete Fourier Transform

The discrete Fourier transform of a sequence $\{x_n\}$ of length N, which is interpreted as a uniform sampling of a periodic function, is given by

$$X_k = \sum_{n=0}^{N-1} x_n e^{-i2\pi k n/N}, \quad k = 0, 1, \ldots, N-1 \tag{3.4}$$

where X_k represents the frequency components of the sequence $\{x_n\}$. The FFT algorithm computes these coefficients rapidly by recursively breaking down the DFT into smaller DFTs, exploiting symmetries in the complex exponentials space. The inverse discrete Fourier transform (IDFT) is given by

$$x_n = \frac{1}{N} \sum_{k=0}^{N-1} X_k e^{i2\pi kn/N}, \quad n = 0, 1, \ldots, N-1 \tag{3.5}$$

where x_n represents the original sequence and X_k are the frequency components. The IDFT converts the frequency domain representation back to the time domain.

Gram matrix

As discussed in 1.5.1, for each basis function we can define a Gram matrix, which has to be taken into account when dealing with change of basis. The DFT introduces a new basis, namely the complex exponential $\phi_k(n) = e^{-i\frac{2\pi kn}{N}}$, with associated Gram matrix Gdefined as:

$$G_{k,l} = \sum_{n=0}^{N-1} \phi_k(n)\overline{\phi_l(n)} = \sum_{n=0}^{N-1} e^{-i\frac{2\pi kn}{N}} e^{i\frac{2\pi ln}{N}} = \sum_{n=0}^{N-1} e^{i\frac{2\pi(l-k)n}{N}}.$$

For $k \neq l$:

$$G_{k,l} = \sum_{n=0}^{N-1} e^{i\frac{2\pi(l-k)n}{N}} = \frac{1 - e^{i2\pi(l-k)}}{1 - e^{i\frac{2\pi(l-k)}{N}}} = 0,$$

since $e^{i2\pi(l-k)} = 1$ and $e^{i\frac{2\pi(l-k)}{N}} \neq 1$. For $k = l$:

$$G_{k,k} = \sum_{n=0}^{N-1} 1 = N.$$

Thus, the Gram matrix G is:

$$G = NI,$$

where I is the $N \times N$ identity matrix.

Fast Fourier Transform

The Fast Fourier Transform (FFT) is an efficient algorithm to compute the discrete Fourier transform (DFT) and its inverse. First proposed by Cooley and Tukey in 1965 [46] and then evolved to the its latest form FFTW [47, 48], the FFT revolutionized many fields by drastically reducing the computational complexity of the DFT from $O(N^2)$ to $O(N \log N)$, where N is the number of evenly spaced samples. One of the key applications of the FFT is in the efficient convolution

of signals. By transforming a signal into the frequency domain, convolutions can be performed as simple multiplications, which are computationally less intensive. This property is widely utilized in filtering, data compression and digital signal processing.

Application to circulant problems

Suppose we have a linear system in the form $\mathbf{Ab} = \mathbf{x}$ where $\mathbf{A}$ is a circulant matrix. The eigenvalues of $\mathbf{A}$ can be obtained by applying the DFT to the first row of $\mathbf{A}$. Let $\mathbf{a} = [a_0, a_1, \ldots, a_{N-1}]$ be the first row of A. The DFT of $\mathbf{a}$ is given by:

$$\hat{a}_k = \sum_{n=0}^{N-1} a_n e^{-i2\pi kn/N}, \quad k = 0, 1, \ldots, N-1 \tag{3.6}$$

The matrix A can then be diagonalized as:

$$\mathbf{A} = \mathbf{F}\hat{\mathbf{A}}_k\mathbf{F}^{\mathbf{H}} \tag{3.7}$$

where $\mathbf{F}$ is the normalized DFT matrix and $\hat{\mathbf{A}}_k$ is a diagonal matrix with the eigenvalues $\hat{a}_k$ on its diagonal. The entries of the DFT matrix $\mathbf{F}$ of size $N \times N$ are defined as

$$[\mathbf{F}]_{jk} = \frac{1}{\sqrt{N}} e^{-i2\pi jk/N}, \quad j, k = 0, 1, \ldots, N-1\,, \tag{3.8}$$

making $\mathbf{F}$ a unitary matrix. Note that the coefficient $\frac{1}{\sqrt{N}}$ already takes into account for the normalization w.r.t. the exponential inner product, i.e., for the inverse square gram matrix introduced in 1.5.6. This diagonalization allows us to solve the linear system efficiently as

$$\mathbf{b} = \mathbf{F}\hat{\mathbf{A}}_k^{-1}\mathbf{F}^H\mathbf{x}\,, \tag{3.9}$$

and since the DFT and its inverse can be computed rapidly using the Fast Fourier Transform (FFT) and $[\hat{\mathbf{A}}_k^{-1}]_{ii} = \frac{1}{[\hat{\mathbf{A}}_k]_{ii}}$, this approach reduces the computational complexity from $\mathcal{O}(N^3)$ to $\mathcal{O}(N \log N)$. Circular problems, where the underlying physical system exhibits rotational symmetry, are particularly well-suited for this method, since as already seen the resulting system matrices are always circulant.

3.2.2 Harmonic transforms in 3D

In extending the concepts of the Fourier transform and circulant matrices to three-dimensional problems, we encounter the natural counterpart to the discrete Fourier transform (DFT) in spherical coordinates: spherical harmonics. Spherical harmonics play a crucial role in solving problems with spherical symmetry, similar to how the DFT is used for problems with circular symmetry. Also in this case, fast schemes are available.

Spherical Harmonics Transform

In the 3D setting, many physical problems can be expressed in terms of linear systems involving spherical harmonics [49–53]. Consider a linear system of the form $\mathbf{Ab} = \mathbf{x}$ where A is now a matrix that discretize an electromagnetic operator on a sphere. In spherical coordinates, functions can be expanded in terms of spherical harmonics $Y_{lm}(\theta, \phi)$, which are the angular portion of the solution to Laplace's equation in spherical coordinates. Spherical harmonics are defined as

$$Y_{lm}(\theta, \phi) = (-1)^m \sqrt{\frac{(2l+1)}{4\pi} \frac{(l-m)!}{(l+m)!}} P_{lm}(\cos\theta) e^{im\phi} \tag{3.10}$$

where l is a non-negative integer, m is an integer such that $-l \leq m \leq l$, and $P_{lm}(\cos\theta)$ are the associated Legendre polynomials. The function $f(r, \theta, \phi)$ in spherical coordinates can be expanded as

$$f(r, \theta, \phi) = \sum_{l=0}^{\infty} \sum_{m=-l}^{l} f_{lm}(r) Y_{lm}(\theta, \phi) \tag{3.11}$$

where $f_{lm}(r)$ are the radial coefficients. This expansion is particularly useful because spherical harmonics form an orthonormal basis for the space of square-integrable functions on the sphere. The transformation from spatial domain to spherical harmonic domain can be represented as:

$$f_{lm}(r) = \int_0^{2\pi} \int_0^{\pi} f(r, \theta, \phi) Y_{lm}^*(\theta, \phi) \sin\theta \, d\theta \, d\phi \tag{3.12}$$

where $Y_{lm}^*(\theta, \phi)$ denotes the complex conjugate of the spherical harmonic function. By leveraging spherical harmonics, we can diagonalize matrices that are invariant under rotations, similar to how circulant matrices are diagonalized by the DFT.

Fast Spherical Harmonic Transform

The Fast Spherical Harmonic Transform (SHT) is an efficient algorithm designed to compute the spherical harmonic coefficients of a function defined on the surface of a sphere [54–56]. Just as the Fast Fourier Transform (FFT) accelerates the computation of the Discrete Fourier Transform (DFT), the Fast SHT reduces the computational complexity of spherical harmonic transforms from $O(N^2)$ to $O(N \log^2 N)$ for N sample points. This efficiency is crucial for applications in geophysics, astrophysics, and computational electromagnetics, where data is often naturally expressed on spherical domains. The Fast SHT leverages the hierarchical structure of the spherical harmonics and recursive algorithms to efficiently compute these coefficients. By exploiting symmetries and applying techniques similar to

those used in FFTs, the Fast SHT significantly reduces the computational burden. However, those algorithms remain quite complex, with non-trivial error bounds and numerous stability considerations to be taken into account during implementation [57]. One prominent application of the Fast SHT is in the field of global climate modeling, where data on temperature, pressure, and other variables is naturally sampled on a nearly-spherical grid, i.e., the earth.

Bi-dimensional Discrete Fourier Transform

2D-DFT is the natural extension of DFT to the planar setting. it is particularly suitable for dealing with functions which are periodic under two dimensions. Note that this is relates to spherical symmetry only under some specific discretization choices.

Let a $P \times Q$-matrix $u = \{u_{mn}; -P_1 \leq m \leq P_2, -Q_1 \leq n \leq Q_2\}$, with $P_1 = \lfloor P/2 \rfloor$, with $P_2 = P - P_1 - 1$, and $Q_1 = \lfloor Q/2 \rfloor$, $Q_2 = Q - Q_1 - 1$. Denote the nth column by $u(:, n)$ and the mth row by $u(m, :)$, and $u(m, n)$ for u_{mn}. Assume that each column $u(:, n)$ is extended to be a P-periodic sequence, and likewise, each row is extended to be a Q-periodic sequence. The 2D-DFT $\mathcal{F}_{P,Q}$, with the periods P and Q, for a (P, Q)-matrix u is defined as

$$(\mathcal{F}_{P,Q}u)(m, n) = \sum_{p=-P_1}^{P_2} \sum_{q=-Q_1}^{Q_2} u(p, q) e^{-i\left(\frac{2\pi}{P}mp + \frac{2\pi}{Q}nq\right)} \tag{3.13}$$

for all m, n. The inverse transform $\mathcal{F}_{P,Q}^{-1}$ is defined by

$$(\mathcal{F}_{P,Q}^{-1}v)(p, q) = \frac{1}{PQ} \sum_{m=-P_1}^{P_2} \sum_{n=-Q_1}^{Q_2} v(m, n) e^{i\left(\frac{2\pi}{P}pm + \frac{2\pi}{Q}qn\right)} \tag{3.14}$$

for all p, q. The 2-D DFT and its inverse transform can also be given, and usually are computed, in the terms of one-dimensional (1-D) DFT's as follows:

$$(\mathcal{T}_{P,Q}u)(m, n) = (\mathcal{T}_Q v(m, :))(n), \quad \text{where} \quad v(p, q) = (\mathcal{T}_P u(:, q))(p), \tag{3.15}$$

for all m, n, p, and q, or the order is reversed: first take $\mathcal{F}_Q$ row-wise and then $\mathcal{F}_P$ column-wise. A similar equation holds for $\mathcal{F}_{P,Q}^{-1}$ in terms of $\mathcal{F}_P^{-1}$ and $\mathcal{F}_Q^{-1}$. Since 2D-DFT can be expressed in terms of 1D-DFT, the fast implementation is straightforward employing FFT.

3.2.3 Relationship among SHT and 2D-DFT

An interesting direction of research that I explored in my BS internship was investigating the relationship among SHT and bi-dimensional DFT. In particular,

we came across a paper [58] that states that the FFT can be used to perform interpolation and anterpolation in multilevel-FMM, steps that by formal definition involve the usage of spherical harmonics [51], with even better accuracy. Given that SHT in FMM is used to do spectral filtering, we hypotized the possibility of using this approach to do operator filtering.

To effectively verify the relationship among SHT and 2D-DFT, we tried out a simple but effective test: to numerically check the band-limitedness of 2D-exponentials when expressed in spherical harmonic basis, and vice-versa.

Gram matrix definition

In order to perform these tests, at first we need to define and build the gram and mix-gram matrices for the involved basis functions. Due to the orthogonality of both the SH and 2D-exponentials basis functions, the gram matrices $\mathbf{G}_{SH,SH}$ and $\mathbf{G}_{e2,e2}$ for both basis are diagonal ones, thus the normalization can be easily included as a coefficient in the change of basis as in 3.2.1. The spherical harmonics to 2D-exponentials gram matrix is defined as $\mathbf{G}_{SH,e2} = \mathbf{G}_{SH,\delta}\mathbf{G}_{e2,\delta}$, where $\mathbf{G}_{SH,\delta}$ and $\mathbf{G}_{e2,\delta}$ are respectively the SHT and the 2D-DFT matrices. Note that the explicit usage of these matrices leads to a cubic complexity. Fast implementations shall be used instead.

Numerical results

Numerical results shows that the spherical harmonic expansion of exponentials is full, without any decay in the coefficient series. The opposite, i.e., the 2D-DFT expansion of a spherical harmonic, is band-limited in the sense that the coefficient series decays with an exponential behavior. An important note about the latter case is that the decay is only visible toward the higher frequency, but not toward the lower ones: in other words, a single order n spherical harmonic requires $\mathcal{O}(n)$ Fourier coefficients to be represented. These results highlights the absence of any sparse mapping among the two basis, but on the other hand suggest that filtering the 2D-DFT transform can effectively lead to an approximate filtering also in the spherical harmonic domain. By the way, trying to explicitly filter spherical harmonics by a 2D-DFT introduces large

3.2.4 Vector Spherical Harmonic Transform

The Vector Spherical Harmonic Transform (Vector SHT) extends the concept of spherical harmonic transforms to vector fields defined on the surface of a sphere [59, 60]. This extension is necessary because, in many physical applications, the quantities of interest are inherently vector fields rather than scalar fields. Unlike the scalar case, where spherical harmonics suffice, vector fields require a

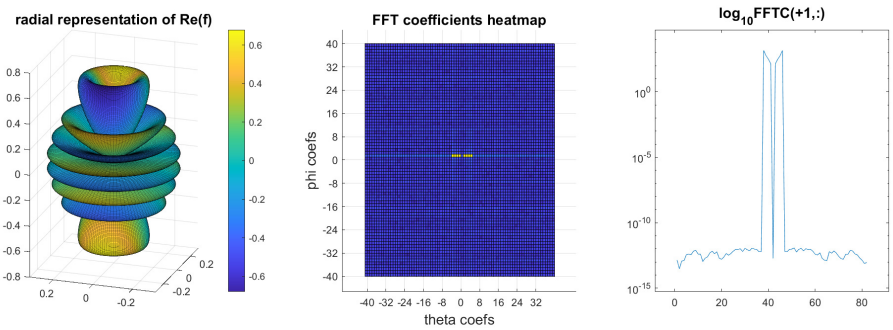

Figure 3.1: 3D representation and SHT of a 2D trigonometric polynomial of order (7,4). The linear plot is the magnitude of row of index +4 of the SHT matrix, which is the only non-zero one.

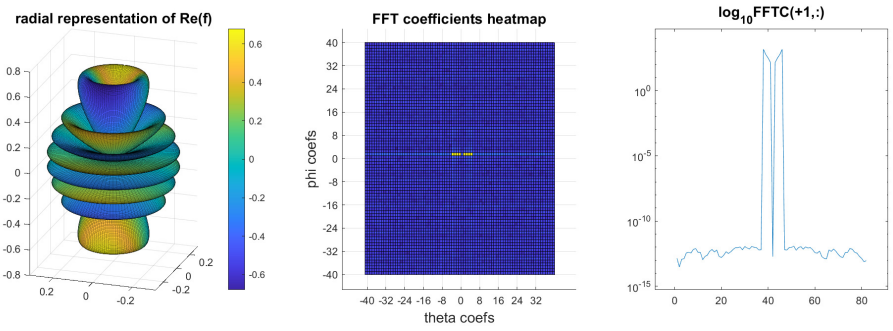

Figure 3.2: 3D representation and 2D DFT of the spherical harmonic of order $n = 8, l = 1$. The linear plot is the magnitude of row of index +1 of the 2D-DFT matrix, which is the only non-zero one.

more complex representation to capture both their magnitude and directional components accurately.

In 2D problems, vector fields can often be decomposed into scalar components that can be separately transformed using the standard Fourier transform. This simplification works well in 2D due to the lower dimensionality and the nature of planar symmetry. However, in 3D, vector fields exhibit more complex behaviors that cannot be adequately captured by scalar spherical harmonics alone.

Vector spherical harmonics are typically defined in terms of the scalar spherical harmonics and their gradients. For a vector field $\mathbf{F}(\theta, \phi)$, the expansion in terms of vector spherical harmonics $\mathbf{Y}_{lm}$, $\mathbf{\Psi}_{lm}$, and $\mathbf{\Phi}_{lm}$ is given by

$$\mathbf{F}(\theta,\phi) = \sum_{l=0}^{\infty} \sum_{m=-l}^{l} \left[a_{lm}\mathbf{Y}_{lm}(\theta,\phi) + b_{lm}\mathbf{\Psi}_{lm}(\theta,\phi) + c_{lm}\mathbf{\Phi}_{lm}(\theta,\phi) \right] \tag{3.16}$$

where $\mathbf{Y}_{lm} = Y_{lm}(\theta,\phi)\hat{r}$, $\mathbf{\Psi}_{lm}(\theta,\phi) = r\nabla Y_{lm}(\theta,\phi)$, $\mathbf{\Phi}_{lm}(\theta,\phi) = \mathbf{r} \times \mathbf{\Psi}_{lm}(\theta,\phi)$ being

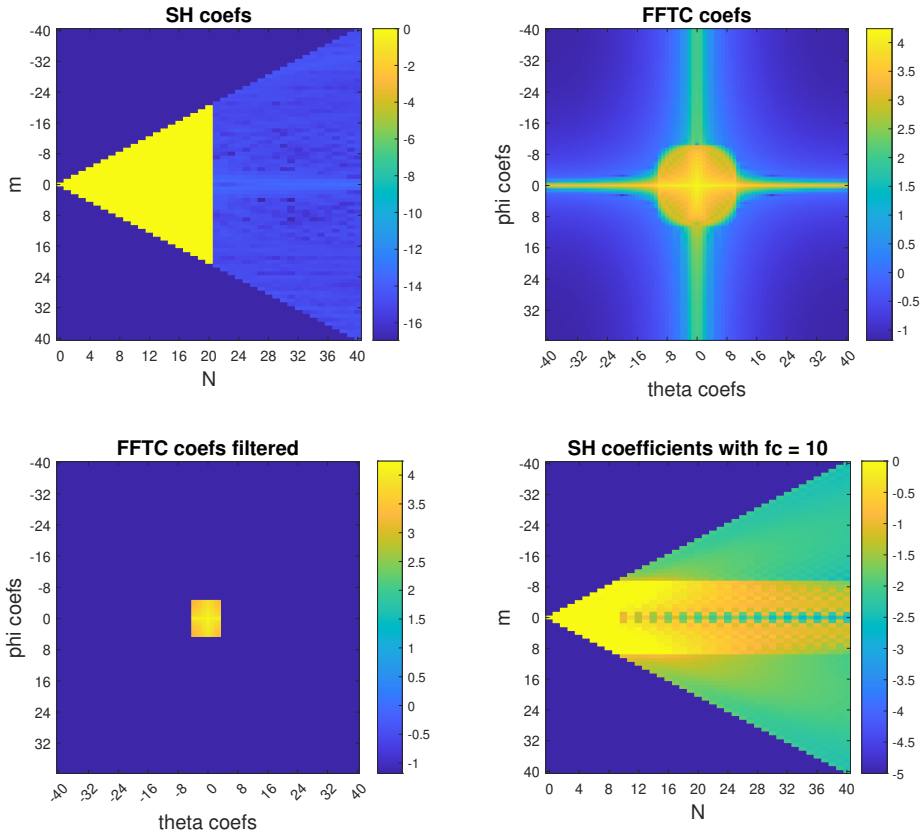

Figure 3.3: a. SHT of the original function, b. 2D-DFT of the original function, c. 2D-DFT of the filtered function, d. SHT of the filtered function. The band-limitedness in the DFT domain does not reflect into a band-limited SHT spectrum.

$\hat{r}$ the unitary vector along the radial direction and $\mathbf{r}$ the position vector of the point with spherical coordinates r, θ, ϕ; and a_{lm}, b_{lm}, c_{lm} are the corresponding coefficients. By using vector spherical harmonics, we can efficiently represent and analyze vector fields, preserving their physical properties and facilitating operations such as differentiation, integration, filtering and convolution in the spectral domain.

3.3 Non uniform discretization schemes

3.3.1 Non-Uniform Discrete Fourier Transform (NUDFT)

The Non-Uniform Discrete Fourier Transform (NUDFT) generalizes the DFT to handle non-uniform discretization cases, enabling the analysis of data sampled at arbitrary points [61].

The NUDFT of a function $f(x)$ is defined as

$$F(k) = \sum_{n=0}^{N-1} f(x_n) e^{-i2\pi k x_n / T}, \quad k = 0, 1, \ldots, N-1 \tag{3.17}$$

where T is the period of the signal, and x_n are the sample points. The inverse NUDFT is used to reconstruct the signal from its frequency components. It is given by:

$$f(x_n) = \frac{1}{N} \sum_{k=0}^{N-1} F(k) e^{i2\pi k x_n / T}, \quad n = 0, 1, \ldots, N-1 \tag{3.18}$$

One of the main challenges in computing the NUDFT is the increased computational complexity compared to the standard DFT. The lack of uniform structure does not allow the application of the $\mathcal{O}(N \log N)$ FFT algorithm. However, various fast algorithms and approximations, such as the Non-Uniform Fast Fourier Transform (NUFFT), have been developed to mitigate this issue and provide efficient computations for non-uniform data.

NUFFT leverages interpolation techniques to approximate the non-uniform data by mapping it onto a uniform grid, where the FFT can then be applied efficiently. This is generally achieved through a process called "gridding". The steps involve:

- Gridding: The non-uniformly spaced data points are convolved with a carefully chosen kernel to interpolate them onto a uniform grid.
- FFT Application: The standard FFT is applied to the gridded data.
- De-Gridding: The results are then interpolated back to the original non-uniform grid to obtain the desired frequency components.

This approach reduces the complexity of the transform significantly. With the use of efficient gridding and de-gridding techniques, the NUFFT can achieve a computational complexity close to $O(N \log N)$, making it nearly as efficient as the FFT while handling the challenges posed by non-uniform sampling. Accuracy in the NUFFT is a critical aspect that hinges on the choice of the interpolation kernel and the parameters used in the gridding process. Commonly used kernels, such as Gaussian or Kaiser-Bessel functions, are selected for their favorable properties in minimizing interpolation errors and spectral leakage. The accuracy of the NUFFT

can be controlled by adjusting parameters like the kernel width and the oversampling factor; however, higher accuracy requires more computational resources. The best trade off between efficiency and precision is application-dependent.

3.3.2 Basis function choice

When dealing with non-uniform schemes, the employed basis functions play a crucial role. More in detail, the accuracy performances of fast schemes may be compromised by the error introduced by numerically integrating on irregular domains. The formulation in 3.17, in fact, relates to function samples, which implies using Dirac delta as source and test functions. This is however an inconvenient choice in practice, because as discussed in 1.5.3 it is not straightforward for the application of differential operators.

Upon uniform discretization, the usage of hat functions introduces only a little error (constant for each harmonic) on the magnitude of the interpolated functions, preserving correctly its phase. This means the singular vector of the DFT are uncorrupted, and a marginal error is present on its singular values. This error is compensated when the adjoint transform is applied. When we move to non-uniform discretization, however, we end up with spurious errors on both phase and magnitude, varying on each point according to the mesh segment length. This reflects in a corruption of the singular vectors of the transformation, which introduce errors not compensated by the adjoint operator.

3.3.3 Numerical analysis and research directions

A campaign of numerical measure of the errors associated with the usage of hat functions has been carried out, considering different forms of irregularity in the discretization. Namely, we considered discretizations derived by the uniform ones by removing a (or multiple) point(s), as well as cases where the point position is moved by a little amount around their initial position. We also measured the effect of a completely random discretization. Fig. 3.4 shows the decay of the order on the discretized projector from hat functions to exponentials, evaluated as

$$err = \frac{|\mathbf{G}_{e,e} - \mathbf{G}_{\lambda,e}\mathbf{G}_{\lambda,\lambda}^{-1}\mathbf{G}_{e,\lambda}|}{|\mathbf{G}_{e,e}|}\,, \tag{3.19}$$

with respect to the number of discretization points. The result is a decay of polynomial type, of order 4. Fig. 3.5 shows how bad is the effect of removing consecutive points from the mesh, introducing irregularity. For certain discretization ranges, it is enough to remove two consecutive points to obtain a decay in accuracy equivalent to halving the discretization density while keeping a uniform mesh.

For comparison, it is worth noticing that, with NUDFT, on such meshes accuracy to nearly machine precision has always been achieved, even if numerical results are not reported. We made some attempts to circumvent the problem. At first, we tried to develop algorithms to correct the phase of the interpolation, thus preserving the singular vectors. However, the needed phase correction not only depends on the geometry, but also on the specific function to be interpolated. Then, we also tried the introduction of a new basis function made of a series of delta with amplitudes shaped as a hat functions, but chosen in such a way to be orthogonal one against the other. Results were poor also in this case. The only effective strategy we tested was the usage of interpolation strategies, to sample the function on reconstructed uniform grids, but this approach is unpractical: it does not allow for a real non-uniform grid simulation, which is the final goal of such studies. The topic definitely remains an open research field.

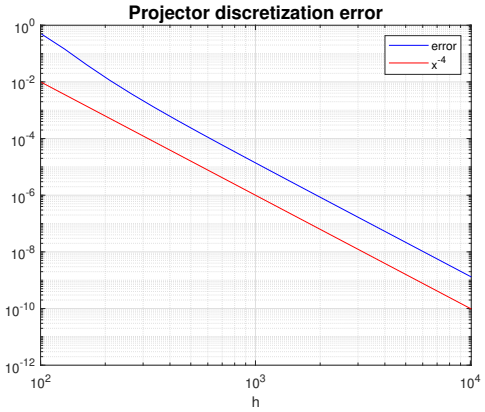

Figure 3.4: Relative error on the discretized projector $\mathbf{G}_{\lambda,e}\mathbf{G}_{\lambda,\lambda}^{-1}\mathbf{G}_{e,\lambda}$ with respect to the discretization density. The error decays with polynomial order as $\mathcal{O}(x^{-4})$.

3.3.4 Non-uniform Fast Vector Spherical Harmonic Transforms

FaVeST (Fast Vector Spherical Harmonic Transforms) [62] represents the state-of-the-art in the efficient computation of spherical harmonic transforms, extending capabilities to both uniform and non-uniform discretizations. The forward FaVeST algorithm computes the vector spherical harmonics with a computational cost proportional to $N \log \sqrt{N}$ for N evaluation points. Similarly, the adjoint FaVeST, which evaluates a linear combination of vector spherical harmonics up to a degree of $\sqrt{M}$ for M evaluation points, also achieves $M \log \sqrt{M}$ complexity. These algorithms offer significant improvements in efficiency compared to traditional methods, which typically have $O(N^2)$ complexity.

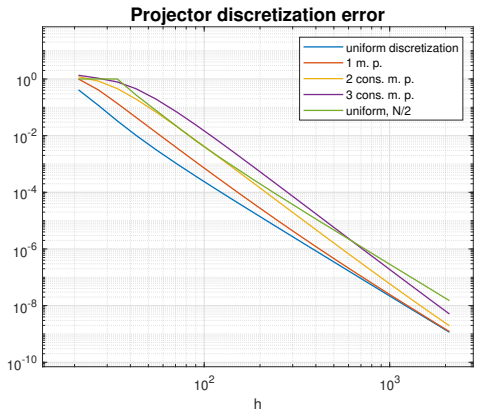

Figure 3.5: Relative error on the discretized projector $\mathbf{G}_{\lambda,e}\mathbf{G}_{\lambda,\lambda}^{-1}\mathbf{G}_{e,\lambda}$ with respect to the discretization density, and in presence of missing consecutive discretization points. It is noticeable how the lack of only two consecutive points produces an overall error comparable to a uniform discretization with the number of discretization points halved.

FaVeST leverages the fast algorithms for scalar spherical harmonic transforms, integrating them with vector spherical harmonics using Clebsch–Gordan coefficients from quantum mechanics. This approach allows the decomposition of vector spherical harmonics into manageable components, facilitating the use of efficient scalar FFT techniques. FaVeST is hierarchically grounded into the other algorithms introduced in this chapter:

- **Fast Fourier Transform (FFT):** Provides the efficient computation of the discrete Fourier transform.
- **Non-Uniform Fast Fourier Transform (NUFFT):** Extends FFT capabilities to non-uniformly sampled data.
- **Fast Scalar Spherical Harmonic Transform (Fast SHT):** Adapts FFT techniques to spherical domains for scalar fields.
- **FaVeST:** Builds on Fast SHT to handle vector fields, incorporating both divergence-free and curl-free components.

By integrating these algorithms, FaVeST achieves high computational efficiency and accuracy, making it a powerful tool for analyzing vector fields on spherical surfaces.

3.4 Generalization to non circular geometries

When dealing with non-circular geometries, the symmetry of the geometry no longer leads to operators whose eigenvectors or singular vectors are exponentials (2D) or spherical harmonics (3D). However, it is noteworthy how the high-frequency part of the operator singular vector space still behaves similarly to that for regular geometries. More specifically, for a given non-circular geometry, let $\mathcal{X}$ be the integral operator of interest, $\mathbf{X}$ its discretized counterpart and $\mathbf{U_X S_X V_X^T}$ its singular value decomposition.

At high frequencies, the wavelength λ becomes small compared to the characteristic dimensions of the geometry. Thus, the local behavior of the wave can be approximated by the behavior in a locally regular geometry. We can define a threshold frequency f_t such that for frequencies $f > f_t$, the singular vectors $\mathbf{u}_n$ and $\mathbf{v}_n$ for the non-circular geometry $\mathcal{X}$ are close to those of the circular (or regular) geometry $\mathcal{X}_{\text{reg}}$.

Thus, for $f > f_t$, the differences between the singular vectors of $\mathcal{X}$ and $\mathcal{X}_{\text{reg}}$ become smaller, and the high-frequency part of the operator singular vector space for non-circular geometries behaves more and more that of regular geometries.

3.4.1 Behavior of the Laplacian

The Laplacian, according to its definition in 2.4.1, is not sensitive to the geometry curvature but only to the discretization regularity. Thus, for any uniformly discretized mesh, the discretized Laplacian will be a regular matrix, circulant in the 2D case. This property, together with the monotonic Laplacian spectrum, makes the set of Laplacian singular vectors a suitable choice as ordered basis w.r.t. spacial frequency. On the other side, we expect the integral operators to share the Laplacian singular vectors only above a certain geometry-dependent spatial frequency f_t.

3.4.2 Mapping to regular geometries

Mapping non-regular geometries onto regular ones is a technique for simplifying the analysis and solving integral equations more efficiently. This process involves transforming a complex, irregular domain into a simpler, regular domain where analytical and numerical methods are more straightforward to apply. For the mapping to be effective, it is needed that it preserves the solution accuracy and that both forward and inverse mapping can be applied in linear complexity. Several strategies are commonly employed to achieve this transformation. Here follows a non-exhaustive list of the most relevant ones.

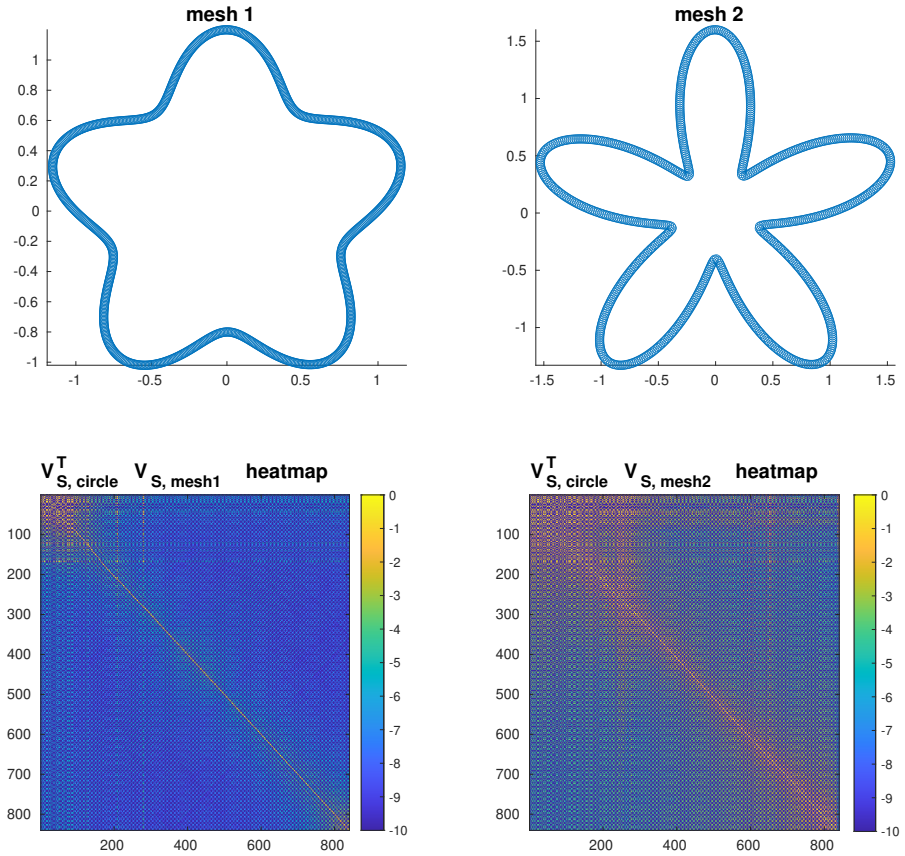

Figure 3.6: Numerical evaluation of the relationship among the singular vectors on the circle and other geometries. the plot technique used here is described in details in appendix B.

Conformal mapping [63, 64] is a mathematical technique that transforms one plane region into another in such a way that angles are preserved. This method is particularly useful in two-dimensional problems where it can be used to map complex geometries onto simpler ones, such as mapping an arbitrary-shaped domain onto a unit circle or rectangle.

Parameterization techniques [57, 65] involve representing the geometry of a domain using a set of parameters. These techniques are particularly useful in three-dimensional problems where surfaces can be described using parametric equations. Common parameterization methods include Bézier and B-Spline Surfaces, used to represent complex surfaces through control points and Non-Uniform Rational

B-Splines, an extension of B-splines that include weights for each control point, allowing for the representation of both standard analytical shapes (like circles and ellipses) and free-form shapes.

Grid and mesh generation techniques [66] involve creating a discretized representation of a complex geometry that approximates a regular domain. These techniques are crucial for finite element and boundary element methods, where the accuracy of the solution depends on the quality of the mesh. Common approaches include structured grids, unstructured grids and Adaptive Mesh Refinement

Domain decomposition methods [67–69] involve breaking down a complex domain into smaller, more manageable subdomains, which can be more regularly shaped. These methods are beneficial for parallel computing and large-scale simulations. Key techniques include Schwarz Methods, an iterative methods that solve subproblems on overlapping subdomains and combine the solutions to form the global solution and Mortar Methods, which use non-overlapping subdomains and employ Lagrange multipliers to ensure continuity across the subdomain interfaces.

Finally, coordinate transformations [70, 71] involve changing the coordinate system to map a non-regular domain onto a regular one. Common transformations include Polar and Spherical Coordinates and Elliptical and Parabolic Coordinates, used for domains that naturally fit these coordinate systems, allowing for a more regular representation.

Chapter 4

Operator filtering based on Modified Green Functions

As already elucidated in section 2.3, operator filtering is an emerging field of research in computational electromagnetic, with Multiplicative Laplacian filters standing as one of the most promising techniques. Operator filtering, relying on quasi-Helmholtz filters, has successfully been used to stabilize the Electric Field Integral Equations (EFIE) for 3D scattering in both the dense-discretization and low frequency regimes and to enhance the compressibility of integral operators for building single-skeleton fast direct solvers.

In this chapter, we introduce a novel way to directly obtain filtered operators by truncating carefully chosen spectral representation of the operators' kernels. This means that the standard BEM discretization of the modified operators will directly yield matrices whose spectra correspond to a filtered version of the spectrum of the discretized original operators, further simplifying the process. The study has been performed in a bi-dimensional setting, on a uniformly discretized non-convex geometry. The principal formulations contained in this chapter has also been published in [72], thus this work can be seen as an extended form of the conference paper, comprehensive of implementation details.

Consider a 2D scatterer modeled by a smooth curve $\gamma \in \mathbb{R}^2$ lying on the xy plane, in a medium with wavenumber k and impedance η, on which impinges an electromagnetic field $(\boldsymbol{E}^i, \boldsymbol{H}^i)$. Let's consider the EFIE problem in TE and TM polarizations, as formulated in 1.106 and 1.108. Using piecewise linear Lagrangian interpolants $\{\phi_i\}$ introduced in 1.132 as both source and test functions, a mesh composed of N segments of uniform length h, and the operators $\mathcal{N}$ and $\mathcal{S}$ introduced

in 1.101 and 1.98, we can write the BEM linear system as

$$\mathbf{S}\mathbf{j}_z = \mathbf{E}_z, \tag{4.1}$$
$$\mathbf{N}\mathbf{j}_t = \mathbf{E}_t \tag{4.2}$$

where

$$[\mathbf{S}]_{ij} = \langle \varphi_i, \mathcal{S}\varphi_j \rangle \,, \tag{4.3}$$
$$[\mathbf{N}]_{ij} = \langle \varphi_i, \mathcal{N}\varphi_j \rangle \,, \tag{4.4}$$
$$\mathbf{E}_t = \left\langle \varphi_i, \frac{\mathrm{i}k}{\eta} E_t \right\rangle, \tag{4.5}$$
$$\mathbf{E}_z = \left\langle \varphi_i, \frac{1}{\eta \mathrm{i}k} E_z \right\rangle \tag{4.6}$$

4.1 Modified Green Function filtering in 2D

The scheme that we present in this work is articulated in three steps: (i) define the filtered Green's function $g^\alpha(\boldsymbol{r}, \boldsymbol{r}')$ where α indicates a filtering parameter (akin to a cutoff frequency) that will depend on the spectral representation chosen, (ii) define the filtered operators $\mathcal{S}^\alpha$ and $\mathcal{N}^\alpha$, and (iii) use the boundary element method to obtain the matrices with the corresponding filtered spectra.

4.1.1 Definition of the filtered Green functions

We introduce two different approaches to filtering, namely a multi-dimensional one based on the Fourier transform (available in both static and dynamic regimes) and a mono-dimensional one that leverages the Mehler–Sonine integral (only for the dynamic case). Note that dimensionality, in this context, does not refere to the geometry of the problem, but to interpretations of the different spectral expansions employed.

Multi-dimensional filters

The first approach to filter $g(\boldsymbol{r}, \boldsymbol{r}')$ we present, imply transforming it into spectral domain in the sense of a multidimensional Fourier expansion, and back-transforming a truncated version obtaining the following modified kernels. In the static case, the resulting formulation reads

$$g_0^\alpha(\boldsymbol{r}, \boldsymbol{r}') = -\frac{1}{2\pi} \log(|\boldsymbol{r} - \boldsymbol{r}'|) - \frac{1}{2\pi} \int_{s=\alpha}^{+\infty} \frac{J_0(s|\boldsymbol{r} - \boldsymbol{r}'|)}{s} \, \mathrm{d}s \,, \tag{4.7}$$

and in the dynamic case

$$g^{\alpha}(\boldsymbol{r},\boldsymbol{r}') = -\frac{\mathrm{i}}{4}H_0^{(2)}(k|\boldsymbol{r}-\boldsymbol{r}'|) - \frac{1}{2\pi}\int_{s=\alpha}^{+\infty}\frac{J_0(s|\boldsymbol{r}-\boldsymbol{r}'|)s}{s^2-k^2}\,\mathrm{d}s \tag{4.8}$$

respectively, where $\alpha > k$, J_0 is the 0^{th} order Bessel function of the first kind and $H_0^{(2)}$ is the 0^{th} order Hankel function of the second kind. Implementation details will be discussed later.

Mono-dimensional filter

Another possible spectral expansion of $g(\boldsymbol{r},\boldsymbol{r}')$ can be obtained for the dynamic case leveraging Mehler–Sonine integrals, obtaining

$$Y_0(x) = -\frac{2}{\pi}\int_1^{\infty}\frac{\cos(xt)}{\sqrt{(t^2-1)}}dt \tag{4.9}$$

where Y_0 is the 0^{th} order Bessel function of the second kind. Using the identity $H_0^{(2)}(x) = J_0(x) - \mathrm{i}Y_0(x)$, recalling the Green's Function definition, and truncating $Y_0(x)$, we obtain

$$g^{\alpha}(\boldsymbol{r}-\boldsymbol{r}') = -\frac{\mathrm{i}}{4}J_0(k|\boldsymbol{r}-\boldsymbol{r}'|) - \frac{1}{2\pi}\int_{t=1}^{\alpha/k}\frac{\cos(k|\boldsymbol{r}-\boldsymbol{r}'|t)}{\sqrt{t^2-1}}\,\mathrm{d}t\,. \tag{4.10}$$

This formulation, however, is challenging to compute. Implementation details will be discussed later.

4.1.2 Definition of the filtered operators

Given the filtered Green functions hereby defined, we can now build the filtered operators of interest, which reads

$$(\mathcal{S}^{\alpha}j_z)(\boldsymbol{r}) \coloneqq \int_{\gamma} g^{\alpha}(\boldsymbol{r},\boldsymbol{r}')j_z(\boldsymbol{r}')\,\mathrm{d}r'\,, \tag{4.11}$$

$$(\mathcal{N}^{\alpha}j_t)(\boldsymbol{r}) \coloneqq -\frac{\partial}{\partial n}\int_{\gamma}\frac{\partial}{\partial n'}g^{\alpha}(\boldsymbol{r},\boldsymbol{r}')j_t(\boldsymbol{r}')\,\mathrm{d}\boldsymbol{r}'\,. \tag{4.12}$$

Note that also operators $\mathcal{D}$ and $\mathcal{D}*$ can be built in an analogous manner

4.1.3 Application of BEM and filtered matrices

Now, it is straightforward to compute the discretized counterparts of the filtered operators as

$$[\mathbf{S}^\alpha]_{ij} = \langle \varphi_i, \mathcal{S}^\alpha \varphi_j \rangle \,, \tag{4.13}$$

$$[\mathbf{N}^\alpha]_{ij} = \langle \varphi_i, \mathcal{N}^\alpha \varphi_j \rangle \,. \tag{4.14}$$

$$\tag{4.15}$$

This step is crucial, since here we expect the spectral properties of the continuous operators to translate into spectral properties of the matrices, which are the ones of interest by a computational point of view.

4.2 Implementation details for stability

All the filtered Green function formulations proposed so far pose some challenges on the computational side, mainly in terms of stability. In this section, stable formulation and implementation details are provided.

Multi-dimensional filters

For the implementation of (4.8), the computation is split in two parts: the singular part is handled by Maclaurin expansion; whereas the asymptotic regime is handled by a recursive extraction of terms which leads to a series of rational coefficients, that are tabulated for runtime. More in detail, to enhace performances, it becomes convenient to introduce a third regime, for medium size argument, which is handled by Taylor expansion around suitably choosen points: in this way, Maclaurin expansion order can be reduced without compromising solution's accuracy.

Starting from the static case, Eq. (4.7) can be rewritten

$$\widetilde{g}(r,S) = \frac{1}{2\pi}\left(\gamma + \log(\frac{S}{2}) + \sum_{k=1}^{+\infty} \frac{(-1)^k (Sr)^{2k}}{2k(k!)^2 4^k}\right) \tag{4.16}$$

Since the log is already computed accurately, it only remains to compute accurately (see NIST 10.22.39)

$$f(x) = \sum_{k=1}^{+\infty} \frac{(-1)^k x^{2k}}{2k(k!)^2 4^k} = -\gamma - \log(\frac{x}{2}) - \int_x^{+\infty} \frac{J_0(t)}{t} dt \tag{4.17}$$

For small x, we compute the truncated series directly.

$$f(x) = \sum_{k=1}^{n} \frac{(-1)^k x^{2k}}{2k(k!)^2 4^k} + O(x^{2n+2}) \tag{4.18}$$

To increase the precision, the terms in the sum are accumulated from large k to smaller k
For large x, We use the expansion

$$\int_x^{+\infty} \frac{J_0(t)}{t} dt \quad = \sqrt{\frac{2}{\pi}} \sum_{k=0}^{n} \left(s_k \frac{\sin(t-\pi/4)}{x^{2k+3/2}} + c_k \frac{\cos(t-\pi/4)}{x^{2k+5/2}} \right) + O\left(\frac{1}{x^{2n+7/2}} \right) \tag{4.19}$$

where

$$s_0 = -1 \tag{4.20}$$

$$s_m = (2m + \frac{1}{2}) c_{m-1} - \frac{(-1)^m (4m)!^2}{32^{2m} (2m)!^3} \tag{4.21}$$

$$c_m = \frac{(-1)^m (4m+2)!^2}{32^{2m+1} (2m+1)!^3} - (2m + \frac{3}{2}) s_m \tag{4.22}$$

These rational coefficients s_m and c_m are tabulated for runtime.
Unfortunately, the accuracy of the two previous expressions decreases as small x increases or large x decreases so that there is a range where none of the previous formulas delivers an accurate result. In this range of medium x that do the junction between the two other forms, we use a taylor expansion around points $x_0 = x - h$

$$\begin{aligned} \int_x^{+\infty} \frac{J_0(t)}{t} dt &= \int_{x_0+h}^{+\infty} \frac{J_0(t)}{t} dt \\ &= \int_{x_0}^{+\infty} \frac{J_0(t)}{t} dt + \sum_{k=1}^{n} \frac{1}{k!} \frac{\partial^{k-1}}{\partial t^{k-1}} \left(\frac{J_0(t)}{t} \right) |_{t=x_0} h^k + O(h^{n+1}) \end{aligned} \tag{4.23}$$

The coefficients for several points x_0 are computed with high precision arithmetic and tabulated for the runtime.

Using the 3 techniques in different regimes, the machine precision accuracy can be achieved for any values of the parameters r and S.

For the dynamic case, the technique is the same: in the asymptotic regime, we use the following expansion of J_0 and integrate by part to extract terms

$$J_0(t) = \sqrt{\frac{2}{\pi}} \sum_{k=0}^{n} \left(a_k \frac{\cos(t-\pi/4)}{t^{2k+1/2}} + b_k \frac{\sin(t-\pi/4)}{t^{2k+3/2}} \right) + O\left(\frac{1}{t^{2n+5/2}} \right) \tag{4.24}$$

$$a_k = \frac{(-1)^k (4k)!^2}{32^{2k} (2k)!^3}, b_k = \frac{(-1)^k (4k+2)!^2}{32^{2k+1} (2k+1)!^3}$$

After few integrations by part it is easy to see that we can look for a general term

in the form

$$\begin{aligned}\int_{t=A}^{+\infty}\frac{J_0(t)t}{t^2-B^2}dt &= \sqrt{\frac{2}{\pi}}\sin(A-\pi/4)\sum_{k=0}^{m-1}\frac{1}{(A^2-B^2)^{2k+1}A^{2k-1/2}}\sum_{i=0}^{2k}s_{k,i}(A^2-B^2)^iA^{2(2k-i)}\\ &+\sqrt{\frac{2}{\pi}}\cos(A-\pi/4)\sum_{k=0}^{m-1}\frac{1}{(A^2-B^2)^{2k+2}A^{2k+1/2}}\sum_{i=0}^{2k+1}c_{k,i}(A^2-B^2)^iA^{2(2k+1-i)}\\ &+\sqrt{\frac{2}{\pi}}\int_{t=A}^{+\infty}\frac{\cos(t-\pi/4)}{(t^2-B^2)^{2m+1}t^{2m-1/2}}\sum_{i=0}^{2m}r_{m,i}(t^2-B^2)^it^{2(2m-i)}dt\\ &+\sqrt{\frac{2}{\pi}}\int_{t=A}^{+\infty}\left(\sum_{k=m+1}^{n}\frac{a_k\cos(t-\pi/4)}{(t^2-B^2)t^{2k-1/2}}+\sum_{k=m}^{n}\frac{b_k\sin(t-\pi/4)}{(t^2-B^2)t^{2k+1/2}}+O\left(...\right)\right)dt\end{aligned} \tag{4.25}$$

After two integration by part, we get the recurrence formulas for the coefficients

$$r_{0,0} = a_0 \tag{4.26}$$
$$s_{m,i} = -r_{m,i} \tag{4.27}$$
$$c_{m,i} = (2+4m-2i)r_{m,i} + (2i-2m-5/2)r_{m,i-1} \tag{4.28}$$
$$c_{m,2m+1} = b_m + (2m-1/2)r_{m,2m} \tag{4.29}$$
$$r_{m+1,i} = (2i-4m-4)c_{m,i} + (2m-2i+7/2)c_{m,i-1} \tag{4.30}$$
$$r_{m+1,2m+2} = a_{m+1} + (-2m-1/2)c_{m,2m+1} \tag{4.31}$$

i.e. after substitution,

$$s_{0,0} = -1 \tag{4.32}$$
$$c_{m,i} = (-2-4m+2i)s_{m,i} + (-2i+2m+5/2)s_{m,i-1}, i \in [0,2m](s_{m,-1}=0) \tag{4.33}$$
$$c_{m,2m+1} = \frac{(-1)^m(4m+2)!^2}{32^{2m+1}(2m+1)!^3} + (-2m+1/2)s_{m,2m} \tag{4.34}$$
$$s_{m,i} = (-2i+4m)c_{m-1,i} + (-2m+2i-3/2)c_{m-1,i-1}, i \in [0,2m-1](c_{m-1,-1}=0) \tag{4.35}$$
$$s_{m,2m} = -\frac{(-1)^m(4m)!^2}{32^{2m}(2m)!^3} + (2m-3/2)c_{m-1,2m-1} \tag{4.36}$$

For small argument, the goal is to reuse the static filter integral I_1 where (here $S = \alpha R$)

$$I_n = \int_S^{+\infty}\frac{J_0(t)}{t^n}dt \tag{4.37}$$

The integral that we want to compute is

$$\int_S^{+\infty} \frac{J_0(t)t}{t^2 - x^2} dt = I_1 + x^2 \int_S^{+\infty} \frac{J_0(t)}{t(t^2 - x^2)} dt \tag{4.38}$$

But we can continue recursively, and eventually we get

$$\int_S^{+\infty} \frac{J_0(t)t}{t^2 - x^2} dt = \sum_{n=0}^{N-1} x^{2n} I_{2n+1} + x^{2N+1} \int_S^{+\infty} \frac{J_0(t)}{t^{2N}(t^2 - x^2)} dt \tag{4.39}$$

Also, we have

$$I_{n+2} = -\frac{1}{(n+1)^2} I_n - \frac{1}{(n+1)^2} \frac{J_1(S)}{S^n} + \frac{1}{n+1} \frac{J_0(S)}{S^{n+1}} \tag{4.40}$$

Mono-dimensional filter

Regarding Eq. 4.10, here a step-by-step procedure to compute the oscillatory part $(2, \alpha/k)$ of the integral is described in details. Let's start by defining

$$f(t) \coloneqq \frac{1}{\sqrt{t^2 - 1}}. \tag{4.41}$$

Now, rewrite the integral in (4.10) as

$$I_k^{c1,c2} = \Re \left(\int_{c1}^{c2} \mathrm{e}^{\mathrm{i}kt} f(t) dt \right). \tag{4.42}$$

We can define a change of variable which maps $(-1, 1)$ into $(c1, c2)$ carried out by a function

$$g(t) \coloneqq (t+1) \frac{c2 - c1}{2} + c1\,, \tag{4.43}$$

end then expand $f \circ g$ as a linear combination of Legendre polynomials P_n

$$f(g(x)) = \sum_{n=0}^{\infty} a_n P_n(x)\,, a_n = \frac{2n+1}{2} \int_{-1}^{1} f(g(x)) P_n(x)\, \mathrm{d}x. \tag{4.44}$$

Now, define $k' = \frac{c2-c1}{2} k$ and rewrite (4.42) as

$$I_k^{c1,c2} = \Re \left(\frac{c2 - c1}{2} \mathrm{e}^{\mathrm{i}(k' + kc1)} \sum_{n=0}^{\infty} a_n \int_{-1}^{1} \mathrm{e}^{\mathrm{i}k't} P_n(t) dt \right). \tag{4.45}$$

Using the following identity from [73]

$$\int_{-1}^{1} P_n(t) \mathrm{e}^{\mathrm{i}kt} dt = (\mathrm{i})^n \sqrt{\frac{2\pi}{k}} J_{n+\frac{1}{2}}(k)\,, \tag{4.46}$$

we finally obtain

$$I_k^{c1,c2} = \Re\left(\frac{c2-c1}{2}\mathrm{e}^{\mathrm{i}(k'+kc1)}\sum_{n=0}^{\infty} a_n(\mathrm{i})^n\sqrt{\frac{2\pi}{k'}}J_{n+\frac{1}{2}}(k')\right) \tag{4.47}$$

which is computable up to arbitrary precision.

In the interval (1,2) a different expansion is used: by integration by part of Eq. (4.42), we obtain

$$I_k^{c1,c2} = \left[\cos(kt)\ln\left(t+\sqrt{t^2-1}\right)\right]_{t=c1}^{c2} + k\int_{c1}^{c2}\sin(kt)\ln\left(t+\sqrt{t^2-1}\right)dt \tag{4.48}$$

and the integral on the right hand side is computed using the Legendre expansion procedure. Because $\ln\left(t+\sqrt{t^2-1}\right)$ is not singular in 1, the number of terms of the expansion is low, and the approach is efficient and accurate.

4.3 Numerical results

Let γ be the scatterer depicted in Fig. 4.1, with maximum dimensions around 2 m. The frequency is set to 1 GHz with a mesh size of $h = \lambda/30$, leading to approximately 830 mesh elements.

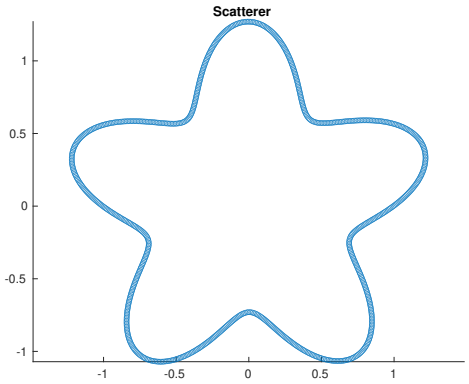

Figure 4.1: Scatterer used as reference for the following numerical results

To understand the following plots, some considerations made through this thesis have to be gathered and taken into account:

- As introduced in section 3.4.1, the singular vectors of the Laplacian provide a meaningful ordering basis, because they can be interpreted as spatial frequency harmonics,

- However, according to 3.4.1, we cannot expect Laplacian singular vectors to be equal to the operator for non-circular geometries,
- Section 3.4 explains how we expect the singular vectors to become increasingly similar for higher spatial frequencies, since the local behavior of the geometry becomes indistinguishable above its characteristic spatial frequency,
- Finally, above the filtering threshold, we cannot expect that any ordering can be made due to the clustering of singular vector in the null-space, according to Davis-Khan theorem introduced in section 2.3.1.

Thus, to represent in a meaningful way the spectrum of our discretized operators and filtered counterparts, we followed this procedure:

1. perform SVD on all the matrices we want to represent, and on the Laplacian,
2. compute the permutation matrix that makes the singular vectors of the matrix of interest most similar to the Laplacian ones. The concept of similarity can be defined with any vector norm, we used energy norm of the convolution among the two vectors,
3. apply this permutation matrix to the singular values of the matrix of interest,
4. plot the resulting spectrum in logarithmic scale.

It is now possible to analyze the following numerical results. In the beginning of the spectrum we expect to have some misalignment among the singular values, because the ordering according to the Laplacian is not reliable for low spectral frequencies. In the same way we expect to have ordering problems approaching the null-space, where Davis-Kahan theorem effect becomes evident. The ordering is by the way reliable in the middle frequencies, around the cutoff frequency of the filter.

Fig. 4.4 shows the application of the multiplicative Laplacian filters introduced in 2.4.2 to the discretized single layer operator $\mathbf{S}$. As clearly visible, the filter of order 32 is highly effective, with a decay to machine precision in about a hundred of singular values.

The aforementioned singular value behavior is also clearly visible when looking at the projection of the filtered operator singular vectors on the Laplacian ones, as shown in Fig. 4.2 for the discretized operator $\mathbf{S}$ under Butterworth filtering. For more details about this kind of plot, the reader can refer to Appendix B.

An alternative technique to display the spectra, which solves the low-frequency ordering issue, is to order the singular values of the filtered operator with respect to the original operator ones. An example of such a plot is reported in Fig. 4.3, where the original operator spectrum is well-ordered by definition [37], but as we can see there are bigger issues when it comes to the ordering in the null-space region.

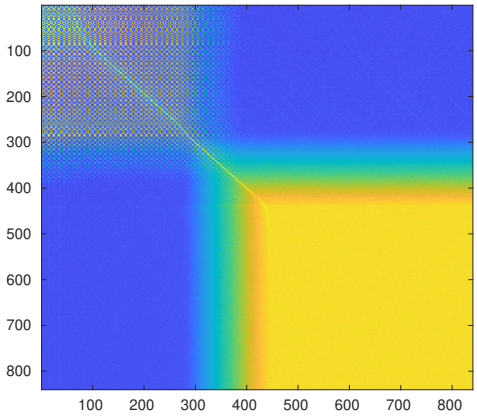

Figure 4.2: singular vector projection of $\mathbf{S}_n$ with Butterworth approximation of order 32 vs Laplace-Beltrami singular vectors. The upper left corner shows the interdependence at low frequency, the diagonal part in the middle is the region where the ordering is effective and the bottom right region corresponds to the filtered operator nullspace.

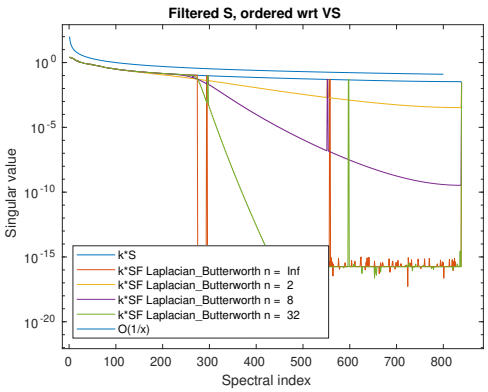

Figure 4.3: Application of Butterworth filtering (Eq. 2.55) to operator **S**. Singular values ordered by the singular vectors of the unfiltered **S** operator

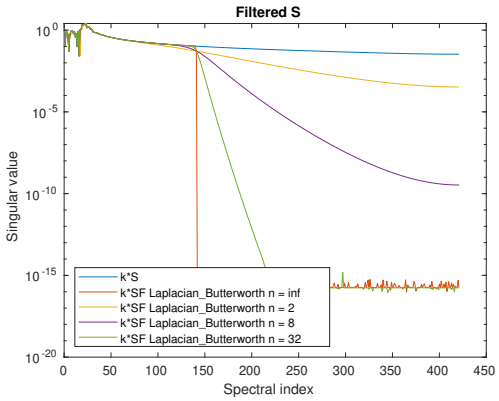

Figure 4.4: Application of Butterworth filtering (Eq. 2.55) to operator **S**. Singular values ordered by the singular vectors of the Laplace-Beltrami operator

Fig. 4.5 shows the effectiveness of the modified green function static formulation (4.7) on the discretized single layer operator **S** in static. In blue, the original operator's spectra, in red its filtered incarnation one. Fig. 4.6 show the performance of (4.8) and (4.10) on the same operator in the dynamic case. We finally show the

effectiveness of the filtering procedure in the Calderón precontitioned TE-EFIE [32]

$$\mathbf{G}^{-1}\mathbf{S}\mathbf{G}^{-1}\mathbf{N}\mathbf{j}_t = \mathbf{G}^{-1}\mathbf{S}\mathbf{G}^{-1}\mathbf{e}_t\,, \tag{4.49}$$

where $[\mathbf{G}]_{ij} \coloneqq \langle \varphi_i, \varphi_j \rangle$. In Figure 4.7, in particular, we show the singular values of $\mathbf{G}^{-1}\mathbf{S}\mathbf{G}^{-1}\mathbf{N}$ and singular values of $\mathbf{G}^{-1}\mathbf{S}^{\alpha}\mathbf{G}^{-1}\mathbf{N}$ where $\mathbf{S}^{\alpha}$ is computed using (4.8) and (4.10), ordered by the singular vectors of the Laplace-Beltrami operator.

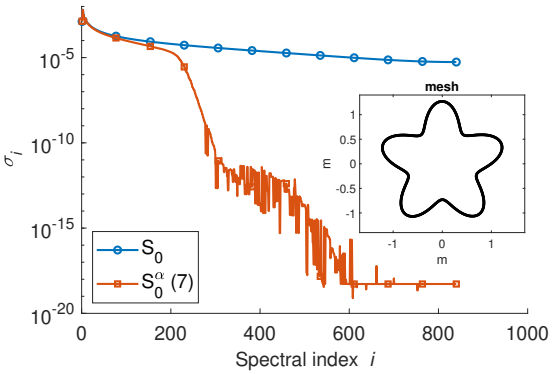

Figure 4.5: Singular values of $\mathbf{S}_0$ and singular values of $\mathbf{S}_0^{\alpha}$ using (4.7), ordered by the singular vectors of the Laplace-Beltrami operator, and reference mesh.

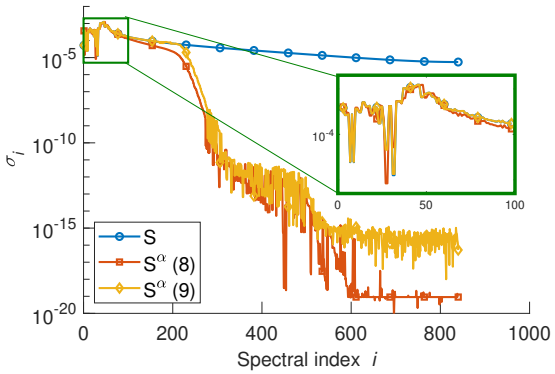

Figure 4.6: Singular values of $\mathbf{S}$ and singular values $\mathbf{S}^{\alpha}$ using (4.8) and (4.10), ordered by the singular vectors of the Laplace-Beltrami operator.

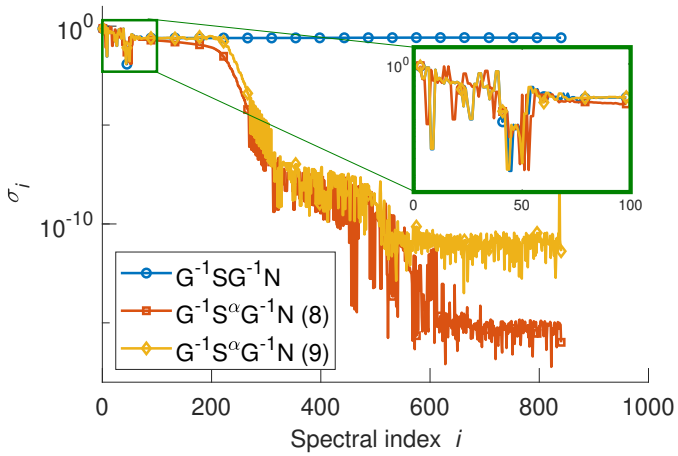

Figure 4.7: Singular values of $\mathbf{G}^{-1}\mathbf{S}\mathbf{G}^{-1}\mathbf{N}$ and singular values of $\mathbf{G}^{-1}\mathbf{S}^{\alpha}\mathbf{G}^{-1}\mathbf{N}$ where $\mathbf{S}^{\alpha}$ is computed using (4.8) and (4.10), ordered by the singular vectors of the Laplace-Beltrami operator.

Chapter 5

Conclusions and future work

In this work, the Laplacian multiplicative filters and Modified Green Function Filters, recently introduced in [38] and [72] are widely discussed, and new implementation details and stability considerations for the Modifies Green Function filters in 2D are introduced. A comprehensive analysis of the effect of different discretization and basis function choices has been carried out, highlighting the reasons behind the effectiveness of fast harmonic transforms on circular and spherical domains, under uniform and non-uniform discretizations. Some investigations have also been carried out on the relationship among Spherical Harmonic Transform and bi-dimensional Fourier Transform, in order to better establish the boundaries of the interchangeability among the two proposed in [58]. These topics are preceded by an extensive introduction, that goes from the well-known Maxwell equations to the more complex concepts tackled in this work without any discontinuity, with a deep focus on the Boundary Element Method and families of Fast Solvers. A great amount of references are also provided for the reader interested in further investigations.

The Modified Green Function filters are here introduced for the bi-dimensional setting, but it is straightforward to imagine the existence of 3D counterparts. These 3D filters could be of great practical interest, since 3D simulations are much more effective for real world applications.

Appendix A

Linear Algebra Primer

Matrix Norms

Frobenius Norm: Defined as

$$\|A\|_F = \sqrt{\sum_{i=1}^{m}\sum_{j=1}^{n}|a_{ij}|^2}$$

This norm considers all elements of matrix A and is useful for various matrix operations.
Euclidean Norm (2-norm): Defined as the largest singular value of A,

$$\|A\|_2 = \sigma_{\max}(A)$$

This norm is critical for understanding the behavior of A under transformation.

Matrix Transformations

Transpose: $(A^T)_{ij} = A_{ji}$. It reflects the matrix over its main diagonal.
Hermitian (Conjugate Transpose): $(A^*)_{ij} = \overline{A}_{ji}$. Essential for complex matrices, where the conjugate transpose is used.

Matrix Definitions

Symmetric Matrix: $A^T = A$. Important for properties like real eigenvalues.
Positive Definite Matrix: $x^T Ax > 0, \forall x \neq 0$. Such matrices have positive eigenvalues, which implies stability in various systems. **Circulant matrix**: A

circulant matrix A is of the form

$$A = \begin{bmatrix} a_0 & a_{N-1} & \cdots & a_1 \\ a_1 & a_0 & \cdots & a_2 \\ \vdots & \vdots & \ddots & \vdots \\ a_{N-1} & a_{N-2} & \cdots & a_0 \end{bmatrix}$$

.

Singular Value Decomposition (SVD) and Eigen Decomposition (EigD)

SVD: $A = U\Sigma V^*$ where U and V are unitary, and Σ is diagonal.
EigD: $A = V\Lambda V^{-1}$ where Λ is diagonal and V is the matrix of eigenvectors.
Both decompositions provides diagonalization of the original matrix, and the diagonal matrices are often refered to as matrix spectrum. Singular values of A are the absolute values of the eigenvalues of $\sqrt{A^*A}$. This relationship bridges the gap between geometric and algebraic properties of A.

Projector

A matrix P is a projector if $P^2 = P$. It maps vectors onto a subspace defined by P.
Orthogonal Projector: $P = A(A^TA)^{-1}A^T$ projects onto the column space of A orthogonally.

Condition Number

$$\kappa(A) = \|A\|\|A^{-1}\|$$

Measures the sensitivity of matrix operations to perturbations. High condition numbers indicate potential numerical instability.

Gershgorin Circle Theorem

Each eigenvalue of A lies within at least one Gershgorin circle, centered at a_{ii} with radius $\sum_{j\neq i} |a_{ij}|$. This theorem provides a way to estimate the location of eigenvalues.

Moore-Penrose Pseudoinverse

For matrix A, the pseudo-inverse A^+ satisfies:

$$AA^+A = A, \quad A^+AA^+ = A^+, \quad (AA^+)^T = AA^+, \quad (A^+A)^T = A^+A$$

Useful for solving systems of equations that are not necessarily invertible.

Complexity of Naive Matrix Operations

Multiplication: $O(n^3)$, Inversion: $O(n^3)$
Matrix-Vector Product: $O(n^2)$
These operations form the computational foundation of many algorithms in numerical linear algebra.

Bound among Condition Number and Linear System Solution Accuracy

For $Ax = b$, if δA and δb are perturbations, then:

$$\frac{\|\delta x\|}{\|x\|} \leq \kappa(A) \left(\frac{\|\delta A\|}{\|A\|} + \frac{\|\delta b\|}{\|b\|} \right)$$

This inequality demonstrates how small changes in A or b can lead to large changes in x, especially when $\kappa(A)$ is large. Remember that the discrete computations always carry a perturbation at least equal to machine precision, i.e. 10^{-16} for double precision arithmetic.

Appendix B

Matrix representation

Most of the topics in computational science involve analyzing properties of numerical matrices. Some of these properties are scalar ones (e.g., the rank or the condition number), other are continuous (e.g., the spectrum) and other relates to the structure (e.g., sparsity, circularity, presence of blocks). This underpin the need for suitable graphical representations, because looking at a huge table of raw numbers is something we human are not really good at. The goal of this section is to introduce the main graphical techniques used in this work to represent matrices, together with their advantages and disadvantages.

Logarithmic color plot

Logarithmic color plot is useful to represent matrices with high dynamic range of values. A first thing that must be noticed is that only the magnitude of the matrix entries is represented: nothing is reported about the phase (i.e., the sign of the entries if they are real numbers). The usage of a colorbar is fundamental, because the color mapping to values depends on the maximum and minimum numerical value in the matrix. When comparing multiple logarithmic color plot, it may also be useful to force the usage of the same dynamic range, to have a coherent color-value mapping. This representation allows to immediately recognize circularity and sparsity, and also the presence of structure, like null spaces or presence of blocks. The example in Fig. B.1 shows the operator $\mathcal{N}_{\in\mathcal{D}}$ introduced in 1.107 discretized on the mesh 4.1. There is a clear maximum on the main diagonal (self-element), and a repetitive (but not circulant) pattern in the rest of the matrix.

In Matlab code, given a matrix $\mathbf{A}$, this can be achieved by

```
imagesc(log10(abs(A)));
colorbar;
```

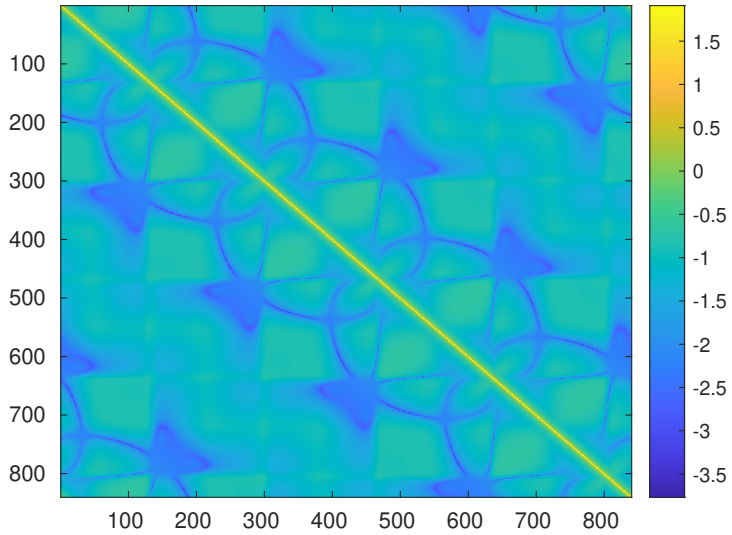

Figure B.1: Operator $\mathcal{N}_{2D}$ discretized on a non-regular mesh

Spectrum plot

A logarithmic plot of the matrix spectrum is the best tool to understand its numerical rank. While the algebraic rank is defined as the number of non-zero eigenvalues (or singular values, if using SVD), the numerical rank depends on the threshold we choose as numerical zero. Plotting the logarithm of the sorted eigenvalues or singular values allows to understand the behavior of the spectrum, if it has a relevant magnitude drop at a certain point, how steep it is and what is the order of magnitude of the values before and after the drop. Furthermore, the dynamic range of the represented values roughly corresponds to the condition number. Example of this kind of plot are 2.2, but also 4.5-4.7 apart for the ordering, which is discussed in section 4.3.

In Matlab code, given a matrix $\mathbf{A}$, this can be achieved by

```
S = svd(A);
semilogy(S);
```

Eigenvector or singular vector projections

Particularly in the context of filtering, the relationships among eigenvectors or singular vectors of couple of matrices are of paramount importance. Given two matrices $\mathbf{A}$ and $\mathbf{B}$, the logarithmic color plot of $\mathbf{V}_\mathbf{A}^H\mathbf{V}_\mathbf{B}$ where $\mathbf{V}_\mathbf{X}$ can either be the

eigenvector, left or right singular vector matrix of $\mathbf{X}$ is an interesting visualization of such a relationship. given the linear independence of both eigenvectors and singular vectors, the similarity of the eigenvector or singular vector set for $\mathbf{A}$ and $\mathbf{B}$ is expressed by the similarity of $\mathbf{V}_\mathbf{A}^H\mathbf{V}_\mathbf{B}$ to the identity matrix. The effect of Davis-Kahan theorem 2.3.1 must be taken into account. Example of such representations are Fig. 2.2 and 4.2.

In Matlab code, given two matrices $\mathbf{A}$ and $\mathbf{B}$, this can be achieved by

```
[ua, sa, va] = svd(A);
[ub, sb, vb] = svd(b);
imagesc(log10(abs(va'*vb)));
colorbar;
```

Bibliography

[1] Constantine A Balanis. *Advanced engineering electromagnetics*. John Wiley & Sons, 2012 (cit. on p. 4).

[2] M Abramovitz and IA Stegun. «Handbook of Mathematical Functions, Vol. 55». In: *National Bureau of Standards Applied Mathematics Series, Washington, DC* (1972) (cit. on p. 16).

[3] Stefan A Sauter and Christoph Schwab. «Boundary element methods». In: *Boundary Element Methods*. Springer, 2010, pp. 183–287 (cit. on p. 19).

[4] David L Colton, Rainer Kress, and Rainer Kress. *Inverse acoustic and electromagnetic scattering theory*. Vol. 93. Springer, 1998 (cit. on p. 19).

[5] Jean-Claude Nédélec. *Acoustic and electromagnetic equations: integral representations for harmonic problems*. Springer Science & Business Media, 2001 (cit. on p. 19).

[6] Jian-Ming Jin. *Theory and computation of electromagnetic fields*. John Wiley & Sons, 2015 (cit. on p. 20).

[7] Roger F Harrington. «The method of moments in electromagnetics». In: *Journal of Electromagnetic waves and Applications* 1.3 (1987), pp. 181–200 (cit. on p. 21).

[8] Sadasiva Rao, Donald Wilton, and Allen Glisson. «Electromagnetic scattering by surfaces of arbitrary shape». In: *IEEE Transactions on antennas and propagation* 30.3 (1982), pp. 409–418 (cit. on p. 25).

[9] Annalisa Buffa and Snorre Christiansen. «A dual finite element complex on the barycentric refinement». In: *Mathematics of Computation* 76.260 (2007), pp. 1743–1769 (cit. on pp. 25, 52).

[10] Francesco P Andriulli, Kristof Cools, Hakan Bagci, Femke Olyslager, Annalisa Buffa, Snorre Christiansen, and Eric Michielssen. «A multiplicative Calderon preconditioner for the electric field integral equation». In: *IEEE Transactions on Antennas and Propagation* 56.8 (2008), pp. 2398–2412 (cit. on p. 26).

[11] Francesco P Andriulli. «Loop-star and loop-tree decompositions: Analysis and efficient algorithms». In: *IEEE Transactions on Antennas and Propagation* 60.5 (2012), pp. 2347–2356 (cit. on pp. 26, 27, 42, 45, 52, 53).

[12] Giuseppe Vecchi. «Loop-star decomposition of basis functions in the discretization of the EFIE». In: *IEEE Transactions on Antennas and Propagation* 47.2 (1999), pp. 339–346 (cit. on pp. 26, 27).

[13] Kristof Cools, Francesco P Andriulli, Femke Olyslager, and Eric Michielssen. «Nullspaces of MFIE and Calderón preconditioned EFIE operators applied to toroidal surfaces». In: *IEEE Transactions on Antennas and Propagation* 57.10 (2009), pp. 3205–3215 (cit. on p. 28).

[14] DRSM Wilton, S Rao, AW Glisson, D Schaubert, O Al-Bundak, and C Butler. «Potential integrals for uniform and linear source distributions on polygonal and polyhedral domains». In: *IEEE Transactions on Antennas and Propagation* 32.3 (1984), pp. 276–281 (cit. on p. 34).

[15] Roberto D Graglia. «On the numerical integration of the linear shape functions times the 3-D Green's function or its gradient on a plane triangle». In: *IEEE transactions on antennas and propagation* 41.10 (1993), pp. 1448–1455 (cit. on p. 34).

[16] Michael A Khayat, Donald R Wilton, and Patrick W Fink. «An improved transformation and optimized sampling scheme for the numerical evaluation of singular and near-singular potentials». In: *IEEE Antennas and Wireless Propagation Letters* 7 (2008), pp. 377–380 (cit. on p. 36).

[17] Michael A Khayat and Donald R Wilton. «Numerical evaluation of singular and near-singular potential integrals». In: *IEEE transactions on antennas and propagation* 53.10 (2005), pp. 3180–3190 (cit. on p. 36).

[18] Michael G Duffy. «Quadrature over a pyramid or cube of integrands with a singularity at a vertex». In: *SIAM journal on Numerical Analysis* 19.6 (1982), pp. 1260–1262 (cit. on p. 36).

[19] Luca Rossi and Peter J Cullen. «On the fully numerical evaluation of the linear-shape function times the 3D Green's function on a plane triangle». In: *IEEE Transactions on Microwave Theory and Techniques* 47.4 (1999), pp. 398–402 (cit. on p. 36).

[20] Zhi Guo Qian, Weng Cho Chew, and Roberto Suaya. «Generalized impedance boundary condition for conductor modeling in surface integral equation». In: *IEEE Transactions on Microwave Theory and Techniques* 55.11 (2007), pp. 2354–2364 (cit. on p. 36).

[21] Swagato Chakraborty and Vikram Jandhyala. «Evaluation of Green's function integrals in conducting media». In: *IEEE transactions on antennas and propagation* 52.12 (2004), pp. 3357–3363 (cit. on p. 36).

[22] Chen Xu, Weiwei Xu, and Kaili Jing. «Fast algorithms for singular value decomposition and the inverse of nearly low-rank matrices». In: *National Science Review* 10.6 (2023), nwad083 (cit. on p. 38).

[23] Mario Bebendorf. «Approximation of boundary element matrices». In: *Numerische Mathematik* 86.4 (2000), pp. 565–589 (cit. on p. 39).

[24] Hongwei Cheng, Zydrunas Gimbutas, Per-Gunnar Martinsson, and Vladimir Rokhlin. «On the compression of low rank matrices». In: *SIAM Journal on Scientific Computing* 26.4 (2005), pp. 1389–1404 (cit. on p. 39).

[25] Leslie Greengard and Vladimir Rokhlin. «A fast algorithm for particle simulations». In: *Journal of computational physics* 73.2 (1987), pp. 325–348 (cit. on p. 39).

[26] Wolfgang Hackbusch. «A sparse matrix arithmetic based on h -matrices. Part I and II». In: *Computing* 62.2 (1999), pp. 89–108 (cit. on p. 39).

[27] Mario Bebendorf. *Hierarchical matrices*. Springer, 2008 (cit. on p. 39).

[28] Jiming Song, Cai-Cheng Lu, and Weng Cho Chew. «Multilevel fast multipole algorithm for electromagnetic scattering by large complex objects». In: *IEEE Transactions on Antennas and Propagation* 45.10 (1997), pp. 1488–1493 (cit. on p. 39).

[29] Kezhong Zhao, Marinos N Vouvakis, and Jin-Fa Lee. «The adaptive cross approximation algorithm for accelerated method of moments computations of EMC problems». In: *IEEE transactions on electromagnetic compatibility* 47.4 (2005), pp. 763–773 (cit. on p. 39).

[30] Anita M Haider and Martin Schanz. «Adaptive cross approximation for BEM in elasticity». In: *Journal of Theoretical and Computational Acoustics* 27.01 (2019), p. 1850060 (cit. on p. 39).

[31] Jonathan Richard Shewchuk et al. «An introduction to the conjugate gradient method without the agonizing pain». In: (1994) (cit. on p. 41).

[32] Simon B Adrian, Alexandre Dely, Davide Consoli, Adrien Merlini, and Francesco P Andriulli. «Electromagnetic integral equations: Insights in conditioning and preconditioning». In: *IEEE Open Journal of Antennas and Propagation* 2 (2021), pp. 1143–1174 (cit. on pp. 41, 85).

[33] Xavier Antoine and Marion Darbas. «An introduction to operator preconditioning for the fast iterative integral equation solution of time-harmonic scattering problems». In: *Multiscale Science and Engineering* 3 (2021), pp. 1–35 (cit. on p. 41).

[34] Francesco P Andriulli, Anita Tabacco, and Giuseppe Vecchi. «Solving the EFIE at low frequencies with a conditioning that grows only logarithmically with the number of unknowns». In: *IEEE transactions on antennas and propagation* 58.5 (2010), pp. 1614–1624 (cit. on pp. 42, 44).

[35] DR Wilton. «Topological consideration in surface patch and volume cell modeling of electromagnetic scatterers». In: *Proc. URSI Int. Symp. Electromagn. Theory*. 1983, pp. 65–68 (cit. on p. 42).

[36] Carl D Meyer. *Matrix analysis and applied linear algebra*. Vol. 71. Siam, 2000 (cit. on p. 46).

[37] GC Hsiao and RE Kleinman. «Error analysis in numerical solution of acoustic integral equations». In: *International journal for numerical methods in engineering* 37.17 (1994), pp. 2921–2933 (cit. on pp. 49, 83).

[38] Adrien Merlini, Clément Henry, Davide Consoli, Lyes Rahmouni, Alexandre Dély, and Francesco P. Andriulli. *Laplacian Filtered Loop-Star Decompositions and Quasi-Helmholtz Laplacian Filters: Definitions, Analysis, and Efficient Algorithms*. 2022. arXiv: `2211.07704 [math.NA]` (cit. on pp. 50, 53–55, 87).

[39] Paolo Luchini and Alessandro Bottaro. «An introduction to adjoint problems». In: *arXiv preprint arXiv:2404.17304* (2024) (cit. on p. 52).

[40] Simon B Adrian, Francesco P Andriulli, and Thomas F Eibert. «Primal and dual wavelets for fast electric field integral equation solutions on unstructured meshes». In: *2017 IEEE International Symposium on Antennas and Propagation & USNC/URSI National Radio Science Meeting*. IEEE. 2017, pp. 723–724 (cit. on p. 53).

[41] David K Hammond, Pierre Vandergheynst, and Rémi Gribonval. «Wavelets on graphs via spectral graph theory». In: *Applied and Computational Harmonic Analysis* 30.2 (2011), pp. 129–150 (cit. on pp. 53, 54).

[42] G Golub and I Van. «CVL Matrix computations». In: *JHU Press* 3 (2012) (cit. on p. 54).

[43] Olin G Johnson, Charles A Micchelli, and George Paul. «Polynomial preconditioners for conjugate gradient calculations». In: *SIAM Journal on Numerical Analysis* 20.2 (1983), pp. 362–376 (cit. on p. 54).

[44] Steven F Ashby, Thomas A Manteuffel, and James S Otto. «A comparison of adaptive Chebyshev and least squares polynomial preconditioning for Hermitian positive definite linear systems». In: *SIAM Journal on Scientific and Statistical Computing* 13.1 (1992), pp. 1–29 (cit. on p. 54).

[45] E Oran Brigham. *The fast Fourier transform and its applications*. Prentice-Hall, Inc., 1988 (cit. on p. 60).

[46] James W Cooley and John W Tukey. «An algorithm for the machine calculation of complex Fourier series». In: *Mathematics of computation* 19.90 (1965), pp. 297–301 (cit. on p. 61).

[47] Matteo Frigo and Steven G Johnson. «FFTW: An adaptive software architecture for the FFT». In: *Proceedings of the 1998 IEEE International Conference on Acoustics, Speech and Signal Processing, ICASSP'98 (Cat. No. 98CH36181)*. Vol. 3. IEEE. 1998, pp. 1381–1384 (cit. on p. 61).

[48] Pierre Duhamel and Martin Vetterli. «Fast Fourier transforms: a tutorial review and a state of the art». In: *Signal processing* 19.4 (1990), pp. 259–299 (cit. on p. 61).

[49] Volker Schönefeld. «Spherical harmonics». In: *Computer Graphics and Multimedia Group, Technical Note. RWTH Aachen University, Germany* 18 (2005) (cit. on p. 63).

[50] Nabila Aghanim et al. «Planck 2018 results-I. Overview and the cosmological legacy of Planck». In: *Astronomy & Astrophysics* 641 (2020), A1 (cit. on p. 63).

[51] Willi Freeden and Michael Schreiner. *Spherical functions of mathematical geosciences: a scalar, vectorial, and tensorial setup*. Springer Nature, 2022 (cit. on pp. 63, 65).

[52] Shravan K Veerapaneni, Abtin Rahimian, George Biros, and Denis Zorin. «A fast algorithm for simulating vesicle flows in three dimensions». In: *Journal of Computational Physics* 230.14 (2011), pp. 5610–5634 (cit. on p. 63).

[53] Paul N Swarztrauber. «Spectral transform methods for solving the shallow-water equations on the sphere». In: *Monthly Weather Review* 124.4 (1996), p. 730 (cit. on p. 63).

[54] Stefan Kunis and Daniel Potts. «Fast spherical Fourier algorithms». In: *Journal of Computational and Applied Mathematics* 161.1 (2003), pp. 75–98 (cit. on p. 63).

[55] Reiji Suda and Masayasu Takami. «A fast spherical harmonics transform algorithm». In: *Mathematics of computation* 71.238 (2002), pp. 703–715 (cit. on p. 63).

[56] Vladimir Rokhlin and Mark Tygert. «Fast algorithms for spherical harmonic expansions». In: *SIAM Journal on Scientific Computing* 27.6 (2006), pp. 1903–1928 (cit. on p. 63).

[57] Emil Praun and Hugues Hoppe. «Spherical parametrization and remeshing». In: *ACM transactions on graphics (TOG)* 22.3 (2003), pp. 340–349 (cit. on pp. 64, 73).

[58] Jukka Sarvas. «Performing interpolation and anterpolation entirely by fast Fourier transform in the 3-D multilevel fast multipole algorithm». In: *SIAM Journal on Numerical Analysis* 41.6 (2003), pp. 2180–2196 (cit. on pp. 65, 87).

[59] EL Hill. «The theory of vector spherical harmonics». In: *American Journal of Physics* 22.4 (1954), pp. 211–214 (cit. on p. 65).

[60] Rubén G Barrera, GA Estevez, and J Giraldo. «Vector spherical harmonics and their application to magnetostatics». In: *European Journal of Physics* 6.4 (1985), p. 287 (cit. on p. 65).

[61] Jens Keiner, Stefan Kunis, and Daniel Potts. «Using NFFT 3—a software library for various nonequispaced fast Fourier transforms». In: *ACM Transactions on Mathematical Software (TOMS)* 36.4 (2009), pp. 1–30 (cit. on p. 68).

[62] Quoc T. Le Gia, Ming Li, and Yu Guang Wang. «Algorithm 1018: FaVeST—Fast Vector Spherical Harmonic Transforms». In: *ACM Trans. Math. Softw.* 47.4 (Sept. 2021). ISSN: 0098-3500. DOI: 10.1145/3458470. URL: https://doi.org/10.1145/3458470 (cit. on p. 70).

[63] Zeev Nehari. *Conformal mapping*. Courier Corporation, 2012 (cit. on p. 73).

[64] Bengt Fornberg. «A numerical method for conformal mappings». In: *SIAM Journal on Scientific and Statistical Computing* 1.3 (1980), pp. 386–400 (cit. on p. 73).

[65] Alla Sheffer, Craig Gotsman, and Nira Dyn. «Robust spherical parameterization of triangular meshes». In: *Computing* 72 (2004), pp. 185–193 (cit. on p. 73).

[66] Patrick Knupp and Stanly Steinberg. *Fundamentals of grid generation*. CRC press, 2020 (cit. on p. 74).

[67] Andrea Toselli and Olof Widlund. *Domain decomposition methods-algorithms and theory*. Vol. 34. Springer Science & Business Media, 2004 (cit. on p. 74).

[68] Barry F Smith. «Domain decomposition methods for partial differential equations». In: *Parallel Numerical Algorithms*. Springer, 1997, pp. 225–243 (cit. on p. 74).

[69] George C Hsiao, Olaf Steinbach, and Wolfgang L Wendland. «Domain decomposition methods via boundary integral equations». In: *Journal of Computational and Applied Mathematics* 125.1-2 (2000), pp. 521–537 (cit. on p. 74).

[70] Steven A Cummer, Nathan Kundtz, and Bogdan-Ioan Popa. «Electromagnetic surface and line sources under coordinate transformations». In: *Physical Review A* 80.3 (2009), p. 033820 (cit. on p. 74).

[71] Jeff Shragge and Guojian Shan. «Prestack wave-equation depth migration in elliptical coordinates». In: *Geophysics* 73.5 (2008), S169–S175 (cit. on p. 74).

[72] Matteo E Masciocchi, Ermanno Citraro, Alexandre Dély, Lyes Rahmouni, Adrien Merlini, and Francesco P Andriulli. «On some Operator Filtering Strategies Based on Suitably Modified Green's Functions». In: *2023 International Conference on Electromagnetics in Advanced Applications (ICEAA)*. IEEE. 2023, pp. 624–626 (cit. on pp. 75, 87).

[73] V Zakian and RK Littlewood. «Numerical inversion of Laplace transforms by weighted least-squares approximation». In: *The Computer Journal* 16.1 (1973), pp. 66–68 (cit. on p. 81).